

Reliability assessment of quay wall renewal method Koningsgracht

Jonas Yassien



Reliability assessment of quay wall renewal method Koningsgracht

A master thesis conducted at Royal HaskoningDHV

by

Jonas Yassien

to obtain the degree of Master of Science in Applied Earth Sciences, track
Geo-Engineering at the Delft University of Technology

Defended publicly on Friday November 17, 2023

Members of thesis committee:

Dr. ir. Mandy Korff (chair)	<i>Dep. of geotechnical eng.</i>
Dr. ir. Timo Schweckendiek	<i>Dep. of hydraulic eng.</i>
Dr. ir. Job Kool	<i>Royal HaskoningDHV</i>

Cover image by Royal HaskoningDHV

1 Preface

This thesis is written to conclude the master track Geo-Engineering for the study Applied Earth Sciences at Delft University of Technology. It has been conducted at engineering firm Royal HaskoningDHV.

Before the start of my thesis, I grappled with the decision to pursue my thesis within a corporate environment. In hindsight, I am very glad that I did. It taught me much about how structural or geo-technical designs were made and how potential problems were tackled from a more commercial perspective. The expertise on the work floor, from all kinds of directions, proved to be interesting and helpful. Working in a corporate setting provided me with a firsthand understanding of the dynamic interplay between theoretical knowledge and real-world applications.

The innovative thesis topic granted me further knowledge on quay wall structures and stability assessment problems. The use of probabilistic methods was completely new to me, so that in particular is knowledge I find very valuable to have gained.

I extend my gratitude to Royal Haskoning for offering me the opportunity to undertake my thesis in collaboration with them, and I am thankful for their willingness to share their knowledge and support. This opportunity has not only expanded my academic horizons but has also given me a practical insight into the industry.

In particular I would like thank my company daily supervisor Job Kool for his guidance throughout the project, and my TU supervisors Mandy Korff and Timo Schweckendiek for their investment and help in the project. Finally, I would like to thank my parents and family for their continuous support throughout my study period.

2 Abstract

This study focuses on the assessment of the reliability of the geobag wall system within the context of the Koningsgracht renewal project. The objective is to identify and understand the most sensitive phase during the project's execution by conducting a comprehensive probabilistic analysis.

The geobag wall, a temporarily constructed component of Koningsgracht, emerges as the focal point of sensitivity in this study. Unlike other project elements, such as historic structures and conventional engineering components, the geobag wall possesses unique characteristics, notably its composition of individual geobags and the use of jute geotextile, which could result into individual instability.

The research delves into the analysis of failure mechanisms and limit states for the geobag wall, considering both the monolithic structure and potential local failures within its segments. The failure modes found include horizontal sliding, overturning and the rupture of the geotextile. Various parameters are examined to calculate factors of safety.

To account for uncertainties inherent in geological and structural parameters, probabilistic methods are employed. Monte Carlo simulation and the First-Order-Second-Moment (FOSM) method are utilized to model the behavior of the geobag wall under different scenarios, encompassing a wide range of parameter combinations.

Correlations between parameters are introduced to simulate spatial variability, ensuring that the values of geological and structural factors align reasonably with one another. This approach reflects the real-world complexities of geotechnical systems.

The analysis reveals intriguing results, with factors such as friction angle playing a significant role in horizontal sliding and overturning, while textile rupture remains relatively independent of geological parameters and heavily reliant on tensile strength of the jute geotextile. Additionally, wall dimensions, particularly height and width, are found to exert a substantial influence on various failure modes.

Ultimately, the probabilistic analysis yields insights into the reliability of the geobag wall system. The study indicates a $1.625 \cdot 10^{-4}$ probability of failure for the geobag wall system considering a Factor of Safety (FOS) of 1.0, aligning with the overall reliability of the Koningsgracht renewal method.

Contents

1	Preface	1
2	Abstract	2
3	Introduction	9
3.1	Problem definition	10
3.2	Research objective and questions	11
3.3	Research method	13
3.3.1	Scope and limitations	13
3.3.2	Research flow diagram	14
4	Structural mechanics of Koningsgracht	15
4.1	Historic quay wall construction	16
4.1.1	Representative historic quay wall dimensions	17
4.2	Koningsgracht summary	20
4.3	Support reactions during Koningsgracht	26
4.3.1	Koningsgracht phases to be analyzed	26
4.3.2	Support reactions per construction phase	27
4.3.3	Moments in historic floor	30
4.3.4	Moments in historic piles using Blum	32
4.3.5	Assessment of pile strength	34
4.4	Common failure mechanisms for quay walls	35
4.5	Most sensitive phase	37
5	Failure mechanisms and limit states	38
5.1	Geobag wall dimensions and conditions	38
5.1.1	Normal force of the geobag wall	39
5.1.2	Earth pressure	39
5.2	Failure by horizontal sliding of geobag wall	41
5.2.1	Global horizontal sliding	41
5.2.2	Local horizontal sliding	42
5.3	Failure by overturning of geobag wall	44
5.3.1	Global overturning	44
5.3.2	Local overturning of wall	46
5.4	Failure by textile rupture of geobags	47
5.5	Additional factors of influence	49
5.5.1	Cohesion affecting horizontal sliding	49
5.5.2	Eccentricity	49
5.5.3	Stiffness	50
5.6	Movement behavior of segments	52
5.6.1	Tilting of the wall	52
5.6.2	Bulging of the wall	53

5.7	Geobag fault tree and failure mode parameters	54
5.8	Modelling methods	56
5.8.1	Deterministic analysis	56
5.8.2	Probabilistic analysis	56
5.8.3	Finite Element Method	56
6	Probabilistic analysis	58
6.1	Reliability methods	59
6.1.1	Comparing Monte Carlo to FOSM	60
6.2	PDF and CDF	61
6.3	Mean and standard deviation	64
6.3.1	Reliability index	66
6.4	Correlations	68
6.5	System reliability	70
6.5.1	System reliability of geobag wall	71
7	Geobag experiments	72
7.1	Potential experiments to determine coefficient of friction	72
7.2	Friction experiment	74
7.2.1	Friction test set-up	75
7.2.2	Friction test validation	75
7.2.3	Results friction experiment	77
7.2.4	Discussion friction experiment	79
8	Methodology	80
8.1	Probabilistic Toolkit	80
8.2	Parameters	82
8.2.1	Parameter correlations	85
8.3	Analyses to be performed	87
8.4	Scenarios for the sensitivity analysis	89
9	Results and interpretation	90
9.1	Global and local reliability analysis	91
9.1.1	Global reliability	91
9.1.2	Local reliability	92
9.2	Contribution analysis	95
9.3	Sensitivity analysis	98
9.3.1	Toolbox sensitivity analysis	98
9.3.2	Manual sensitivity analysis	100
9.4	Sensitivity to scenarios	104
9.5	Results system reliability	106
9.6	Additional discussion of parameter effects	109
9.6.1	Cohesion and friction angle	109
9.6.2	Friction angle wall-backfill	109

10 Conclusion	111
11 Recommendations	113
12 Appendix A - NEN 9997 - Table 2b	i

List of Figures

3.1	Collapse of Grimburgwal in 2020. [25]	9
3.2	The work in Koningsgracht is done from pontoons. [4]	10
3.3	Research flow diagram.	14
4.1	Historic quay wall construction composition. [36]	16
4.2	The exposed timber cross beams of the Maaskade in Rotterdam. [22]	17
4.3	A part of the Brouwersgracht quay wall, showing its height inconsistency, retrieved from RHDHV documents. [34]	18
4.4	Existing quay wall types in Amsterdam, with varying wall heights and floor widths, retrieved from RHDHV documents. [37]	18
4.5	Quay wall types according to blue-prints show the number of piles from type 1 to type 8, retrieved from RHDHV documents. [37]	19
4.6	The trench box is placed until the wooden floor. [36]	21
4.7	The casings are placed in pre-made holes in the floor. [36]	21
4.8	The underwater concrete is deposited next to the prefab concrete element. [36]	22
4.9	The sand bags are placed onto the new flooring, with a protecting plate in front. [36]	23
4.10	When the trench box is removed, the sand bags act as a retaining wall. [36]	23
4.11	The front piles are inserted. [36]	24
4.12	The prefab wall element can then be placed over the piles. [36]	24
4.13	When the flooring is finished, sand is deposited and the casings are partially pulled out. [36]	25
4.14	Most crucial phases of Koningsgracht to be analyzed.	26
4.15	Original quay wall with support reactions.	28
4.16	Pile support reactions of the original quay wall.	29
4.17	Pile support reactions after placing trench box, the new floor and the geobags.	29
4.18	Pile support reactions after removing the old quay wall.	30
4.19	Moments in floor of the original quay wall.	31
4.20	Moments in floor after placing the new floor and the sand bags.	31
4.21	Moments in floor after removing the old quay wall.	31
4.22	Blum describes how moments can be calculated in piles. [43]	32
4.23	The common failure modes of a historic quay wall. [39]	35
5.1	Visualization of geobag wall, with its seven segments, and the forces exerted on it.	38
5.2	Global horizontal sliding of wall, along the bottom interface.	42
5.3	Local horizontal sliding of wall, along one of the interfaces.	43
5.4	Global overturning of wall, with its moment forces and arms.	45
5.5	Local overturning of wall element, with its moment forces and arms.	46
5.6	Tension in geobag due to vertical and horizontal stresses. [30]	47
5.7	Example of a material with a low stiffness, deformed by the contours of the floor. [41]	50
5.8	Tilting of an elemental wall as a result of horizontal pressure. [13]	52
5.9	Bulging of an elemental wall as a result of horizontal pressure. [13]	53
5.10	Fault tree of the geobag wall.	54
6.1	When the limit state equals 0, it describes the boundary at which the the loads exceeds the resistance of a structure. [24]	58
6.2	The probability where low resistances and a high loads occur should be minimized. [24]	61
6.3	An example of a PDF, where the probability density (y-axis) is presented for every possible variable value (x-axis). The total area of the curve is equal to 1. [24]	62

6.4	An example of a CDF, with the values of a variable on the x-axis and the cumulative probability on the y-axis. [24]	62
6.5	The probabilities of the R and S variables form the equal probability circles on the R-S curve. [24]	63
6.6	The percentage of values that occur within a standard deviation away from the mean. [5]	64
6.7	The reliability index can be used as a substitute to the probability of failure for lower probabilities. [3]	66
6.8	Visualization of reliability index. [8]	67
6.9	Many realizations of two parameters with $\rho = -1$.	68
6.10	Many realizations of two parameters with $\rho = 0$.	68
6.11	Many realizations of two parameters with $\rho = 1$.	69
6.12	Many realizations of two parameters with $\rho = 0.5$.	69
6.13	A visualization of series and parallel systems. [24]	70
6.14	An example of systems with mutually exclusive, independent or dependent events. [24]	71
7.1	Visualization of direct shear test and pullout test. [40]	72
7.2	Principle of friction. [35]	74
7.3	A smooth wood plank and three concrete bricks.	75
7.4	The smooth surface of the concrete bricks.	76
7.5	Jute was attached to the inclined wood plank. The tilt, measured by the phone, was increased until motion of the brick.	76
7.6	By wrapping a concrete brick with jute, a jute-jute interface is created.	77
8.1	The model is made using an internal Python script, where the probabilistic input and output variables can be defined separately, as shown by the red markings.	80
8.2	The type of distribution needs to be defined for all probabilistic variables.	81
8.3	An example of the correlation input screen of the Probabilistic Toolbox.	81
8.4	The requested output variables are displayed as distributions.	81
8.5	An example of the correlation distribution with respect to the bottom segment for both the geological and structural parameters.	86
8.6	An example of the correlation between the friction angles on the first and second interface.	86
9.1	The PDF's of the FOS distribution for all failure mechanisms.	91
9.2	The CDF's of the FOS distribution for all failure mechanisms.	92
9.3	Parameter contributions of all failure modes.	96
9.4	The FOS sensitivity to all parameters for all modes.	99
9.5	PDF curves of the FOS of horizontal sliding for a changing friction angle and changing jute-concrete friction coefficient.	101
9.6	The effect of friction angle ϕ on the active earth pressure K_a for different values of wall-backfill friction angle δ . [23]	110

List of Tables

4.1	Dimensions of quay wall type 6.	19
5.1	All failure mode parameters. The color codes state the origin of the parameter values that are used in this thesis.	55
7.1	Weights used during the experiment.	77
7.2	Angle of mobilizations (α) per weight, with their mean and the corresponding coefficient of friction (μ).	78
7.3	Angle (α) of mobilization for the jute-jute validation.	78
8.1	Deterministic values for all parameters used in the stability analysis.	82
8.2	Standard deviation of soil parameters using their coefficient of variation. [2] . . .	83
8.3	Probabilistic parameters used for stability analysis.	84
9.1	Results probabilistic analysis of geobag wall failure mechanisms.	91
9.2	All FOS distributions and failure probabilities per mode for every local interface along the geobag wall.	93
9.3	Results of the reliability analysis, stating the impact of all parameters per failure mode.	95
9.4	Lower, mean and upper boundary values for all uncertain parameters, used for the sensitivity analysis.	100
9.5	Reliability of the global geobag wall against horizontal sliding per changing parameter.	102
9.6	Reliability of the global geobag wall against overturning per changing parameter.	102
9.7	Reliability of the global geobag wall against textile rupture per changing parameter.	102
9.8	Parameter values for the original situation, and for the additional 8 scenario's.	104
9.9	Global reliability against horizontal sliding for the original situation and for the additional 8 scenarios.	104
9.10	Global reliability against overturning for the original situation and for the additional 8 scenarios.	104
9.11	Global reliability against textile rupture for the original situation and for the additional 8 scenarios.	105
9.12	All FOS distributions and failure probabilities per mode for every local interface along the geobag wall.	106
9.13	System probability of failure considering modes and interfaces being dependent and independent from one another.	107

3 Introduction

At the end of the 16th century, the city of Amsterdam started founding its quay walls on timber piles. [22] These old quay walls are reaching the end of their service life, for the condition of its foundation has deteriorated over the centuries. More than 200 km of quay walls is to be replaced by the municipality, and more than half of these quay walls have a high risk of collapse. [22] A recent example is the collapse of Grimburgwal in 2020. [25] Ever since, the municipality of Amsterdam has given a higher priority to researching and renovating the remaining quay walls, questioning their stability. In figure 3.1 the collapsed Grimburgwal is shown.



Figure 3.1: Collapse of Grimburgwal in 2020. [25]

In this introductory chapter, the problem definition of this thesis will be presented, together with its research objectives and research questions. This is followed by the research scope and the research flow diagram of this thesis.

3.1 Problem definition

To ensure the safety and stability of the historic quay walls faster, the municipality of Amsterdam stated that innovation was required. For this reason, the city started the innovation partnership regarding quay wall renovations in Amsterdam (project IPK, innovatieproject kademuren). The municipality has started this project with several companies in order to come up with new quay wall renewal methods, focused on efficiency and speed of the renovation, accessibility of the quays during the renewal process, and the durability of the work. [1]

Royal HaskoningDHV (RHDHV) has been given the opportunity to contribute to IPK with the method Koningsgracht, which has been created in a collaboration with the company BAM.

Koningsgracht focuses on the renovation of small segments of quay walls, in which the renewal process moves along the quay wall in a train like manner. During this method, the quay wall remains accessible to the public, because all the work is done via pontoons situated in the canals. The method is said to be durable, for all equipment used is electric, and existing trees along the quay are preserved. [1] In figure 3.2 the work from the pontoon is visualized.



Figure 3.2: The work in Koningsgracht is done from pontoons. [4]

In order for this new method to be used on a large scale in the future, its reliability needs to be analyzed in terms of quay wall stability during the renewal. This is important for safety and economical purposes. It is a method that is still under development such, that the construction stages are still being altered, and the structural mechanics are not yet visualized for all stages. A pilot project, where Koningsgracht is being applied for the first time, is being performed at a part of Brouwersgracht in Amsterdam while this thesis is being conducted. Therefore, the quay walls of Brouwersgracht will act as a representative construction for this research.

3.2 Research objective and questions

The objective for this thesis is to determine the reliability of Koningsgracht by retrieving the probability of failure for the most vulnerable or uncertain work phase within the renewal method. This shall be done by describing this phase in a model, and to use this model to assess the phase's stability. Additionally, a sensitivity analysis is performed in order to see what variables inside the created model play a dominant factor to determine the phase's stability.

The thesis objective above results into the following research question:

Main research question: *"What is the reliability of Koningsgracht?"*

To reach the answer of the main research question, multiple sub-questions are necessary:

1. **First sub-question:** *"What is the most sensitive phase in the Koningsgracht method?"*
2. **Second sub-question:** *"How do the support reactions change during Koningsgracht, and how is equilibrium maintained?"*
3. **Third sub-question:** *"How to assess the Koningsgracht stability?"*
4. **Fourth sub-question:** *"What are the most sensitive variables in the most sensitive phase?"*
5. **Fifth sub-question:** *"What is the reliability of the most sensitive phase of Koningsgracht?"*

The initial sub-question is addressed through an examination of the Koningracht construction phases. A comprehensive literature review is conducted to assess the stability of the quay wall during each phase. This process helps identify potential weaknesses or uncertainties within the project. For instance, the research may focus on determining whether specific combinations of elements are new or if there are any gaps in knowledge concerning material properties and soil characteristics.

The second sub-question focuses on examining the support reactions of elements involved in the different phases of the Koningsgracht project. To better understand the phases that have emerged as potentially critical in the literature review, we perform basic support reaction calculations. These calculations rely on material and soil properties, which we can obtain from both literature sources and the project's design documentation. This approach allows for the gaining of rapid insights into the structural behavior and stability of key elements within the project, and to uncover potential weak links during the renewal method.

When sufficient variables of the construction and the soil are known, a reliable model can be set-up, which relates to sub-question three. The crucial phase should be researched based on its failure mechanisms. These should be modeled such that a Factor of Safety (FOS) can be calculated for every failure mode. Using a probabilistic analysis, these models can be used to derive the probability of failure per failure mode.

Addressing the fourth and final sub-question involves a comprehensive evaluation of the system's stability, including all potential failure modes. These individual probabilities of failure must then be systematically combined to derive an overall probability of failure for the entire crucial phase of the Koningsgracht project. The reliability of this critical phase is considered to be connected to the overall reliability of the Koningsgracht project. Consequently, answering this sub-question not only addresses the specific inquiry but also provides a conclusive response to the main research question, shedding light on the overall reliability and safety of the method.

3.3 Research method

3.3.1 Scope and limitations

In order to maintain the focus of the thesis and ensure the quality of research, it is essential to establish a specific scope.

First of all, this thesis will concentrate exclusively on one phase or on one significant element of the Koningsgracht method, given that a single phase or element offers a substantial level of complexity.

Only one version of Koningsgracht is to be researched. Since Koningsgracht is still developing, the construction phases are not definite. However, the research done in this thesis should still be relevant for the final design of Koningsgracht.

Additionally, it should be noted that Koningsgracht includes alternative phases for renovating a quay segment that incorporates a tree. These alternative phases are beyond the scope of this research. Furthermore, this thesis will be constrained to examining a particular historical quay wall construction composition that represents quays walls in Amsterdam.

Finding a proper method to assess the stability of Koningsgracht should be a part of this thesis, but only one stability method should be chosen to work with.

A final important note is that the reliability of Koningsgracht is considered to be equal to the reliability of the most crucial phase, and therefore neglecting the probability of failure in phases that fall outside this thesis's scope.

3.3.2 Research flow diagram

In figure 3.3, the research flow diagram of this thesis is presented.

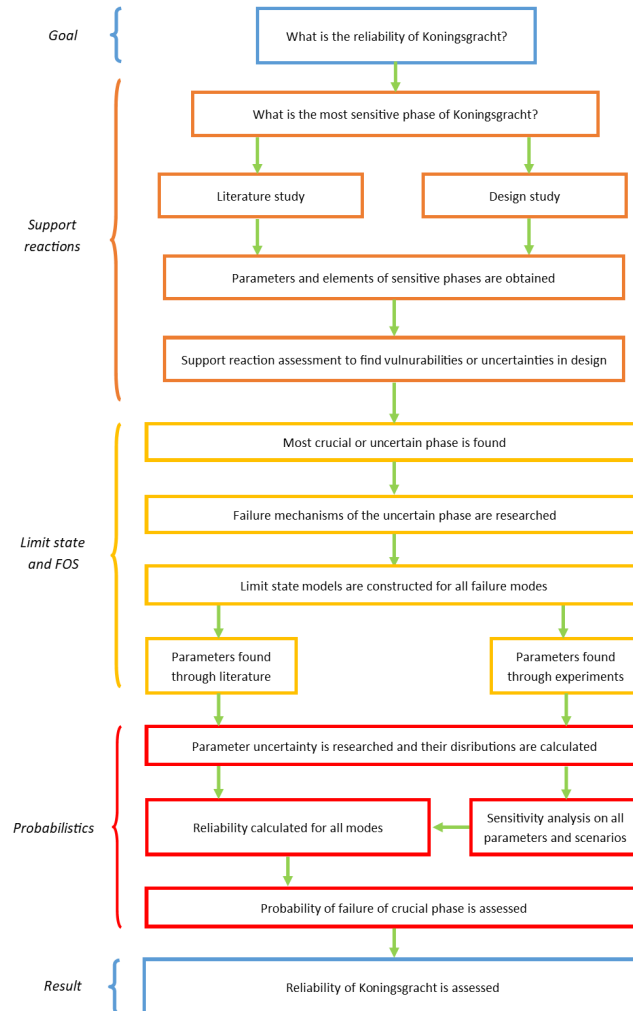


Figure 3.3: Research flow diagram.

4 Structural mechanics of Koningsgracht

To identify the most sensitive work phase during Koningsgracht, it is imperative to provide a brief overview of all phases. This chapter begins with an examination of the historical quay walls, utilizing a representative set of dimensions that encapsulate the entire construction process considered in this thesis. Subsequently, a concise overview is provided of the key work phases within Koningsgracht. These phases are subjected to a preliminary assessment based on simplistic support reactions applied throughout the construction process. This initial analysis aims to find the phase characterized by the highest degree of uncertainty or instability, which would then need a more comprehensive evaluation. It is crucial to note that, in the context of this thesis, the overall reliability of Koningsgracht hinges entirely upon the reliability of this identified critical phase.

4.1 Historic quay wall construction

Before the renewal method Koningsgracht can be described, the original quay wall construction has to be understood. For this thesis, a specific composition of its elements is considered to be the original historic quay wall construction. This composition should represent the majority of historic quay walls in Amsterdam. In figure 4.1, this construction is shown.

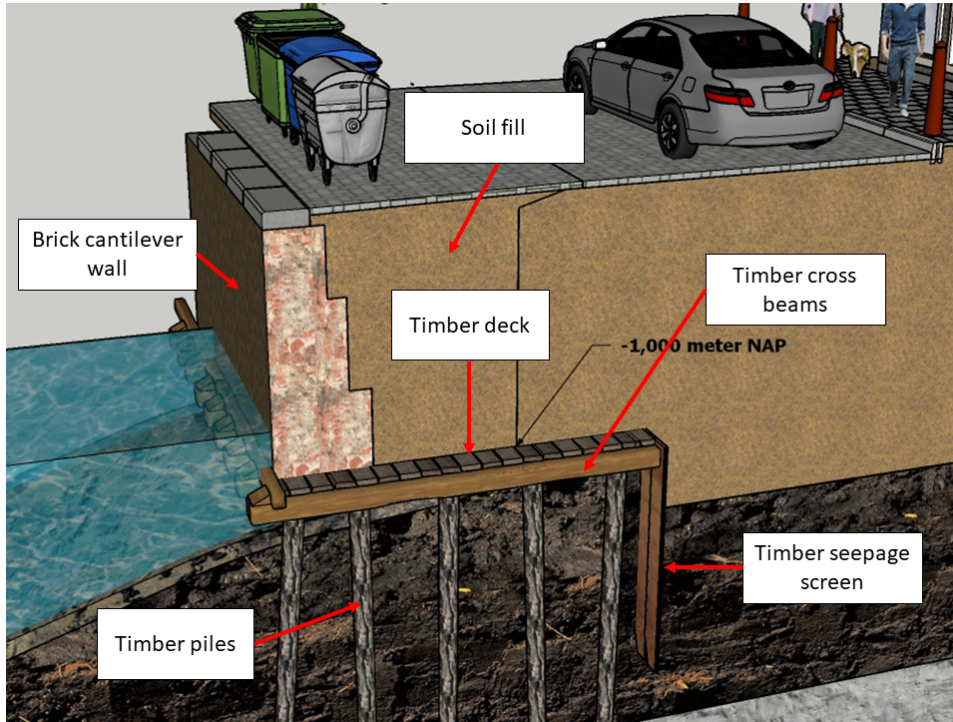


Figure 4.1: Historic quay wall construction composition. [36]

As depicted in Figure 4.1, the historic quay walls exhibit a distinctive structure comprising a timber deck supported by a framework of timber beams [22]. Each of these beams is affixed with a row of timber piles. Notably, the front pile, situated along the canal side of the deck, is inclined, enhancing its ability to provide lateral load resistance. On the opposite side of the timber deck, a timber seepage screen serves its function. Positioned atop the timber deck, facing the canal, stands a brick cantilever wall. Behind this robust gravity wall, backfill extends to street level, where the public road is constructed upon. [22] In 2019, the quay wall of the Maaskade in Rotterdam was excavated, showing the original timber cross beams with piles, on which the rest of the flooring was founded, as can be seen in figure 4.2.



Figure 4.2: The exposed timber cross beams of the Maaskade in Rotterdam. [22]

4.1.1 Representative historic quay wall dimensions

To perform an accurate analysis of Koningsgracht, a structural composition of a quay wall with their respective dimensions should be chosen which represents the quay walls in Amsterdam well. As the pilot of Koningsgracht is conducted on the Brouwersgracht in Amsterdam, the original quay wall constructions there function as the base for this analysis. In figure 4.3 a front view of a part of Brouwersgracht is shown, retrieved from RHDHV design documents. From this image it becomes apparent that the quay wall height is not consistent over one street, and therefore a representative height should be chosen.

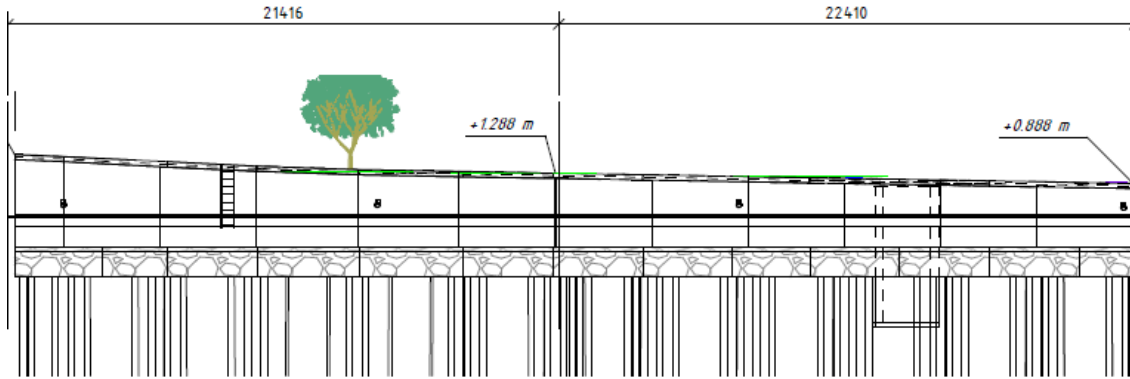


Figure 4.3: A part of the Brouwersgracht quay wall, showing its height inconsistency, retrieved from RHDHV documents. [34]

Higher quay walls need to retain larger bodies of soil, resulting into a larger magnitudes of forces compared to lower quay walls. As a basis for this Koningsgracht stability analysis, it is decided to use a quay wall type that with a relatively small retaining height. In figures 4.4 and 4.5, eight quay wall types are described that exist in Amsterdam, retrieved from RHDHV documents. Each type has a unique retaining height, floor width and number of piles.

Type	Retaining height [m]	Floor level [m NAP]	H top of quay [m NAP]	Width masonry [m]	Width floor [m]
8	1,5	1,2	0,3	0,55	1,9
7	1,7	1,2	0,6	0,55	2,4
6	2,1	1,2	0,9	0,66	2,6
5	2,4	1,2	1,2	0,77	3,1
4	2,7	1,2	1,5	0,88	3,4
3	3	1,2	1,8	0,99	3,9
2	3,3	1,2	2,1	1,1	4,15
1	3,6	1,2	2,4	1,21	4,4

Figure 4.4: Existing quay wall types in Amsterdam, with varying wall heights and floor widths, retrieved from RHDHV documents. [37]

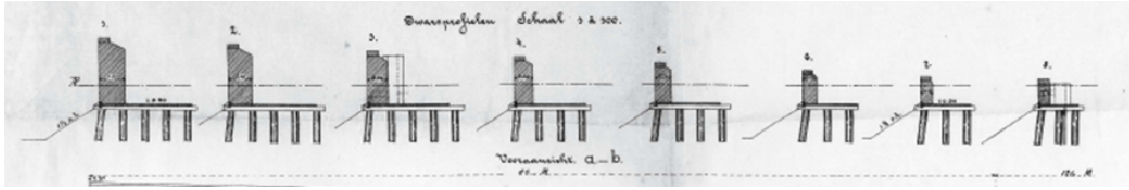


Figure 4.5: Quay wall types according to blue-prints show the number of piles from type 1 to type 8, retrieved from RHDHV documents. [37]

For this thesis it is decided to work with quay wall type 6 since it has one of the smaller retaining heights, and because it only consists of 3 piles per cross section. Because of this, the preliminary assessment remains sufficiently simplistic. Considering quay wall type 6, the quay wall construction composition results into the values listed in table 4.1.

Characteristic	Unit	Value
Retaining height	[m]	2.1
Height floor	[m NAP]	- 1.2
Height level of quay wall	[m NAP]	0.90
Width masonry wall	[m]	0.66
Width floor	[m]	2.6
Number of piles	-	3

Table 4.1: Dimensions of quay wall type 6.

Additionally, information about the quay wall foundation is required. According to Frankemolen (2006) [16], historic constructions in Amsterdam were mostly founded on the first sand layer. A general guideline was a pile length of approximately 12 meters, reaching the sand layer on approximately NAP - 12 m. The piles had a general diameter of 232 mm at the head, and 135 mm at the base of the piles. Each row of piles is attached to wooden beams, which are constructed perpendicular to the canal. The wooden beams are considered to have a distance of 1.25 meters to one another, according to the studies of RHDHV. The number of piles on each wooden beam depends on the type of quay wall, with 3 piles for the considered type 6. It should be noted that it is difficult to have perfectly representing dimensions for the piles in this analysis, for the real dimensions are not consistent along a quay wall and these are often unknown.

4.2 Koningsgracht summary

As outlined within the scope and limitations, this thesis will focus on researching a single variant of the Koningsgracht renewal method. This is due to the changes that are still made in the design and during the construction phases of the pilot. The subsequent subsections will provide detailed descriptions of the primary construction phases involved in Koningsgracht.

In this section, a description of the construction phases of Koningsgracht will be given. A summary of Koningsgracht is given by the phases shown below: [36]

1. Existing quay wall
2. Inserting trench box
3. Inserting casings
4. Constructing new floor
5. Placing geobags
6. Pulling trench box
7. Removing old quay wall
8. Inserting front piles and new wall

In a predetermined segment of the quay wall, a trench box is inserted down until the old wooden floor, as can be seen in figure 4.6. While lowering the trench box, it is simultaneously excavated. The trench box is placed to function as a retaining element during excavation, and to use it as a mold for the placement of concrete later in the process. [36]

When the trench box is excavated up until the wooden floor, holes are made in the floor. Through these holes, casings are placed in an inclined position, alternating the direction of inclination. The casings are then filled with sand. This phase is shown in figure 4.7. [36]

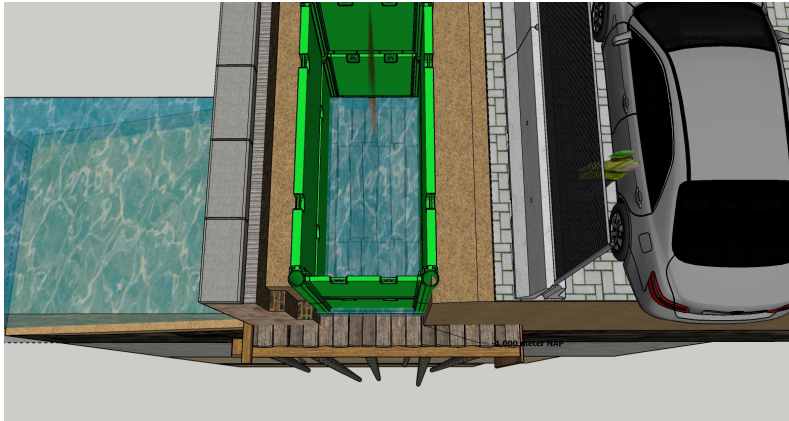


Figure 4.6: The trench box is placed until the wooden floor. [36]

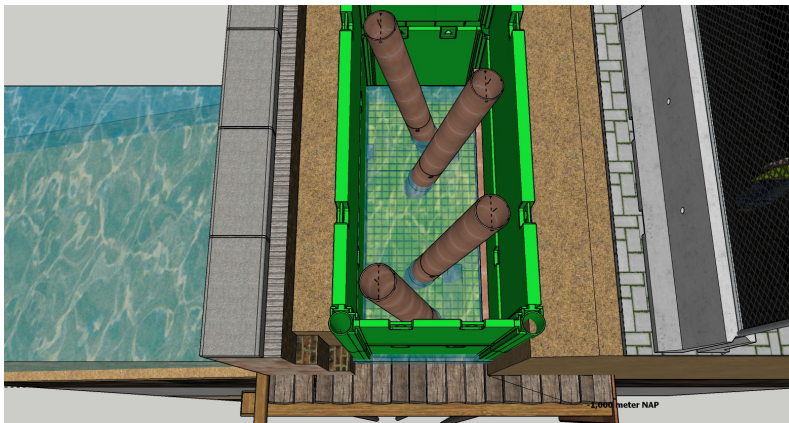


Figure 4.7: The casings are placed in pre-made holes in the floor. [36]

After placing the casings, the new flooring is to be constructed, as shown in figure 4.8. Note that this is partially done in water. On top of the wooden floor, a foil formwork and a prefab concrete element is placed. Underwater concrete is then deposited into the trench box, until the height of the prefab element, together resulting into a part of the new concrete flooring. [36]

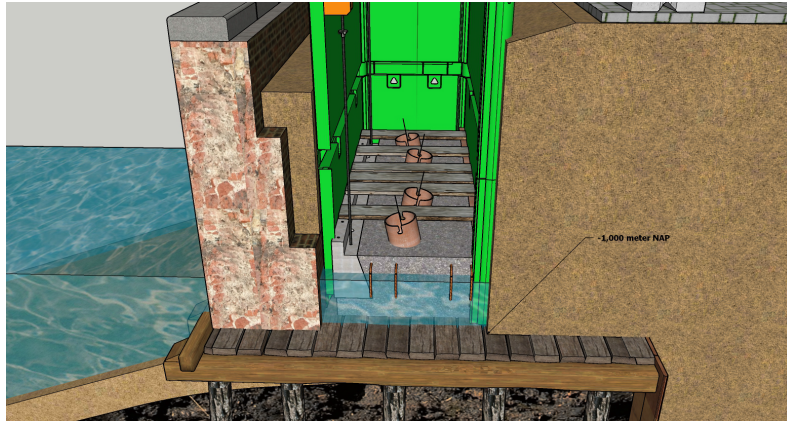


Figure 4.8: The underwater concrete is deposited next to the prefab concrete element. [36]

When the concrete has hardened, The trench box is filled with geobags, surrounding the existing casings, as shown in figure 4.9. The geobags should later function as a temporary retaining wall. For this thesis, it is considered that the geobags are situated above the phreatic surface. In front of the geobags, on the canal side, a metal plate is placed to protect the geobags against damages that might occur during the demolishing of the old quay wall. [36]

Now that there is a new retaining wall of sand bags, the space between the trench box and the old wall is excavated, and the trench box is removed. Then, the old quay wall is demolished, leaving the metal plate and the geobags, as can be seen in figure 4.10. [36]

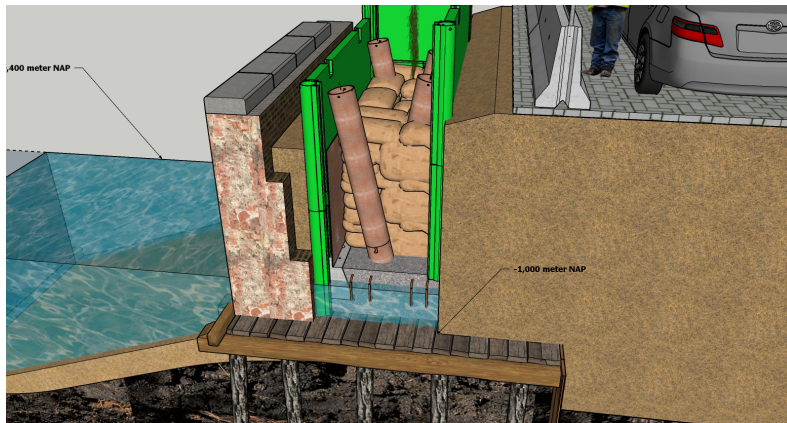


Figure 4.9: The sand bags are places onto the new flooring, with a protecting plate in front. [36]

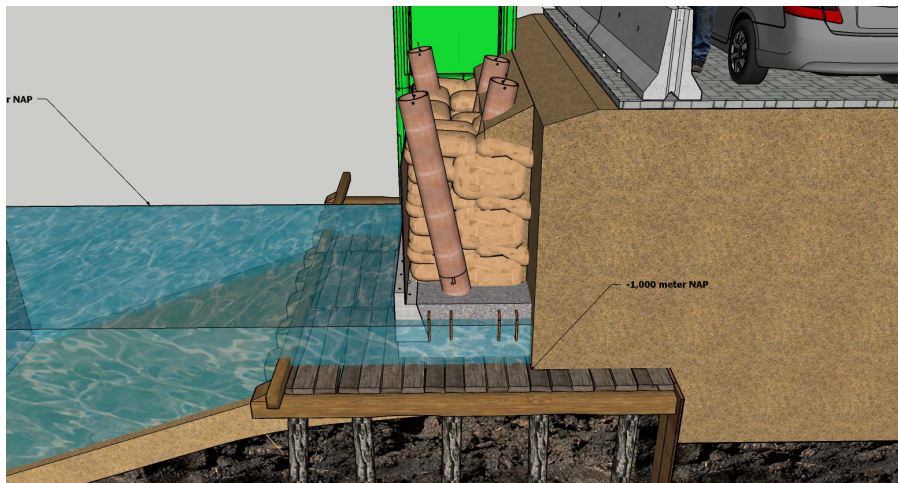


Figure 4.10: When the trench box is removed, the sand bags act as a retaining wall. [36]

To place the new quay wall, holes are drilled at the location of the old quay wall. From a pontoon, piles are inserted in these holes, shown in figure 4.11. A prefab wall element can then be placed over these piles, fixated by struts, shown in figure 4.12. [36]

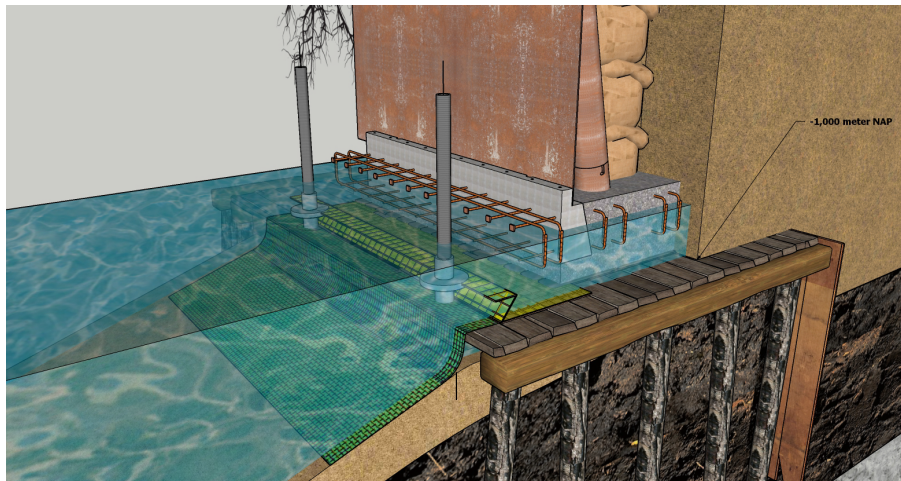


Figure 4.11: The front piles are inserted. [36]

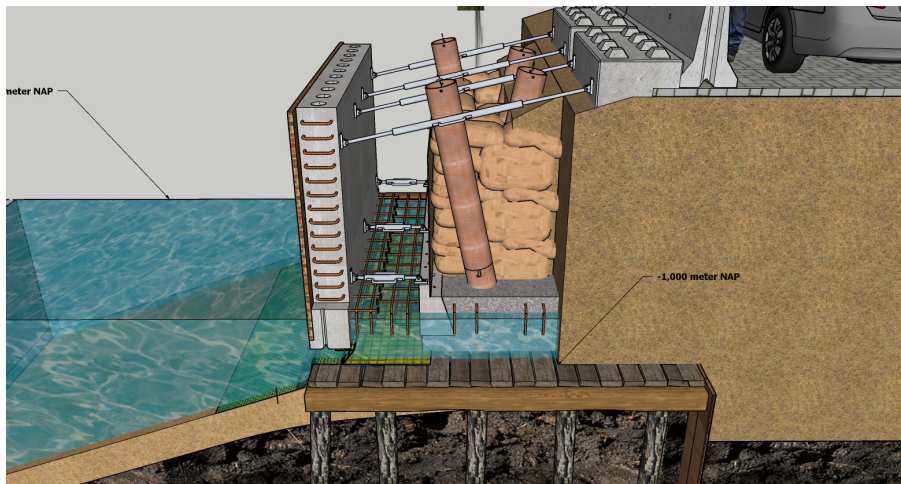


Figure 4.12: The prefab wall element can then be placed over the piles. [36]

In between the new wall element and the concrete flooring that was constructed before, a wet joint is to be made using foil formwork and by depositing underwater concrete. When the wet joint has hardened, the space between the sand bags and the new wall element is filled with sand. The inclined piles are inserted into the inclined casings. After recovering a part of the casings and the metal plate, the renewal method is finished, as presented in figure 4.13. [36]

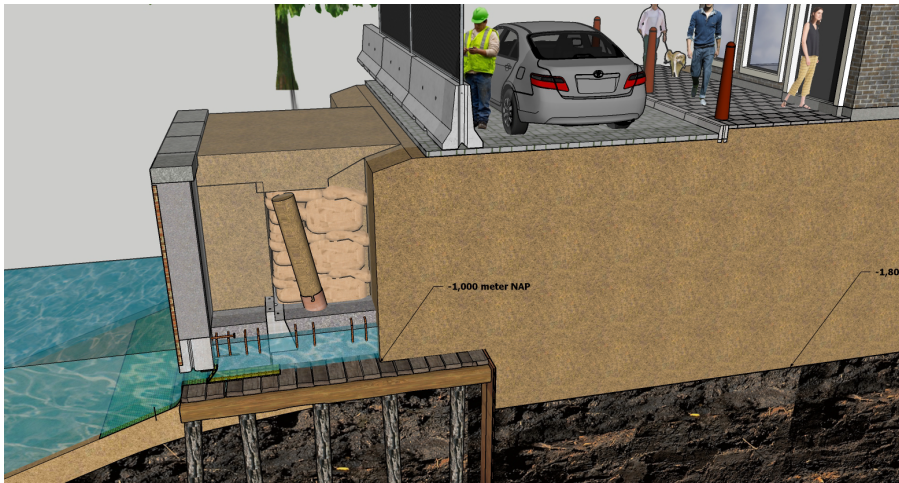


Figure 4.13: When the flooring is finished, sand is deposited and the casings are partially pulled out. [36]

4.3 Support reactions during Koningsgracht

To understand what the most sensitive phase in Koningsgracht is, an understanding of the internal support equilibrium is necessary, together with the changing support reactions during Koningsgracht. In order to analyze the stability of Koningsgracht, a representative quay wall type should be considered, together with the most important Koningsgracht phases. From this, the support reactions and the internal moments can be calculated to get an understanding of the structural responses during Koningsgracht. Finally, a strength assessment can be done of the quay wall components during the process.

4.3.1 Koningsgracht phases to be analyzed

It is decided that three Koningsgracht phases are to be analyzed for their stability, since these can cause a significant change in the structural balance between quay wall components. The phases listed below and shown in figure 4.14 are considered to be the most crucial.

1. Original historic quay wall
2. Placing trench box, constructing new floor and placing geobags
3. Removing old quay wall

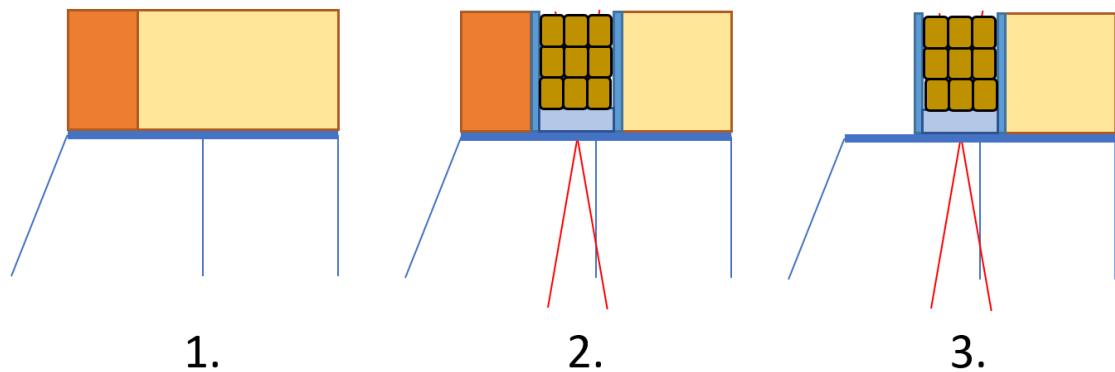


Figure 4.14: Most crucial phases of Koningsgracht to be analyzed.

To analyze these phases for their support reactions, moments and to assess the structure's strength, more dimensions are needed for the added elements. These dimensions all originate from RHDHV design documents.

First of all, the trench box is inserted next to the original masonry wall. According to the RHDHV design, the trench box can have a width of up to 1.6 m, although there are more widths possible. In this thesis, the trench box is considered to be placed exactly behind the masonry wall and that it has a width of 1.0 m. This is decided to make the geobag wall that is constructed in the trench box have more conservative dimensions.

Secondly, the casings are inserted down to a depth of NAP - 22,5 m, into the second sand layer. This layer starts at NAP -18 m. The diameter of these casings are considered to be 300 mm. The casings are inserted in an inclined 5:1 ratio, alternating their direction towards the canal and towards the road. The casings are considered to be perfectly placed in the middle of the trench box, as is done for the most segments in Koningsgracht according to RHDHV documents. For the quick assessment of the stability during Koningsgracht, the casings are considered not to interact with other elements, and are neglected for the stability assessment.

The new concrete floor that is constructed in the trench box has a height of 0.5 m on top of the original wooden floor, and is considered to have the exact same length and width as the trench box. On top of the new floor, the geobags are placed around the casings. For simplicity reasons for the support reactions, the column of bags are considered to be a column of sand, neglecting possible gaps between the bags.

4.3.2 Support reactions per construction phase

First, the support reactions of the original quay wall construction should be schematized in 2D. The schematic of this 2D scenario is shown in figure 4.15. The connection between the floor and piles are schematized by hinges, allowing for the transfer of support reactions, without exerting a normal force in any direction. The base of the piles are schematized such, that these can exert a normal force in the vertical direction, and only the inclined pile can additionally exert a normal force in the lateral direction. The wooden floor is considered to have no stiffness, meaning that all stresses will be transferred to the piles below the floor, without a new stress distribution.

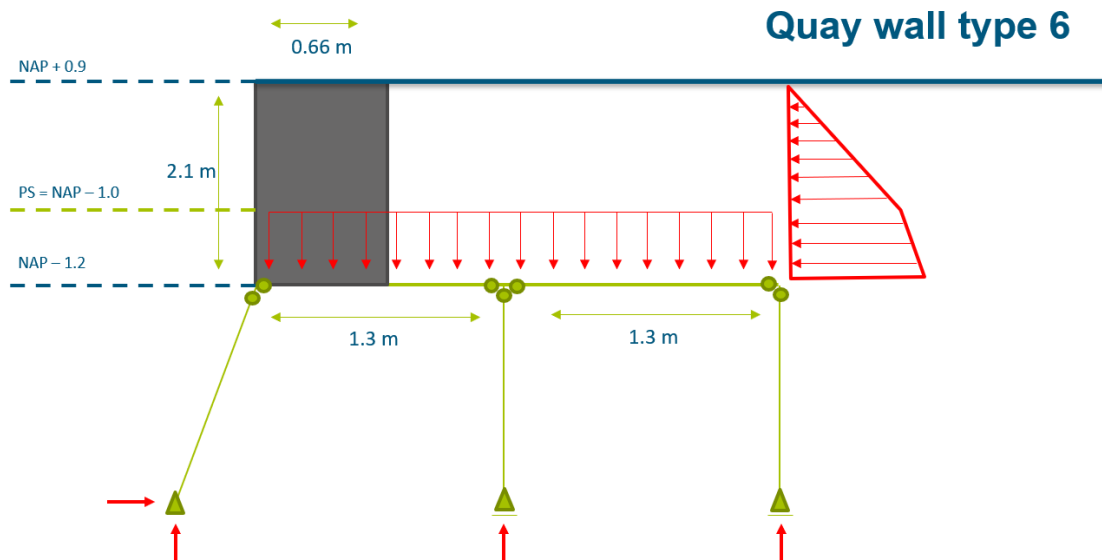


Figure 4.15: Original quay wall with support reactions.

As can be seen in figure 4.15, there are horizontal and vertical external stresses acting on the system. First of all, there is the lateral stress from the soil that pushes against the quay wall. This stress increases with depth. The quay wall remains on its place due to its attachment and friction to the wooden floor. The wooden floor remains on its place using a resisting force from the inclined front pile.

Secondly, there are also vertical stresses present. The wooden floor experiences the weight of the masonry wall at the front side, and the weight of the soil in the back of the floor. Additionally, there is a variable load considered of 5 kPa over the whole quay wall construction, which simulates the (construction) traffic loads. [18]

The wooden floor is piled, granting it a vertical resistance to the experienced loads. The inclined pile gives both a horizontal and vertical resistance. The support reactions from the pile are determined in a simplistic manner. As mentioned above, the floor is considered to have to have no stiffness, and therefore does not change the distribution of stresses before it reaches the piles. Each pile is considered to bear the loads that are present on half the distance to the next pile. That means that the load area of the middle pile is twice the size of the load areas of the side piles. The support reactions of the piles per phase are shown in figures 4.16 to 4.18.

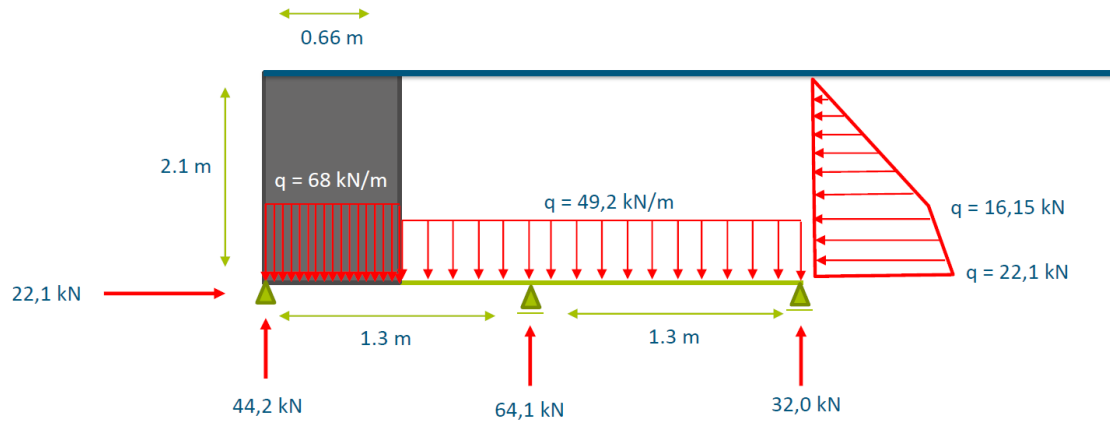


Figure 4.16: Pile support reactions of the original quay wall.

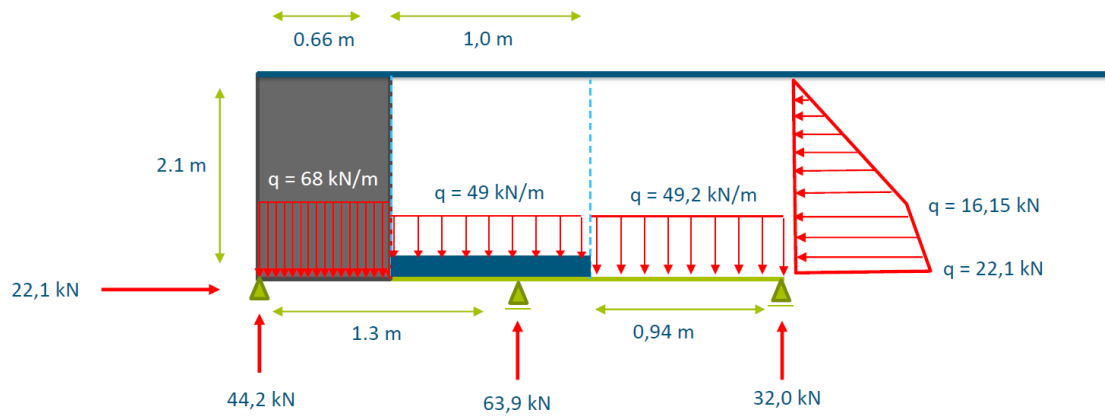


Figure 4.17: Pile support reactions after placing trench box, the new floor and the geobags.

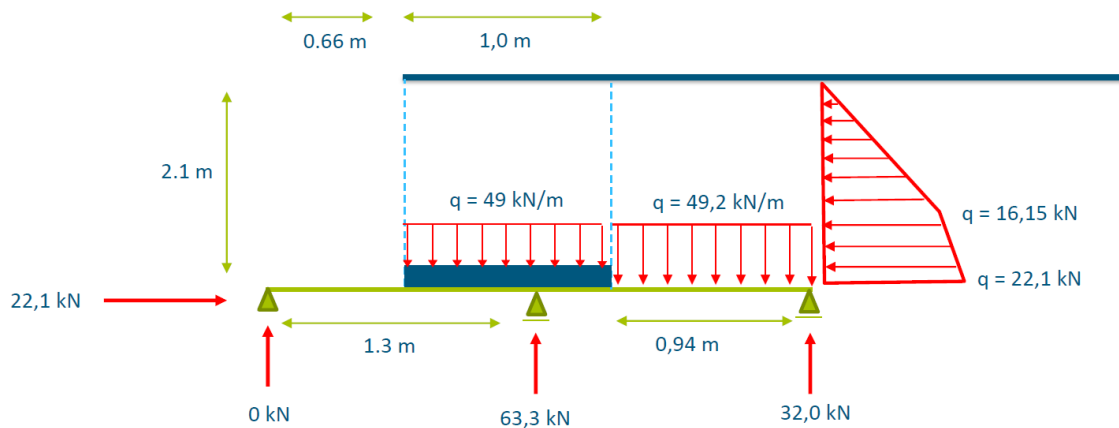


Figure 4.18: Pile support reactions after removing the old quay wall.

From figures 4.16 to 4.18 can be seen that the support reactions barely change from the original situation to the phase where the trench box is inserted, and the geobags are placed. When the old masonry wall is removed, so is all the load on the front pile. Note that this is the result from considering a stiffness floor. In reality, the front pile would share more loads with other piles with an increasing floor stiffness.

From these support reactions, no significant instabilities are noticed because the support reactions remain similar or lower than those from the original situation.

4.3.3 Moments in historic floor

When the loads and pile supports are known, it is possible to calculate the moments throughout the historic wooden floor. The moments give an indication of the bending forces that are applied to the floor, and could be used for a strength assessment. Based on the support reactions, the moments in figures 4.19 to 4.21 are obtained for the wooden floor for the crucial phases. The moment lines are indicated with a red line. The symbol inside the moment lines indicate the direction of bending.

From figures 4.19 to 4.21 can be seen that the bending moments in the historic quay wall only change from the removal of the old masonry wall, all due to the fact that the front pile did not experience any load because of the stiffness floor. In reality, the floor does have a stiffness, which redistributes loads more evenly, making moment changes smaller along the construction.

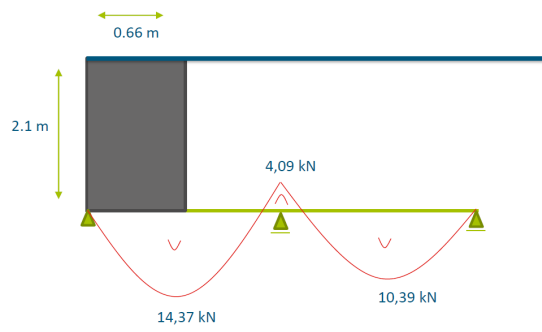


Figure 4.19: Moments in floor of the original quay wall.

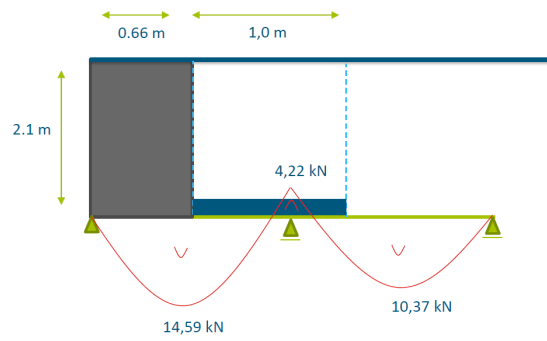


Figure 4.20: Moments in floor after placing the new floor and the sand bags.

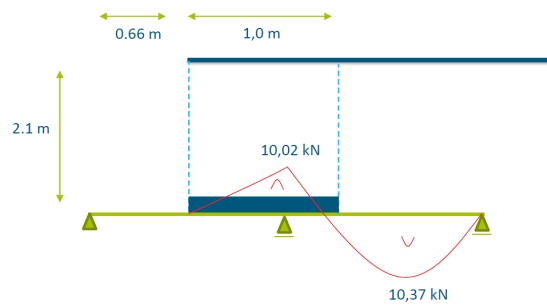


Figure 4.21: Moments in floor after removing the old quay wall.

4.3.4 Moments in historic piles using Blum

The moments of the historic piles underneath the floor could also be assessed. However, the method to be used for this is different than that for the floor moments. All piles underneath the floor are expected to experience a lateral force from the active soil pressure, and a resisting force from the passive soil pressure. This causes forces on this pile, inducing moments. Because the lateral stresses increase with depth, retrieving the moments can become difficult. For this reason, the Blum method is used for a simplified approach. [43]

Blum (1932) created a simplified method to obtain moments and deformations in retaining walls, but according to Van Baars et al. (2002) [43] this method can be used for piles as well for a rough indication. Blum considers a pile of length $h + t$, with length t being the part driven into the ground. As can be seen in the left image in figure 4.22, along the pile there is a point where the moment is zero. This theoretical penetration depth is called t_0 , where [38]:

$$t_0 = t/1,2 \quad (1)$$

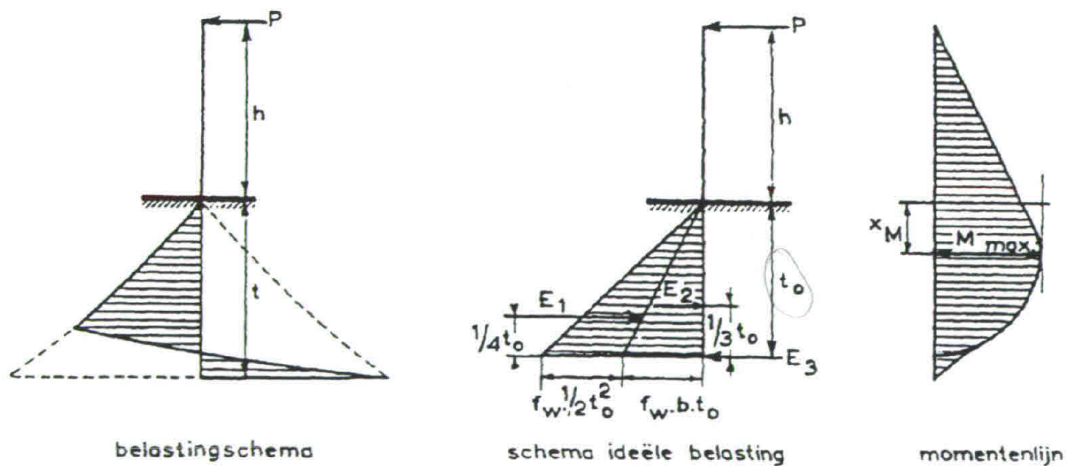


Figure 4.22: Blum describes how moments can be calculated in piles. [43]

Because moment equilibrium with theoretical penetration depth t_0 is zero, the maximum force the pile can support (P) can be calculated as [43]:

$$P = \gamma' K_p \frac{t_0^3}{24} \frac{t_0 + 4b}{t_0 + h} \quad (2)$$

Where γ' is the unit weight of the soil, K_p is the passive ground pressure coefficient, b the width of the pile, and h the height of the pile above the ground. K_p can be obtained by the following relationship [43]:

$$K_p = \frac{1 + \sin(\phi')}{1 - \sin(\phi')} \quad (3)$$

Where ϕ' is the friction angle of the soil. With P, all lateral forces on the Pile are known, thus it is possible to retrieve the moments. At a certain point on the pile x_M the moment is maximal. To find this point, the following relationship can be used [43]:

$$x_M^2(x_M + 3b) = \frac{t_0^3 t_0 + 4b}{4 t_0 + h} \quad (4)$$

Using an iterative process, the above equation leads to the location on the pile x_M where the maximum moment occurs. This moment can be calculated using the following calculation [43]:

$$M = P(h + t_0) - \gamma' K_p \left(\frac{bx^3}{6} + \frac{x^4}{24} \right) \quad (5)$$

4.3.5 Assessment of pile strength

With the method described in the previous section, the bearing capacity of the piles can be determined together with the maximum moments that occur along a pile. When this information is available, it is possible to assess if the loads do not exceed the strength of the pile.

Van de Kuilen et al. (2021) [45] discussed that the mean wet compression strength of new timber piles is approximately 16 N/mm^2 , resulting in a load carrying capacity of 150 to 320 kN, depending on the dimensions of the pile. It is stated that timber piles that are in use for several decades, the long-term carrying capacity can be down to 50% of the original capacity when the pile was new. Because many quay-walls in Amsterdam are older than 500 years, this capacity degradation is considered. One can therefore assume a strength of 8 N/mm^2 against vertical loads, but it can also be considered against bending stresses of timber piles. [45]

To assess if the existing piles are still safe against failure, the following relationship has to hold [44]:

$$\sigma_{max} < \sigma_{strength} \quad (6)$$

Where σ_{max} is the maximum stress that occurs in the element, and where $\sigma_{strength}$ is the stress on which the material will fail. [44] σ_{max} is calculated as follows:

$$\sigma_{max} = \frac{M \cdot z}{I_{zz}} \quad (7)$$

Here, M is the maximum moment that exists on the element. z is the distance from the bending axis on which the moment is exerted to the sides of the element. In this case, z is the radius of the timber pile. I_{zz} is the surface inertia moment for the pile's circular cross section. [44]

The surface inertia I_{zz} can be calculated using its definition for a circular cross section [44]:

$$I_{zz} = \frac{1}{64} \pi D^4 \quad (8)$$

4.4 Common failure mechanisms for quay walls

To assess the stability of the historic quay wall construction, it is necessary to assess its resistance against failure along one of the possible failure mechanisms. In this chapter, the common failure mechanisms for quay walls will be discussed.

In the designs of pilot project Brouwersgracht, the common failure mechanisms of quay walls were listed, as shown in figure 4.23. These failure modes are geotechnical or structural, and are shortly described below [28].

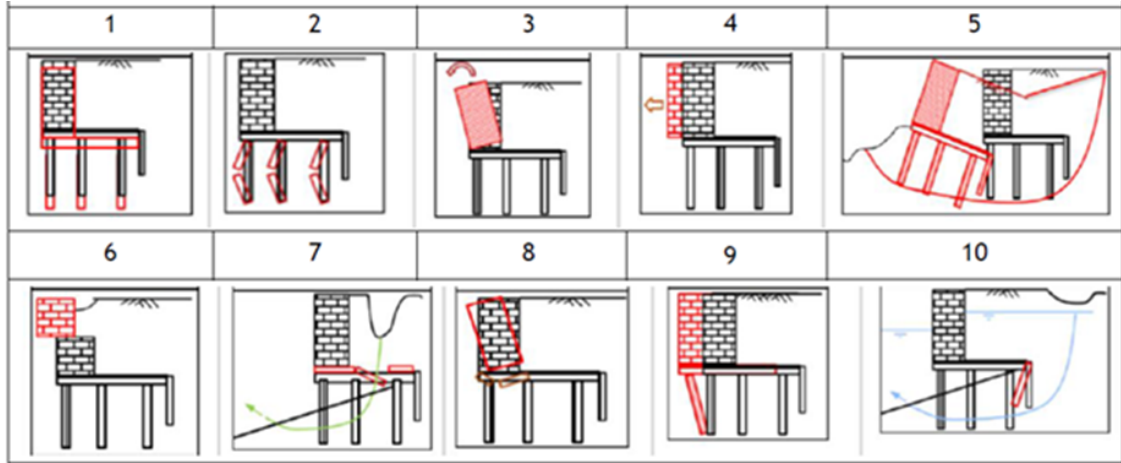


Figure 4.23: The common failure modes of a historic quay wall. [39]

1. Exceedance of bearing capacity of soil.
2. Structural failure of timber piles.
3. Toppling of gravity wall.
4. Horizontal displacement of gravity wall.
5. Exceedance of global stability.
6. Failure of gravity wall.
7. Failure of timber deck.
8. Failure of timber cross beams.
9. Horizontal displacement of gravity wall and failure of the soil.
10. Failure by erosion or piping.

Exceedance of bearing capacity of soil: This occurs when the load applied to the quay wall exceeds the bearing capacity of the supporting soil. It can lead to soil settlement and instability of the wall. [28]

Structural failure of timber piles: Quay walls often use timber piles for support. If these piles deteriorate or are subjected to excessive loads, they can structurally fail, compromising the stability of the wall. [25]

Toppling of gravity wall: Gravity walls rely on their weight to resist horizontal forces. If the wall's weight or the forces acting on it become unbalanced, the wall may topple over. [12]

Horizontal displacement of gravity Wall: The horizontal displacement of a gravity wall can occur due to excessive lateral forces from the backfill pressure. This displacement can lead to the wall moving away from its intended position. [46]

Exceedance of global stability: Global stability refers to the overall stability of the entire quay wall system, including the soil, foundation, and wall structure. If global stability is not maintained, it can lead to failure, often resulting from slope failures or sliding of the entire structure. [25]

Failure of gravity wall: A general failure of the gravity wall can occur when it is unable to resist the loads and forces acting upon it, leading to structural collapse or deformation. [28]

Failure of timber deck: If the quay wall has a timber deck, it may fail due to rot, decay, or overloading. [25]

Failure of timber cross beams: Timber cross beams are used to support the deck and distribute loads. Failure of these beams can affect the overall integrity of the quay wall and deck. [25]

Horizontal displacement of gravity wall and failure of the soil: This mechanism combines the horizontal displacement of the wall with soil failure. The soil may lose its ability to support the wall due to excessive lateral movement. [12]

Failure by erosion or piping: Erosion refers to the gradual wearing away of the soil or material around or beneath the quay wall. Piping is the formation of channels through which water can flow, potentially leading to soil erosion and wall instability. Both erosion and piping can undermine the wall's foundation and stability. [28]

4.5 Most sensitive phase

After the short preliminary assessment of Koningsgracht, the research should be narrowed down to a phase or element in the renewal method, which brings uncertainty or of which little information is available.

During the assessment, it became apparent that the support reactions barely change for the piles. When stiffness in the floor would be considered, which is present in reality, the support reactions of the piles would become more evenly distributed, resulting in an even lower support reaction change during Koningsgracht. This would indicate that no significant hazards are foreseen for the piles and floor.

Trench boxes are also widely used. They are known to be fairly easy to install, and have a reliable stability. [6] The depth of the excavation is also fairly low, hence it is expected that earth pressures are sufficiently low for the trench box to remain stable.

The geobag wall however is a construction of which not much information is available in literature. Geobags are often used for coastal protection purposes [33] or for soil reinforcements [21], but not often as a high retaining wall. The structure is interesting, for it consists out of multiple elements that could fail individually. For the reason that not much information can be found on the stability of a geobag wall, compared to studies about historic quay walls, piles and casings, it is considered as the most sensitive phase of Koningsgracht. In the continuation of this thesis, the reliability of the geobag wall is assessed, which will then directly represent the reliability of Koningsgracht. In the following chapter, the dimensions and conditions of the geobag wall will further be discussed, and its possible failure mechanisms will be presented.

5 Failure mechanisms and limit states

The geobag wall construction is considered to be the most sensitive and uncertain phase in Koningsgracht. To assess its stability, the failure mechanisms of the geobag wall need to be analyzed, along with their limit state equations. The considered failure mechanisms are horizontal sliding, overturning and rupture of geobag textile.

5.1 Geobag wall dimensions and conditions

Before discussing the failure modes of the geobag wall, it is important to understand in what form the geobag wall is considered in this thesis. This is done using the visualization of figure 5.1 below.

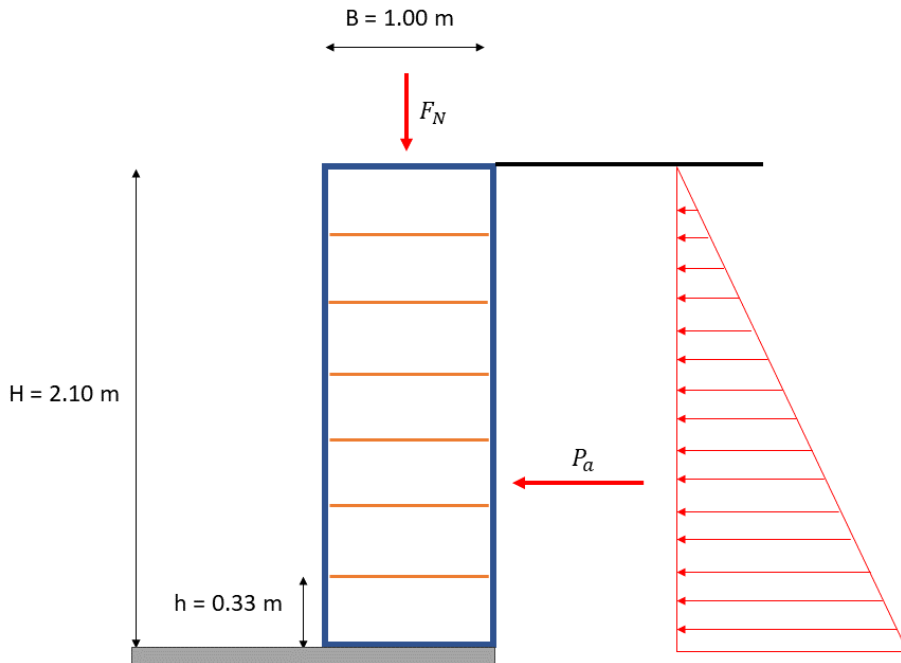


Figure 5.1: Visualization of geobag wall, with its seven segments, and the forces exerted on it.

As can be seen in figure 5.1, the geobag wall is considered to be a 2D structure, with a height of 2.1 meters and width of 1.00 meters. In chapter 4 of this thesis was discussed that the trench box width, in which the geobag wall is placed in, can have a width up to 1.60 meters. The reason behind selecting a smaller width for the geobag wall lies in the fact that there is an empty space present between the soil bags and the trench box, as well as accommodating for the presence of casings between the geobags, leaving less

room for geobags in the same wall dimensions. Opting for a larger width might result in an overestimation of the wall's weight, so a more cautious and conservative approach is preferred.

The wall consists out of individual soil bags. These bags are considered to be separate segments of the wall, with a segment height of 0.33 meters. This divides the wall into seven segments, and therefore seven interfaces. The geotextile of the geobags is jute, creating jute-jute interfaces between the wall segments. The flooring is made of concrete, creating a jute-concrete interface at the bottom of the wall. The geobag wall is a gravity retaining wall, meaning that its function is to prevent a backfill from sliding, using its own weight. This means that the wall is not attached to the flooring.

The main forces that are exerted on the wall or segments are also visualised, and it is important to understand how these forces can be approached with equations. The most important forces here are the normal force F_N resulting from the weight of the wall, and the force of the earth pressure P_a , resulting from the backfill pushing against the geobag wall. [32] How these forces will be considered in this thesis is discussed in the following subsections.

5.1.1 Normal force of the geobag wall

The first main force to discuss is the normal force F_N of the geobag wall. It can be calculated using the wall dimensions and the unit weight of the wall in the following equation [32].

$$F_N = H \cdot B \cdot \gamma_{wall} \quad (9)$$

Where H is the height of the wall, B the width of the wall, and γ_{wall} the unit weight of the wall.

5.1.2 Earth pressure

The total active thrust describes the force that is exerted from the soil behind the gravity wall. This is described by the following equation [32]:

$$P_a = \frac{1}{2} K_a \gamma_{soil} H^2 - 2cH \sqrt{K_a} + \frac{2c^2}{\gamma_{soil}} \quad (10)$$

Where, K_a is the active earth pressure coefficient, γ the unit weight of the backfill, H the height of the wall, and c the cohesion of the backfill.

The active earth pressure K_a can be calculated using the friction angle of the backfill soil ϕ in the Rankine equation [32]:

$$K_a = \frac{1 - \sin(\phi)}{1 + \sin(\phi)} \quad (11)$$

The above equation is only valid for a level backfill, a vertical wall face, and when it is assumed that there is no friction between the backfill and the wall. If one of these conditions is not met, the Coulomb equation should be used instead [12]:

$$K_a = \frac{\sin^2(\alpha + \phi)}{\sin^2(\alpha)\sin(\alpha - \delta)\left[1 + \sqrt{\frac{\sin(\phi + \delta)\sin(\phi - \beta)}{\sin(\alpha - \delta)\sin(\alpha + \beta)}}\right]^2} \quad (12)$$

Where β is the backfill slope angle, ϕ the internal friction angle of the soil, α is the wall slope angle from the horizontal with $\alpha > 90^\circ$ being a wall leaning towards the backfill, and δ is the angle of friction between the wall and the backfill. [12]

The friction angle δ of the wall-backfill interface describes the friction between the soil and the rough surface of the wall. For a smooth wall, $\delta = 0$. The friction on this interface results into a decrease of active earth pressure that the wall experiences. [23]

5.2 Failure by horizontal sliding of geobag wall

In this section, the failure mechanism of horizontal sliding is described. The stability of the geobag wall should not be assessed by considering the wall to be a monolithic structure, but by considering it to consist out of segments that can fail individually. In this thesis, the term 'local', refers to a part of the wall or a group of segments. Note that it does not imply that a segment moves with respect to all other segments, but it is considered that when an individual segment moves, all segments above it move along. The term 'global' refers to the monolithic wall, i.e. the wall as a whole.

Therefore, horizontal sliding will be discussed in two parts; one that describes horizontal sliding of the global monolithic construction, and one that describes the sliding of segments of the wall.

5.2.1 Global horizontal sliding

This failure mechanism describes the failure of the global construction, i.e. the wall as a monolithic structure, by horizontal displacement. The structure is stable against displacement when the driving forces $\sum F_d$ acting on the structure are smaller than then resisting forces $\sum F_R$. [46]

In the paper of Mustafa et al. (2022) [32] an approach was given to assess the resistance of a gravity wall to horizontal sliding in terms of a factor of safety. Since the monolithic structure of a geobag wall can be considered as a gravity wall, this approach should be applicable. It is stated that a gravity wall is able to retain soil masses using its own weight and the friction of the interface between the wall and the base. The factor of safety against horizontal sliding is given as follows [32]:

$$FOS = \frac{\sum F_R}{\sum F_D} = \frac{F_{fr}}{P_a} \quad (13)$$

In equation 13 above, F_R and F_D respectively are the summations of the resisting forces and the driving forces. F_{fr} is the friction force, and P_a is the total active thrust. [32] Due to uncertainties in the calculation method, the factor of safety against horizontal sliding for a gravity retaining wall is higher than 1.0, and generally lies between 1.5 and 2.0. [20] An illustration of the global stability against horizontal sliding is presented in figure 5.2.

The friction force F_{fr} from equation 13 is defined as the force that is just sufficiently high enough to prevent a relative motion between two objects [10]. The friction can be determined from the relationship shown below:

$$F_{fr} = \mu \cdot F_N \quad (14)$$

Where μ is the friction coefficient between two materials and F_N is the normal force on the movable object. [10] The dimensionless friction coefficient is relates to two materials

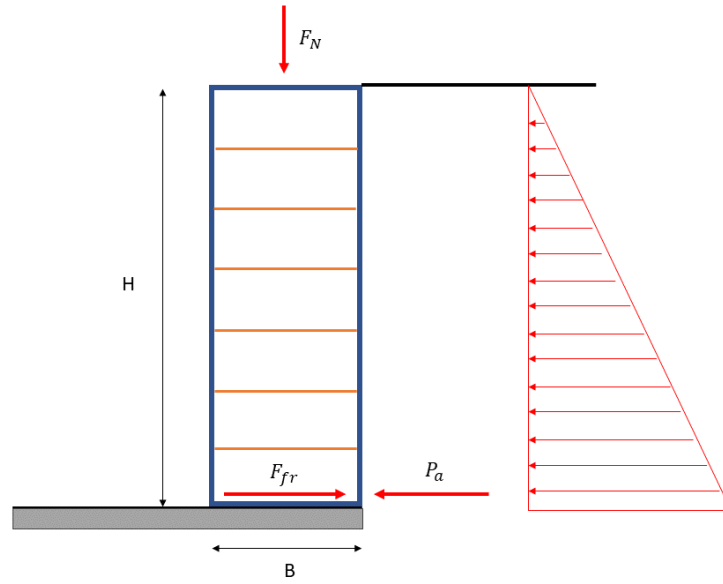


Figure 5.2: Global horizontal sliding of wall, along the bottom interface.

that are in contact with each other, and can be dependent on many factors, such as surface roughness and asperity interlocking. [10] Since the geobags are made out of jute, and the flooring is made of concrete, the bottom of the wall experiences a jute-concrete interface. The horizontal driving force from the soil pressure, and the normal force from the weight of the wall can be calculated, but the friction coefficient for a jute-concrete interface could not be found and is still needed in order to calculate the stability against horizontal sliding. In chapter 7, several experiments are listed that could retrieve this friction coefficient, and one of these experiments is conducted.

5.2.2 Local horizontal sliding

The horizontal sliding of a local part works similar to the sliding of the global construction, since only three differences are considered. A visualization of a local horizontal sliding scenario is given in figure 5.3 below.

First of all, the normal weight F_N of the wall decreases when moving to the top of the wall from the flooring, for each interface upwards as a smaller part of the wall above them. Every segment interface therefore should have its own normal weight assigned to. Note that the height of the wall is now represented by h , representing the height of the segment group that is assessed. Secondly, the backfill pressure is considered to increase with depth, meaning that the maximum backfill pressure on the wall is considered at the bottom interface, and the minimum at the top of the wall. Again, all segment interface are assigned their own backfill pressure, dependent on the wall height, and therefore

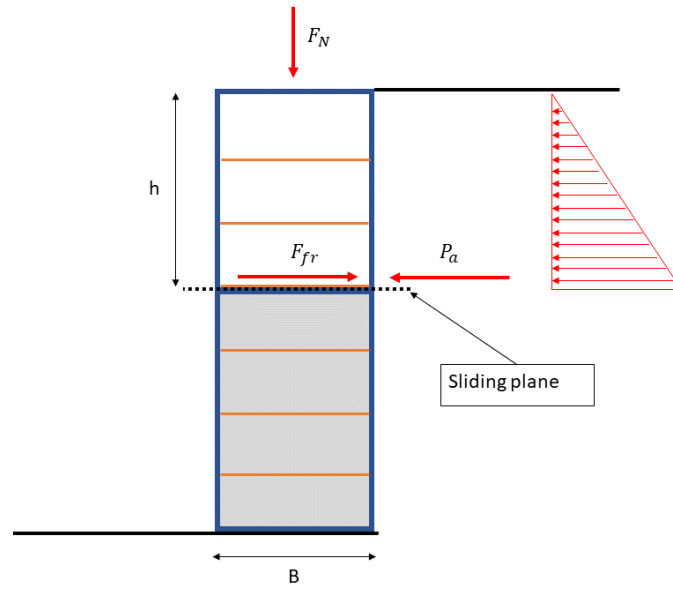


Figure 5.3: Local horizontal sliding of wall, along one of the interfaces.

the backfill depth. Thirdly, the monolithic structure has a jute-concrete interface at the bottom, while the segments interfaces above the lowest one have a jute-jute interface. This is because only the bottom geobags are in contact with the concrete floor, and all geobags above the first interface are in contact with other jute geobags. This means that only the bottom segment interface has a jute-concrete friction coefficient $\mu_{jute-concrete}$ assigned to, and all other interfaces a jute-jute friction coefficient $\mu_{jute-jute}$.

5.3 Failure by overturning of geobag wall

In this section, the failure mechanism over overturning of the wall is discussed. As in the previous section, the overturning failure mode is first considered for the global wall structure, where the monolithic wall is considered to topple over. Afterwards, overturning is discussed for the local segments.

5.3.1 Global overturning

The stability of a monolithic wall against overturning is can be described by comparing the overturning moment M_D , caused by the soil-pressure of the backfill, to the resisting moment M_R , caused by the weight of the wall. [12] The following equation can therefore be used to assess the stability against overturning:

$$FOS = \frac{\Sigma M_R}{\Sigma M_D} = \frac{F_N \cdot L_{arm,F_N}}{P_a \cdot L_{arm,P_a}} \quad (15)$$

Where F_N is the weight of the wall, L_{arm,F_N} is the length of the moment arm of the wall weight, P_a is the lateral force from the backfill, and L_{arm,P_a} is the length of the moment arm of the soil force. Because of calculation method uncertainties, the factor of safety against overturning for gravity retaining walls is higher than 1.0, and generally between 1.25 and 2.0 [20].

To assess the stability against overturning of the wall, one must first consider the point of overturning. For a gravity wall, this point can be considered to be at the toe of the wall, i.e. the bottom front corner. [12] The overturning moment is calculated by multiplying the lateral force from the backfill with the moment arm. This moment arm is the length from the point of application of the lateral forces, to the horizontal axis through the overturning point, i.e. the base of the wall. The lateral point of application is located at one-third of the wall height above the base of the wall, because the soil pressure is a triangular load. [12] The lateral point of application of P_a is therefore considered to be applied at $1/3H$. The backfill pressure P_a is calculated using equation 10 [15].

The moment of resistance is the weight of the wall, multiplied by the moment arm of the weight of the wall. Assuming that the wall is symmetrical, the point of application of the weight of the wall lies at half the width of the wall. The moment arm of the weight of the wall is the distance from the point of application to the vertical axis through the overturning point, i.e. half the wall width to the front side of the wall. [12] The points of applications for the resisting and overturning moments are visualized in figure 5.4.

There often exists friction between the wall and the backfill. This down-drag also contributes as a resisting force against overturning. [31] The active-earth pressure coefficient is affected by the friction angle between the wall and the backfill, as can be seen in the Coulomb equation (equation 12 with the symbol δ). The soil-wall friction angle δ is generally smaller than the internal soil friction angle ϕ , but never larger. [42]

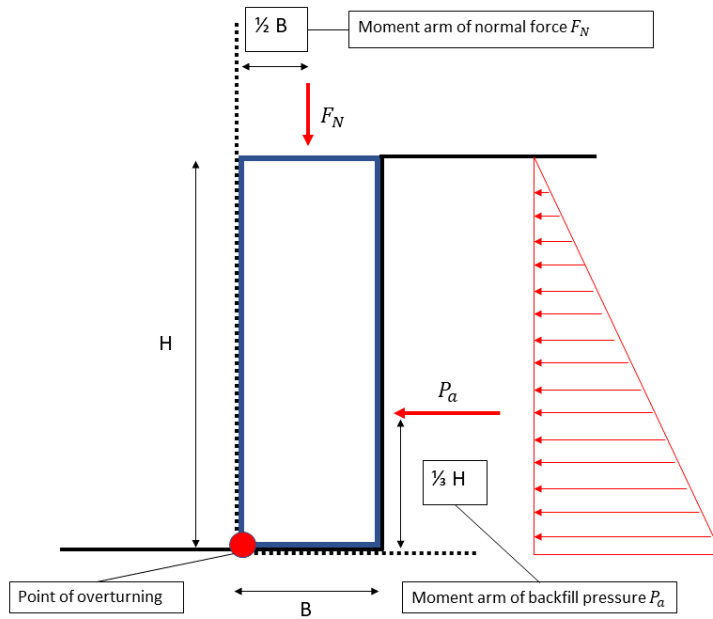


Figure 5.4: Global overturning of wall, with its moment forces and arms.

Note that the overturning of the geobag wall could result into a slope which creates favorable conditions for upper components of the wall to slide horizontally. This is an example of two modes inducing each other. A top component resting on a tilted lower component will experience less friction with its bottom interface than it would experience when there was no tilt. This is because the weight of the wall is not fully exerted on the interface, but a part is exerted along the slope axis. This lowers the resisting force against horizontal sliding.

The downward force at the interface between the back of the geobag wall and the backfill is neglected in this thesis to stay conservative. This is a force that could help resist overturning, exerted by the soil onto the wall in a downwards direction. However, the friction angle between the wall and the backfill is a parameter that is considered, situated in the calculation of the active earth pressure K_a (see equation 12). [23]

5.3.2 Local overturning of wall

The stability against overturning at a local level could be assessed in the same manner as the overturning stability of the monolithic wall, but now for a smaller part of the wall. Again, this means that segments at the top of the wall experience less wall weight, and a lower earth pressure. Additionally, the point of application is now at $1/3h$, where h represents the height of the group of segments that experiences the failure mode. An example of a local scenario is illustrated in figure 5.5. In this example, overturning is assessed at the third segment interface from the top of the wall, involving the top three segments.

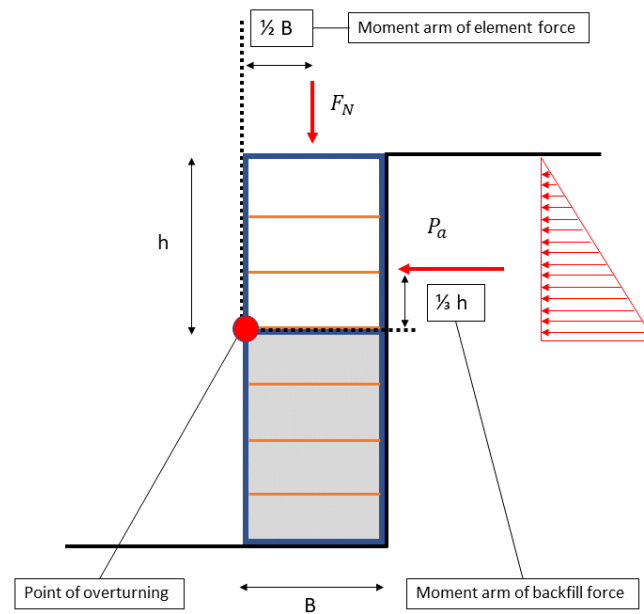


Figure 5.5: Local overturning of wall element, with its moment forces and arms.

In assessing the global stability against overturning for the monolithic wall, the assumption is a stable flooring. The segments beneath the potential overturning sections are also presumed to remain stable. Nonetheless, it is important to explore whether the top elements might topple more rapidly if partial overturning occurs in the lower elements. This evaluation can be conducted using equation 12, which computes the active earth pressure and incorporates the wall slope as one of its input parameters.

5.4 Failure by textile rupture of geobags

The geobag wall consists out of individual geobags of jute-geotextile containing sand. Jute might not be the strongest available geotextile, but it is a decomposable material that can be left in the subsurface after the quay wall is renewed. This allows for the permanent placement of the geobags, with no environmental harm.

The last failure mode of the geobag wall is the rupture of the jute geotextile of these individual bags. This rupture could be a result of tensions that build up in the geotextile from the weight of the wall, the pressure exerted by the backfill, or the frictional forces occurring at the interfaces between the bags or at the base of the wall. The generation of tensile stresses in the jute from the weight of the wall or from the backfill pressure is visualized by figure 5.6 [30].

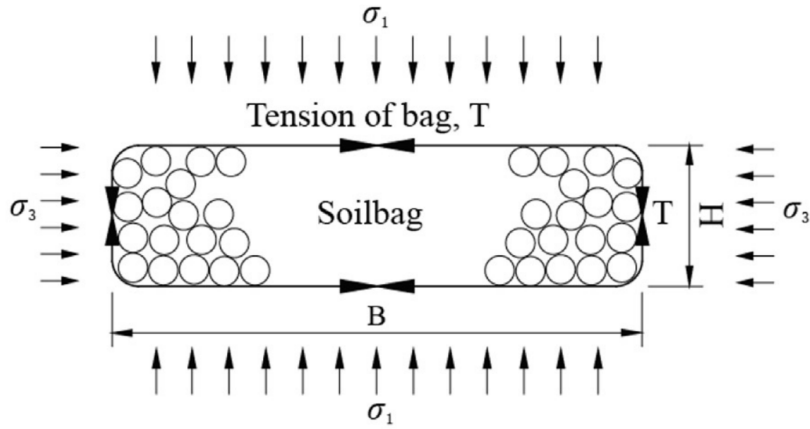


Figure 5.6: Tension in geobag due to vertical and horizontal stresses. [30]

The tensions in the geotextile from both the vertical and horizontal stresses can be calculated by using equations 18 and 19 [30].

$$T_{\sigma_1} = \frac{\sigma_1 \cdot B}{2} \quad (16)$$

$$T_{\sigma_3} = \frac{\sigma_3 \cdot H}{2} \quad (17)$$

Where T is the tensile stress in the jute, σ_1 and σ_3 respectively are the primary and secondary stresses exerted on the geobag, B the width of the geobag and H the height of the geobag. [30] σ_1 and σ_3 can be rewritten to the primary and secondary stresses that a geobag experiences in Koningsgracht, i.e. the weight of the wall and the backfill pressure, as shown in the following equations.

$$T_{F_N} = \frac{F_N \cdot B}{2} \quad (18)$$

$$T_{P_a} = \frac{P_a \cdot H}{2} \quad (19)$$

Because the tensile stresses can be a combination from both the weight of the wall and the backfill pressure, the active forces that work towards rupture are considered to be a summation of both tensions. The resisting force is the tensile strength of jute geotextile. Equation 20 shows the limit state relationship that is used for rupture of a geobag.

$$FOS = \frac{\sigma_{jute}}{\Sigma T} \quad (20)$$

Where σ_{jute} is the tensile strength of jute geotextile, and ΣT is the summation of tensions in the jute. Textile rupture could occur in any segment of the geobag wall. The height of the wall where a geobag is positioned determines the amount of weight that is exerted on it. As a conservative approach, the backfill pressure from the total wall length is used as the horizontal stress on all local geobags, regardless their height in the wall. The height of each bag is considered to be the height of a wall segment, i.e. 0.3 m, and the width of each bag is considered to be the full wall width, i.e. 0.66 m.

Note that the stiffness has an influence on the tensile strength of jute. While stiffness is neglected in this thesis, this relationship is later shortly discussed.

5.5 Additional factors of influence

5.5.1 Cohesion affecting horizontal sliding

In this thesis, the sandbag retaining wall is supported by a concrete floor. The interface between the jute material and the concrete is characterized as lacking cohesion. The backfill soil is considered to be little to non-cohesive as well, but this particular parameter can significantly influence the stability of the sandbag wall. [20]

According to Haddad et al. (2017), if the sandbag wall were to be situated atop cohesive soil rather than a concrete floor, equation 14 of this thesis, describing the frictional resistance against horizontal sliding, can be expanded to the following form [20]:

$$F_{fr} = \mu \cdot F_N + B \cdot c' \quad (21)$$

Where B is the width of the wall-floor interface, and c' is the cohesion of the interface. Please take note that this term differs from the internal cohesion c inherent to the soil. Importantly, it should be highlighted that c' is consistently a fraction of c [20]. The reason for this is because the cohesive bond at the interface between a cohesive soil and a non-cohesive material cannot attain the same level of cohesion as the bond between two cohesive soils.

5.5.2 Eccentricity

In the failure mechanisms described earlier in this chapter, it is assumed that the sandbag wall is positioned such that all vertical forces are perfectly distributed along the total wall width. According to Haddad et al. (2017) [20], the resultant vertical force, for example from the wall weight, should be exerted on the middle third of the wall width at the wall base in order for the normal weight to be optimally distributed. In the case that this resultant force is exerted on the first or last third of the wall width, the so-called eccentricity of the wall got sufficiently large to consider that the wall is slightly leaning forwards or backwards. This would then decrease the interface that the normal force has on the base, which directly decreases the friction force of the wall. This means that if the eccentricity of the wall becomes too large, the stability of the wall decreases. In this thesis, the eccentricity is considered to be zero, resulting in a perfect distribution of the weight.

5.5.3 Stiffness

Stiffness is a mechanical property that describes the resistance of a material or structure to deformation or the ability of a material to resist changes in its shape when subjected to an external force. [40] In essence, it measures how rigid a material or structure is when subjected to an applied load or force. A stiffer material deforms less than a less stiff or more flexible one under the same load. In figure 5.7 below, it can be seen that an object with a low stiffness deforms easily, where it also tends to follow the shape of the surface it is situated on.

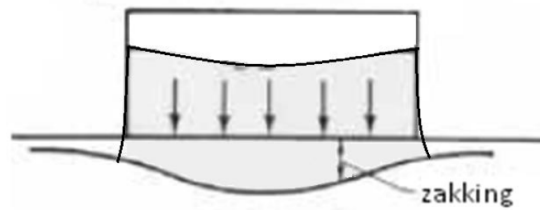


Figure 5.7: Example of a material with a low stiffness, deformed by the contours of the floor. [41]

Stiffness is often described by Hooke's Law, which states that the deformation (strain) of a material is directly proportional to the applied force (stress) within the elastic limit of the material. It can be rewritten for soils in the following manner.

$$\sigma = E \cdot \epsilon \quad (22)$$

Where σ is the stress on the soil, E the material property Young's modulus, and ϵ is the strain the soil undergoes due to the stress applied on it. Young's modulus E measures a material's resistance to elastic deformation when subjected to axial or tensile loads.

According to Sanyal (2017) [40], the stiffness prevents the deformation of a geobag in such a way, that a normal force is exerted upwards when a vertical load is applied on it. Note that this does not prevent tensile stresses generated in the textile. It is also known that an increase of stiffness of the geotextile increases the stiffness of stacked geobags. [26]. This results into a better redistribution of loads applied on the geobag wall, avoiding concentrations of stress which could lead to local rupture or deformation of a geobag. It was also shown that the deformation of stacked geobags from a vertical load resulted into a higher shearing resistance on a textile-textile interface, meaning that lateral displacement is less likely to occur after a compaction took place. [26]

Earlier in this chapter, the rupture of geotextile was presented as a failure mode for the geobag wall. Its limit state can be assessed using the tensile strength of jute. Note that this tensile strength is dependent on the stiffness of the material. This is described with the following relationship. [33]

$$\sigma_{jute} = K \cdot \epsilon_{max} \quad (23)$$

Where σ_{jute} is the tensile strength of the jute, K the stiffness, or bulk, modulus of jute, and ϵ_{max} the maximum strain that the material can resist. [33] The bulk modulus K can be calculated using:

$$K = \frac{E}{2 \cdot (1 - \nu)} \quad (24)$$

Where E is the Young's modulus and ν is the Poisson's ratio. This ratio represents the ratio of lateral strain to axial strain when a material is stretched or compressed. [33]

5.6 Movement behavior of segments

In this sub-chapter, the deformation behavior of the individual geobags is discussed by a comparison with dry stone walls. Two main deformation phenomena could occur, i.e. tilting and bulging of the wall.

5.6.1 Tilting of the wall

In the paper of McCombie et al. (2012) [31] real sized tests were described where dry stone walls were loaded with an increasing backfill pressure. This research is of interest, for it resembles the geobag wall with its individual components. The individual stones of which the walls consisted of deformed during the loading, affecting the global structure. It was observed that during the loading tests, individual stones rotated before there was any sliding of stones observed. Stones founded on top of rotating stones were horizontally displaced. This caused the top of the global structure to displace horizontally with respect to the bottom of the structure, as is visible in figure 5.8.

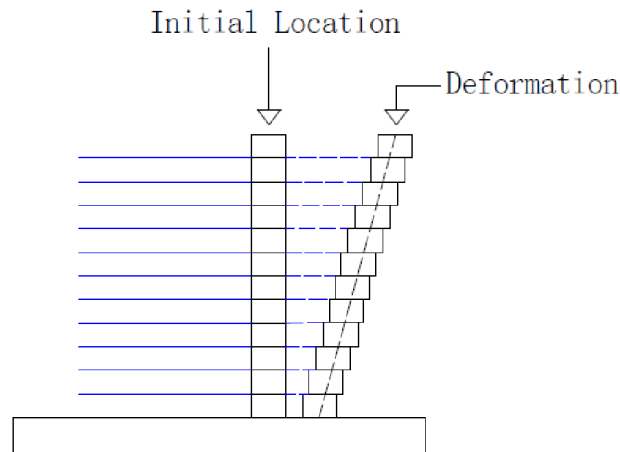


Figure 5.8: Tilting of an elemental wall as a result of horizontal pressure. [13]

The test showed that dry stone walls that were constructed in a denser manner showed less internal deformation and more global rotation of the wall than looser built walls. [31] This is because the stones in the denser wall share more interfaces and therefore have more friction with each other. This results into a higher internal tensile strength for denser built walls. Looser built walls showed more rotation of individual stones.

The tilting of the wall can contribute to an unstable state of the geobag wall. Since the top part of the wall has moved outwards, the weight of the wall is distributed differently than it was designed for. For this reason, the resisting moment can be less efficient, and therefore the wall could get more vulnerable against overturning. Additionally, the small displacements of the bags could result into a decrease in bag-bag interfaces. The friction between the bags could therefore decrease, which could drive the horizontal sliding mode.

Finally, the tilting of the wall contributes to the re-arrangement of tensions. When these tensile stresses pile up, they could result into the rupture of a geobag.

5.6.2 Bulging of the wall

As described in chapter 5.3.1, the backfill pressure can be assumed to be exerted on a specific height of the retaining wall, i.e. at one-third the height of the wall. For a monolithic wall, this phenomenon would only matter to determine the driving moment that the wall experiences, but for a componental wall it creates a new type of wall deformation, i.e. bulging. [31] A representation of bulging is shown in figure 5.9.

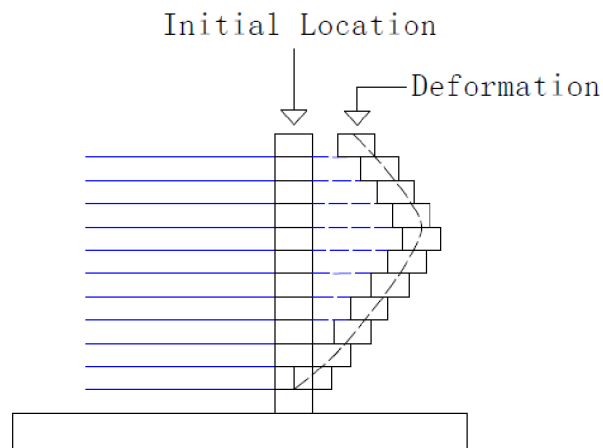


Figure 5.9: Bulging of an elemental wall as a result of horizontal pressure. [13]

For dry stone walls it was found that for low pressures, a wall would respond in a monolithic manner. For higher pressures, stones would start to rotate into a more stable position. If pressure increases even further, a shearing band starts to appear in the lower third of the wall. [15] This shearing band is the result of shearing stresses becoming larger than the friction between components.

Similar to tilting, bulging could result into tensions that rupture geobags, or it could result into the deformation of the wall such, that it drives overturning or horizontal sliding.

5.7 Geobag fault tree and failure mode parameters

The fault tree of the geobag wall is presented in figure 5.10 below. In this scheme, failure of the geobag wall system is considered when failure occurs along one of the wall's seven interfaces. Along each of these interfaces, the failure mechanisms horizontal sliding, overturning or textile rupture could occur when their limit states are reached, which all could individually lead to the failure of an interface.

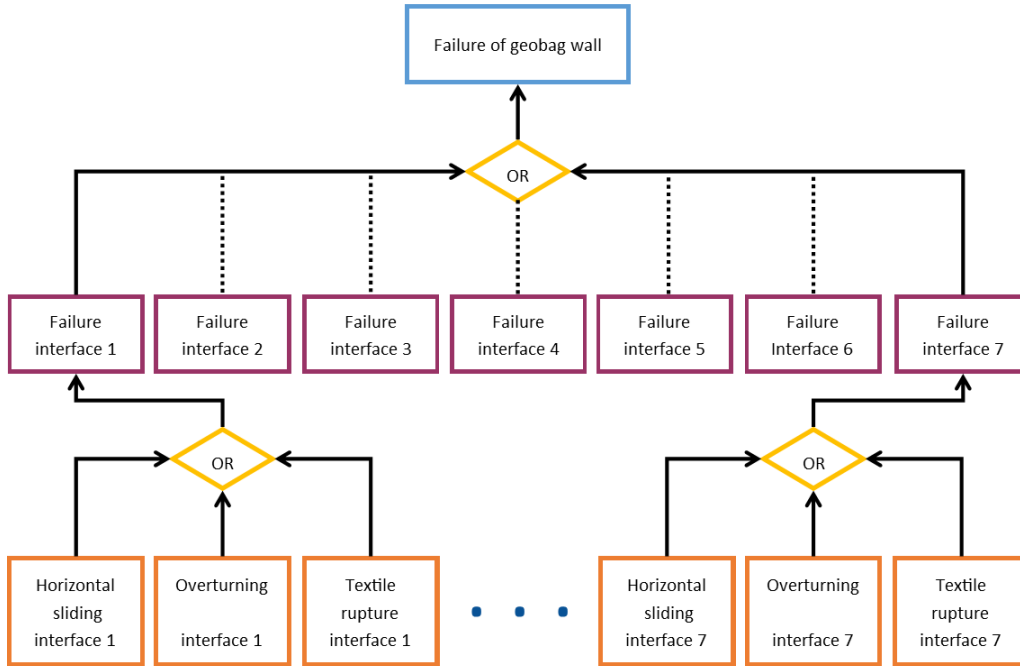


Figure 5.10: Fault tree of the geobag wall.

In table 5.1 below, an overview is shown of the parameters required to assess the potential failure modes of the geobag wall. When a parameter features in the limit state function of a failure mechanism, it is marked with an 'x'. Each parameter is color-coded to indicate the origin of their obtained values, i.e. green for values known from literature, yellow for values obtained from the design, orange for values acquired through testing, and blue for values dependent on the considered scenario.

Parameter	Hor. sliding		Overturning		Geotextile rupture
	global	local	global	local	
ϕ_{soil} friction angle soil ●	x	x	x	x	x
c_{soil} , cohesion soil ●	x	x	x	x	x
γ_{soil} , unit weight soil ●	x	x	x	x	x
γ_{wall} , unit weight wall ●	x	x	x	x	x
H , height wall ●	x	x	x	x	x
B , width wall ●	x	x	x	x	x
α , tilt wall ●	x	x	x	x	x
β , slope backfill ●	x	x	x	x	x
$\mu_{jute-concrete}$, friction coefficient ●	x				
$\mu_{jute-jute}$, friction coefficient ●		x			
$\delta_{jute-soil}$, friction angle jute-soil ●	x	x	x	x	x
σ_{jute} , tensile strength jute ●					x
<ul style="list-style-type: none"> ● : Values obtained from literature. ● : Values obtained from internal design documents. [37][34] ● : Values obtained from friction experiment, discussed in chapter 7.2. ● : Values based on scenarios. 					

Table 5.1: All failure mode parameters. The color codes state the origin of the parameter values that are used in this thesis.

5.8 Modelling methods

The failure mechanisms in this chapter could be assessed using several modelling methods. In this chapter, three methods will be shortly discussed.

5.8.1 Deterministic analysis

In deterministic analysis, all input parameters, such as soil properties, material strengths, and loading conditions, are assumed to have known and fixed values. These values are typically based on laboratory testing, historical data, or engineering standards.

Unlike probabilistic or stochastic analysis, where parameters are described by probability distributions, deterministic analysis uses single-point values for each parameter. For example, soil cohesion might be represented by a specific, constant value rather than a range of potential values. If a deterministic analysis is used, it often relies on conservative assumptions. [24]

The output of deterministic analysis is typically a single, deterministic result, such as a safety factor or a margin of safety.

5.8.2 Probabilistic analysis

Since, a deterministic analysis does not account for the inherent variability and uncertainties in geotechnical parameters and loading conditions, it may not fully capture the true range of possible outcomes in real-world scenarios. Probabilistic analysis provides a means to quantify the probability of failure associated with different outcomes. One can assess not only the most likely scenario but also the probability of various failure modes and their consequences. [24]

5.8.3 Finite Element Method

In geotechnical engineering, complex interactions between soils, structures, and various environmental factors occur. Finite Element Methods (FEM) allow for an accurate simulations of these systems. [17] FEM software like PLAXIS uses different soil models to simulate soil deformations depending on the stress distributions. As a result, one could retrieve the deformations that structures experience from soil-pressures, or one could assess if certain safety thresholds are exceeded.

For this thesis, it is decided to assess the geobag wall stability using a probabilistic analysis. As stated before, this allows for the explicit consideration of the parameter uncertainties by modeling them as probability distributions. In contrast, traditional FEM, like PLAXIS, typically employs deterministic values for parameters, which may not account for real-world variability.

Also, geotechnical systems, as the geobag wall, can fail in various ways, including sliding, overturning, and material rupture. Probabilistic analysis allows for the assessment of multiple failure modes simultaneously and for complex interactions between the parameters.

Probabilistic analysis can capture these interactions by considering correlations between variables. Lastly, a probabilistic analysis can be used to perform a sensitivity analysis, so that the most dominant parameters in the calculation of the geobag wall reliability can be identified. In the following chapter, probabilistic analyses will be discussed more thoroughly.

6 Probabilistic analysis

To assess the structural stability of a construction to following simple rule can be used:

$$R > S \quad (25)$$

Here, R represents the structural resistance, which contains the strength and durability of the materials used in the construction, where the load-bearing capacity of these materials are assessed, considering factors such as compressive strength, tensile strength, and shear resistance. The structural resistance acts as the foundation of a building's ability to withstand various external forces. [24]

The S term signifies the load on the structure over its entire lifespan. This includes both static and dynamic loads that the structure may encounter, such as dead loads (the weight of the structure itself), live loads (e.g. movable loads), environmental loads (e.g. wind), and any other possible forces. [24]

The limit state represents the point at which a structure or a specific component no longer meets its performance requirements. [24] This critical state, denoted as Z can be seen as a boundary value, defined as :

$$Z = R - S \quad (26)$$

In the above relationship, failure occurs when limit state $Z \leq 0$. In figure 6.1, this scenario is described by a line, functioning as a boundary between a safe structural state (with $R > S$) and failure (with $S > R$).[24]

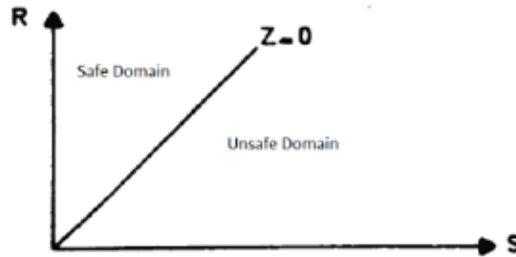


Figure 6.1: When the limit state equals 0, it describes the boundary at which the the loads exceeds the resistance of a structure. [24]

6.1 Reliability methods

To determine if a structure or component has reached its limit state using the relationship described in equation 26, there are five groups of reliability methods one can use. [24]

Level 0 methods

These consist out of the more simple approaches to calculate structure stability, for its completely deterministic. This means that for all parameters, one representative value is used without any uncertainty. [24]

Level I methods

These approaches are often called semi-probabilistic because they acknowledge uncertainties related to the limit state, but they do so in a straightforward way, using standard values. In many design codes, this is achieved by employing partial factors for specific input parameters. For parameters that help prevent the limit state from being reached, these partial factors reduce their values. Conversely, for parameters associated with actions that contribute to reaching the limit state, the partial factors increase their values. [24]

Level II methods

These methods are based on considering uncertain parameters using their mean value and standard deviation. The assumption is made that the uncertainty follows a bell-shaped normal pattern, meaning that there is a lower probability that a value farther from the mean will occur. Level II methods are also called FOSM methods, which stands for First Order Second Moment. The first order term stands for the mean value of a variable, while the second moment term stands for the variance, indicating how spread out the values of a random variable are from their mean. [24] The FOSM method ignores possible asymmetry around a mean and uses a linearized version of the distribution. These methods predict the spread of the outcome rather than calculating realizations to find the true spread. [8]

Level III methods

While Level II methods more an approximation of uncertainty, level III methods use models and complex mathematical computations to get a more exact uncertainty. An example of a level III method is the Monte Carlo method. This method is compared to FOSM in chapter 6.1.1. [24]

Level IV methods

Lastly, there are the level IV methods, which also include the cost of failure and the actual risk of a construction. When considering the risk, not only the probability of failure is assessed, but also the consequences of that particular failure. [24]

6.1.1 Comparing Monte Carlo to FOSM

It is of importance to understand the difference between the Monte Carlo method and the FOSM method in order to use them for a safety analysis. Both methods can make calculations using uncertain variables by using their mean and standard deviation. Monte Carlo then randomly samples values for these input variables based on their probability distributions. For each set of sampled values, the desired calculation is made. Each of these calculations with their own set of random samples are called realizations. One needs to specify how many realizations should be calculated. The product of the Monte Carlo method is a distribution of all calculated result values from each realization. From this distribution, one can analyze the probability of a certain result occurring. [24]

The FOSM method works in a fairly simpler manner, for unlike Monte Carlo it does not calculate realizations. It uses the same input distributions for each uncertain input parameter to approximate the distribution of the result. This is done by considering that the model behaves linearly and that result is a normal distribution. The advantage of FOSM over Monte Carlo is that it grants a quick estimation of the result without the need for extensive simulations, and it can also rapidly provide insights into which input parameters have the most significant impact on the FOS. However, because FOSM relies on estimates from the mean and standard deviations of input parameters, it may not fully capture the underlying probability distribution. [24]

Another important difference between the two methods is that the FOSM always gives the same distributions as a result, for its input does not change. However, Monte Carlo can generate new realizations each time the method is performed, resulting into unique result distributions. The more realizations the method calculates, the more consistent the result will become. Monte Carlo can also be used to simulate spatial variability in a model. For example, for different heights of a soil column, different samples of one friction angle distribution can be taken. In this manner, not only parameter uncertainty is taken into account, but also uncertainty about its homogeneity inside the model.

6.2 PDF and CDF

The terms involved in the safety verification process are not deterministic, meaning they are not represented by singular values. Instead, they are probabilistic in nature. The reason for this is that the strength of a construction can show variability due to differences in construction elements and potential deterioration over time. Similarly, loads acting on the structure may not only vary spatially but can also change over time. [24]

Considering equation 25, the objective in this context is to minimize the probability, denoted as P , of a specific event where both a low structural resistance R and a high load S occur simultaneously. In figure 6.2 below, a graph is visible on which the x-axis represents values for both S and R values. The y-axis represents the probability that certain values can occur. The graph shows that there is a low probability for high S values, and for low R values, but there is a possibility that S turns out larger than R , resulting in structural failure. [24]

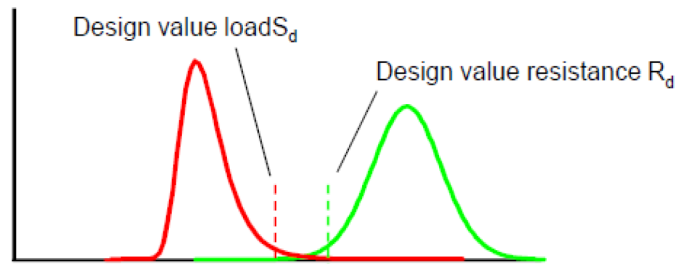


Figure 6.2: The probability where low resistances and a high loads occur should be minimized. [24]

The graphs in figure 6.2 are examples of so-called probability density functions, or PDF. It shows the probability of a random variable falling within a specific range of values. The x-axis of the graph represents the values of the variable, while the y-axis represents the probability density. The total area under the curve is equal to 1. [24]

While the PDF clearly shows which values have the highest possibility to occur, it is a bit more difficult to see what the probability exactly is that a certain value occurs. For this, the cumulative distribution function (CDF) is easier to use. The CDF provides information about the probability that the variable takes on a value less than or equal to a given value. An example of a CDF graph, which is unrelated to the PDF example shown above, is shown in figure 6.4.

The x-axis in figure 6.4 represents the values of the random variable, and the y-axis represents the cumulative probability. The cumulative probability at any point on the graph is the sum (for discrete variables) or integral (for continuous variables) of the probabilities up to that point. Discrete variables are countable integers, while continuous variables can be any value on an infinite range, often values obtained from measurements.

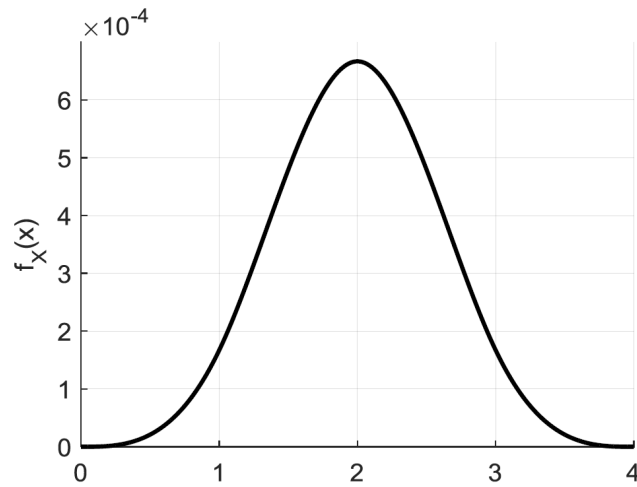


Figure 6.3: An example of a PDF, where the probability density (y-axis) is presented for every possible variable value (x-axis). The total area of the curve is equal to 1. [24]

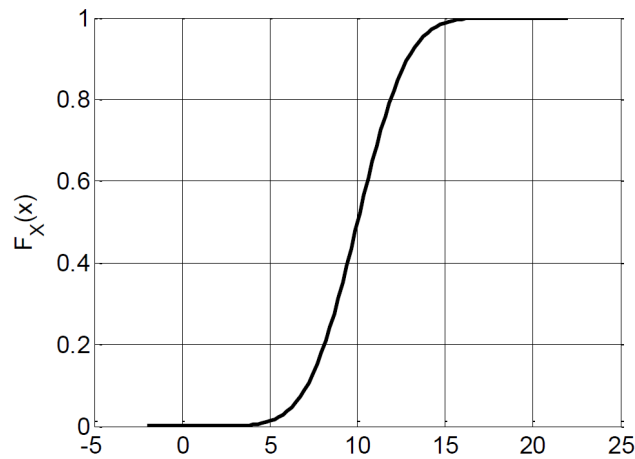


Figure 6.4: An example of a CDF, with the values of a variable on the x-axis and the cumulative probability on the y-axis. [24]

The CDF graph starts at zero on the left side of the x-axis, indicating that the probability of the random variable being less than the smallest value is zero. Using the example of figure 6.4, we can see that the probability of the variable having a value of 10 or lower than 10 is 0.5, or 50%. [24]

When creating a construction design, understanding the probability functions of both the resistances and the loads is crucial. This knowledge makes it possible to assess the probability of construction failure. In figure 6.5, the PDF's of both the resistance and load variables create zones of equal probabilities on the R-S graph. When adding the

limit state failure line, a safe and unsafe domain is created. The area of the zones that fall into the unsafe domain, compared to the part that fall into the safe domain, indicate the probability of failure. To lower the probability of failure, the zones can be moved away from the unsafe domain, by moving it up (increasing the resistances) or by moving it left (by lowering the loads) in ones design.

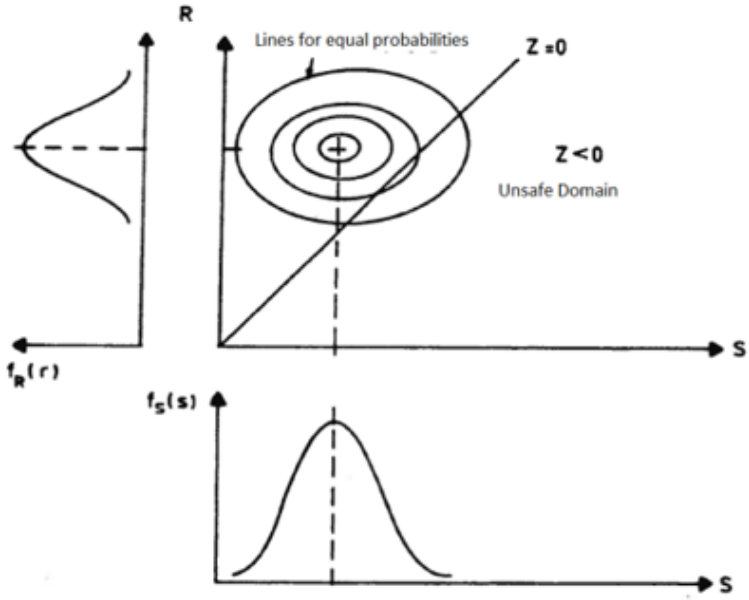


Figure 6.5: The probabilities of the R and S variables form the equal probability circles on the R-S curve. [24]

6.3 Mean and standard deviation

The PDF and CDF of some uncertain variable are constructed using information about the distribution of this variable. First of all, one should know the range of possible values, which can be used to calculate the mean of that data-set. Secondly, one needs the standard deviation (σ). The standard deviation is a way to measure how spread out or varied all possible values for a variable are around the its mean. [24]

To calculate the standard deviation, the mean is subtracted from all values in the data-set. This gives the so-called deviation. All deviations are squared to lose potential negative values, and the mean of the squared deviations is calculated. The square root of this mean gives one the standard deviation. [24]

Note that one standard deviation from the mean does not include all possible values. The empirical rule is as follows: one standard deviation from the mean includes 68.2% of all possible values, two include 95.4%, and three standard deviations include 99.7% of all possible values in the distribution. [24] This division is shown in figure 6.6, where the mean is represented by μ and the standard deviation by σ [27]:

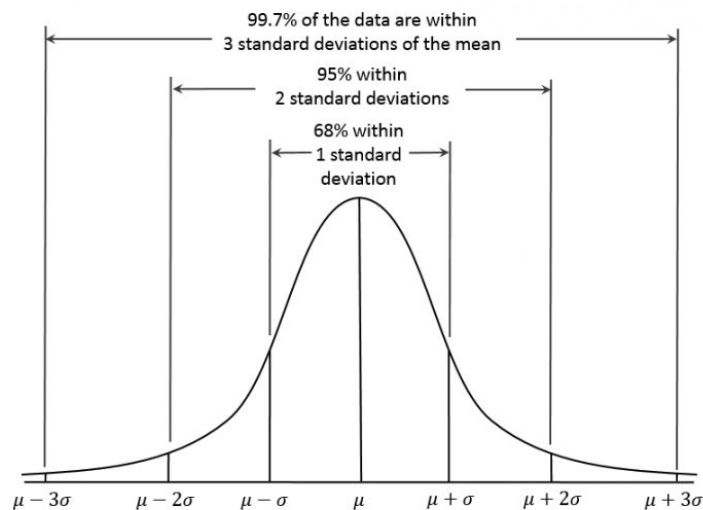


Figure 6.6: The percentage of values that occur within a standard deviation away from the mean. [5]

If the standard deviation is unknown, one can estimate it for a normal distribution using a known mean and range of possible values. This can be done by rewriting equation 27 for the so-called Z-score [27].

$$Z_{score} = \frac{X - \mu}{\sigma} \quad (27)$$

Where X is a certain value inside the data-set. The Z -score is linked to a specific value on the data-set and states how usual or unusual that value is. The mean has a Z -score of 0, and one standard deviation away from the mean has a Z -score of 1. [27]

When one desires a simple distribution of a range, with its mean in the middle, one could state that half the range equals to the distance from the minimum value to the mean, or the maximum value to the mean. Using this principle, equation 27 can be rewritten to:

$$\sigma = \frac{R}{2Z_{score}} \quad (28)$$

With R representing difference between the minimum and maximum value of the range of possible values, and Z representing the Z -score. Now the Z -score can be used to indicate what the probability is that the the 'true' value lies inside the input range. For instance, if one assigns a probability of 95.4% that the true value falls inside the range, the Z -score equals to two standard deviations, since the interval of 2 standard deviations from the mean is considered to include to 95.4% of all data. When one would be absolutely certain about the used range, one could use a Z -score of 3 in order to give a 99.7% probability that the value falls inside the range. [27]

6.3.1 Reliability index

As discussed before, the probabilistic distributions can be used to find the probability of failure of a limit state function. This probability of failure could be nicely represented by a percentage when the distribution approaches the limit state, but when a distribution occurs far above the limit state value, a percentage will approach zero or result into an inconvenient number with many decimal digits. When this occurs, the reliability index (β) can be used, which provides much clearer numbers. This variable states the number of standard deviations (σ) that lie between the mean (μ) and the limit state (Z). [9] This results into the following relationship.

$$\beta = \frac{\mu - Z}{\sigma} \quad (29)$$

In figure 6.7 below, the benefit of using the reliability index becomes apparent for small failure probabilities, since the values of the reliability index remain easily readable.

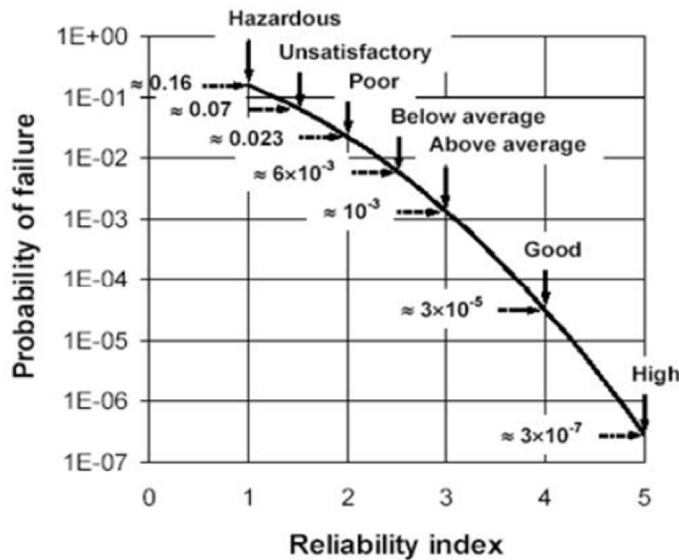


Figure 6.7: The reliability index can be used as a substitute to the probability of failure for lower probabilities. [3]

The reliability index can also be visualized in a distribution, as shown in figure 6.8.

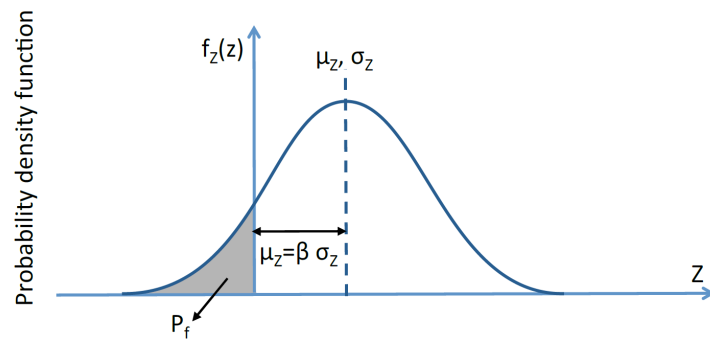


Figure 6.8: Visualization of reliability index. [8]

In figure 6.8 above, the limit state equals to a value of zero. The distance from the mean to the limit state value equals to the standard deviation times the reliability index. In this thesis, the reliability index will be listed with the reliability results, in order to state the magnitude of safety.

6.4 Correlations

It is possible that some parameters in a model have an influence on each other. The dependency of two stochastic variables can be described using the correlation coefficient (ρ). [24] This coefficient can have a value between -1 and 1, with the following meaning:

For $\rho = -1$, the parameters are mutually exclusive. The samples of one parameter decreases linearly in value when the sample value of the other parameter increases. A visualization is given in figure 6.9.

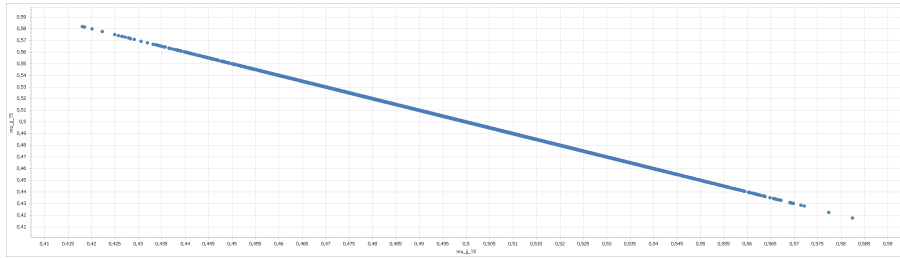


Figure 6.9: Many realizations of two parameters with $\rho = -1$.

For $\rho = 0$, the parameters are independent. The samples taken from both parameter distributions have no effect on one another. A visualization is given in figure 6.10.

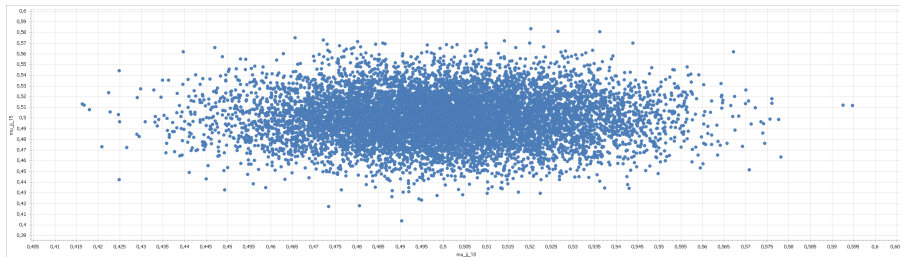


Figure 6.10: Many realizations of two parameters with $\rho = 0$.

For $\rho = 1$, the parameters are dependent. The samples of one parameter increases linearly in value when the sample value of the other parameter increases. A visualization is given in figure 6.11.

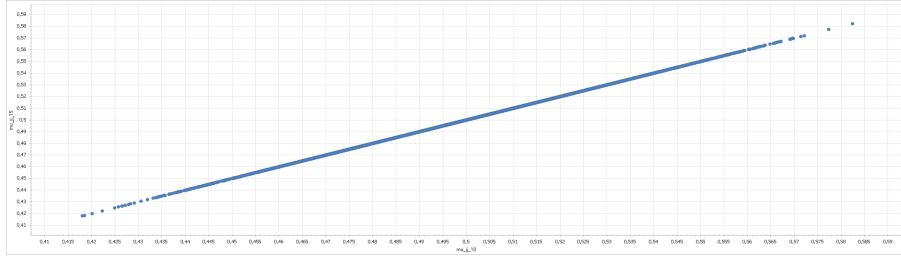


Figure 6.11: Many realizations of two parameters with $\rho = 1$.

For $\rho = 0.5$, the parameters are slightly dependent. The samples of one parameter tend to increase in value when the sample value of the other parameter increases. This is noticeable for larger value changes, but for small sample changes the parameters seem independent. The more the coefficient of correlation approached -1 and 1, the more linear two parameters affect each other in respectively a negative and positive manner. A visualization is given in figure 6.12.

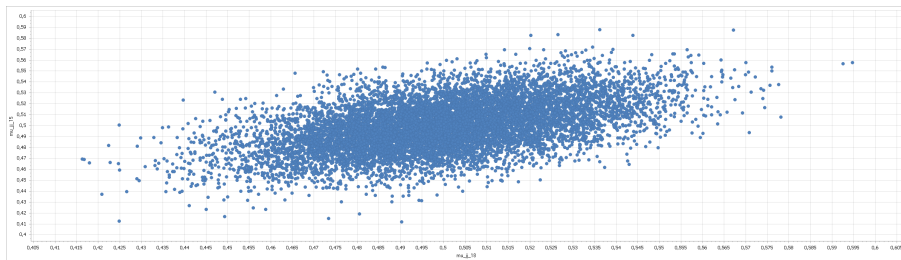


Figure 6.12: Many realizations of two parameters with $\rho = 0.5$.

6.5 System reliability

While chapter 6.1 discussed how to determine the reliability of limit states, one should also be able to determine the reliability of a system. The reliability of a system, comprising various events, refers to the system's overall ability to perform its intended function without failure under specific conditions. It takes into account the probability of each individual event failing. [24] To recover the system's probability of failure, one should first consider if the failure modes in the system are in series or in parallel with one another. A series system means that when one failure mode occurs, the system fails. With a parallel system, other components can still compensate for the occurred failure mode, and therefore more or all failure modes need to occur in order for the system to fail. Series and parallel systems are visualized in figure 6.13 below. [24]

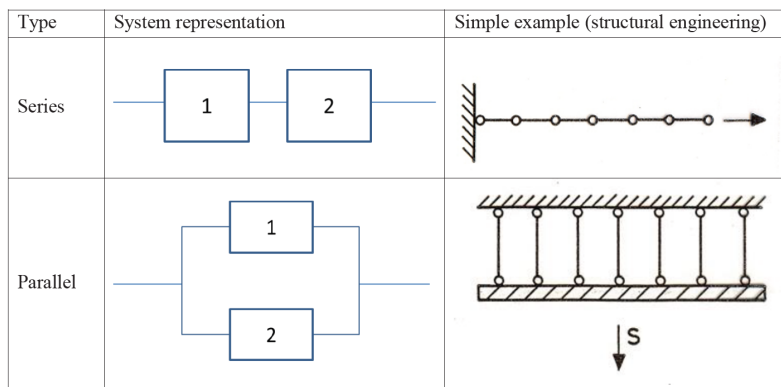


Figure 6.13: A visualization of series and parallel systems. [24]

The system's reliability can be further illustrated with a Venn diagram. The diagram consists out of a box, representing all possible outcomes, and circles, where the circles represent event probabilities. Imagine a point randomly falling within the box: if it lands in an event circle, that event occurs. Larger circles mean higher event probabilities. A Venn diagram helps grasp total system failure probability based on individual event probabilities. The events in a system can be mutually exclusive, independent or dependent. An example of Venn diagrams for these three types of systems is shown in figure 6.14. [24]

Mutually exclusive events are events that have no influence on one another, and that cannot occur simultaneously. An example of such events is the probability that heads or tails is obtained from a coin toss. The occurrence of one of these events does not affect another, and it is impossible that both events occur simultaneously. For a series system, the system's probability can be calculated by the summation of the probabilities of the individual events. For a parallel system, it is impossible to have mutually exclusive events, since the events cannot occur simultaneously. [24]

Independent events are events that do not affect one another, but they can occur simultaneously. An example of two independent events is retrieving heads from a coin toss and


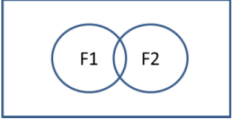

Case	Mutually exclusive	Independent	Dependent
Correlation coefficient, $\rho_{z_1, z_2} =$	-1	0	1
Venn diagram			
System failure probability $P(F)$	$P(F_1) + P(F_2)$	$P(F_1) + P(F_2) - P(F_1) \cdot P(F_2)$	$Max(P(F_1), P(F_2))$

Figure 6.14: An example of systems with mutually exclusive, independent or dependent events. [24]

obtaining 6 from a die throw. For a series system, the system's probability can be calculated by the summation of the probability of the individual events, minus the probability that both events occur, represented by the overlapping part in the Venn diagram. This is because the summation of the two probabilities include the overlapping part twice. For a parallel system, the probability equals to the probability that both events occur. [24]

Dependent events are events that affect one another, and that can also occur simultaneously. An example is two events that are based on the same parameter sets. In the Venn diagram, this type of reliability is visualized by a small event circle inside a larger one. The probability of the system equals to the probability of the largest circle, since that represents all space in the Venn diagram where events occur. The event with the highest probability between two dependent events determines the probability of the system. For a parallel system, two events need to occur simultaneously. This implies that the probability of the system equals to that of the event with the lowest probability. [24]

6.5.1 System reliability of geobag wall

With this knowledge, the probability that the geobag wall fails can be determined from the probabilities of the individual failure modes, i.e. horizontal sliding, overturning and geotextile rupture. To do so, one should first consider if these different modes are in series or parallel to one another. Since the geobag fails if only one mode occurs, the geobag wall can be defined as a series system. Since all three failure modes could occur simultaneously, the events can be either independent or dependent. However, since the modes are largely based on the same parameter set, it can be stated that the failure modes of the geobag wall are dependent modes. Since the geobag wall is a series system with dependent modes, the probability of the system is equal to the maximum probability of the three events. For example, if there is a 12% probability of overturning, a 5% probability of horizontal sliding, and a 1% of geotextile rupture, there is a 12% probability that the system will fail.

7 Geobag experiments

In this chapter, potential experiments to determine the coefficient of friction are presented. This is because there could not be a value found in literature for the coefficient of friction for a jute-concrete interface. This is followed by a section where one of these experiments is performed, and its results are discussed.

7.1 Potential experiments to determine coefficient of friction

Three tests will be described below in which the angle of the friction interface α can be obtained. One of these tests can even be used to obtain μ directly. These tests are the direct shear test, the pullout test and the slope friction test. [40] The first two tests are visualized in figure 7.1.

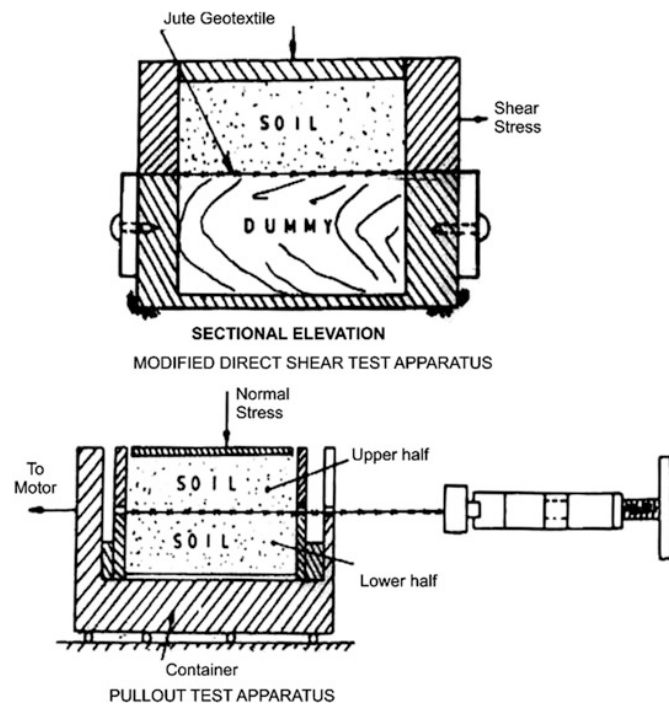


Figure 7.1: Visualization of direct shear test and pullout test. [40]

The direct shear test contains two boxes placed on top of one another, of which the top part can move along the interface. Jute geotextile can be placed on the fixed bottom half and a concrete sample in the upper half can then move horizontally along the interface. [40] For multiple different compressive stresses, the maximum shear stresses can be obtained, which can be plotted against each other. From a best-fit line, the cohesion and the friction angle of the interface α can be determined. From the slope of the line, the coefficient of friction μ can be determined directly. [40] If μ is retrieved directly, equation 33 could then be used to validate the value.

In the pullout test, a piece of jute geotextile could be placed in between two box halves containing concrete samples. [40] Under a constant displacement the jute sample is pulled out where the required pullout force is retrieved. The friction angle of the interface can be obtained with the pullout stresses at different compressive stresses. [40]

In the paper of Mahmood et al. (2000) [29] it was found that for higher normal stresses on a movable object, lower coefficients of friction of the interface were obtained. Also, for increasing tensile strengths of the jute geotextile, an increasing friction coefficient of the interface was also found. The latter finding needs a side note, for the lowest friction coefficient was obtained using the highest tensile strength. While this appears to contradict the relationship, it is thought that this occurred due to shearing failure in the soil close to the material interface, rather than due to the friction at the interface itself. [29]

The third test to be described is one that RHDHV has performed in the past. This test was used to obtain the coefficient of friction of the interface between a certain material and concrete. It is conducted using a slope covered with the material, with a concrete tile on top. By slowly increasing the angle of the slope it eventually reaches a value where the friction between the tile and the material is smaller than the force driving the tile down, resulting into the sliding of the tile. This angle corresponds to the α in equation 33, so that the coefficient of friction can be calculated. [35]

The load of the tile was altered throughout the test in order to test the independence of the coefficient of friction to the normal force on the interface. This theory was confirmed based on the results obtained.

7.2 Friction experiment

The coefficient of friction can be determined using the relationship with the slope of the friction interface, which can be derived from figure 7.2 and equation 14.

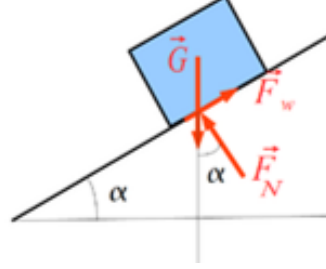


Figure 7.2: Principle of friction. [35]

From figure 7.2, the following relationship becomes apparent:

$$F_{fr} = G \cdot \sin(\alpha) \quad (30)$$

Where G is the gravitational force on the block, and α is the angle of the friction interface when the friction is just sufficient to keep the block into place. From figure 7.2 to write component G as:

$$G = \frac{F_N}{\cos(\alpha)} \quad (31)$$

this can be used to rewrite equation 30:

$$F_{fr} = \frac{F_N}{\cos(\alpha)} \cdot \sin(\alpha) = F_N \cdot \tan(\alpha) \quad (32)$$

Combining this with equation 14 gives the relationship between the coefficient of friction μ and the slope of the friction interface α :

$$\mu = \tan(\alpha) \quad (33)$$

According to Bouazza et al. (1994) [11], the relationship from equation 33 can be complemented by an adhesion component, if this exists on the friction interface:

$$\mu = C_a/\sigma_N + \tan(\alpha) \quad (34)$$

Where C_a is the interface adhesion, σ_N is the normal stress on the movable object, and α is the internal friction angle of the sliding interface, i.e. the slope of the friction interface.

While the friction coefficient of a jute-jute contact is known from literature studies, with a value commonly between 0.45-0.54 [40], the friction coefficient of a jute-concrete contact is unknown. [11] Since the adhesion between jute and concrete can be considered to be zero, the angle α is the only unknown. This means that either the friction coefficient of the interface μ needs to be determined directly, or by retrieving the friction angle of the interface α and apply equation 34.

To determine the unknown coefficient of friction of the jute-concrete interface, a simple test has been performed. The test is based on the inclination on which an object starts sliding off a surface. This angle of mobilization (α) has a relationship with the coefficient of friction (μ) with the following relationship, defined in chapter 5.2.1 of this thesis:

$$\mu = \tan(\alpha) \quad (35)$$

7.2.1 Friction test set-up

To perform the test, a smooth wood plank was used for the inclined surface. Three concrete bricks acted as the sliding object on the surface. These materials are shown in figure 7.3 The concrete bricks also had a fairly smooth surface, as shown in figure 7.4.



Figure 7.3: A smooth wood plank and three concrete bricks.

Around the wood plank, jute was tightly attached so that the brick and the plank acted as a jute-concrete interface. It was now a matter of increasing the tilt of the plank until the brick started to slide down. The inclination was simply measured by using an accurate tilt measuring app on a phone, which was attached to the plank. Figure 7.5 shows the final set-up.

7.2.2 Friction test validation

Validation is a crucial step in any process or study that involves collecting and analyzing data to arrive at meaningful results. Without validation, there is a risk of drawing in-



Figure 7.4: The smooth surface of the concrete bricks.



Figure 7.5: Jute was attached to the inclined wood plank. The tilt, measured by the phone, was increased until motion of the brick.

correct conclusions based on unreliable information. The friction test has been tested on reliability using two methods.

The first validation method relied on the principle stating that the friction coefficient remains constant regardless of the normal force applied to the inclined surface. To test this, various brick weights were used, aiming to observe if the inclination at which the brick began sliding remained unaffected. The following weights were used for the experiment:

No. bricks	Weight
1 brick	3.0 kg
2 bricks	6.0 kg
3 bricks	8.0 kg

Table 7.1: Weights used during the experiment.

The second validation method relies on test results. As there was no pre-existing information about the concrete-jute interface in the literature, the friction coefficient obtained from the test could not be directly compared to existing literature values. However, literature does provide the jute-jute coefficient of friction. To address this, a jute textile was wrapped around a concrete brick, creating a jute-jute interface. By conducting the test in this configuration, the friction coefficient between the jute materials can be validated, thereby establishing the reliability of the test results. The jute-jute interface set-up is shown in figure 7.6.



Figure 7.6: By wrapping a concrete brick with jute, a jute-jute interface is created.

7.2.3 Results friction experiment

The results of the friction test, conducted to retrieve the coefficient of friction for a jute-concrete interface, are presented in table 7.2. The table lists the value of the angle of mobilization (α) per brick weight used. The mean per brick weight is then presented, together with the corresponding coefficient of friction (μ).

To validate the experiment, a jute-jute interface was tested as well. In table 7.3, the mobilization angles are shown for a brick wrapped in jute.

According to Sanyal et al. (2017) [40], the coefficient of friction of a jute-jute interface can have a value between 0.45 and 0.54. This corresponds to angles of mobilization between 24° and 28° . The highest possible value of 28° corresponds with the lowest value obtained from the friction test, as indicated in table 7.3. However, it should be noted that the

Trial	1 brick	2 bricks	3 bricks
1	33°	34°	32°
2	35°	31°	34°
3	34°	31°	30°
4	35°	32°	33°
5	34°	34°	31°
Mean α	34.2°	32.4°	32.0°
Mean μ	0.68	0.63	0.62

Table 7.2: Angle of mobilizations (α) per weight, with their mean and the corresponding coefficient of friction (μ).

Trial	1 brick
1	33°
2	31°
3	33°
4	31°
5	31°
6	28°

Table 7.3: Angle (α) of mobilization for the jute-jute validation.

majority of the friction test results for the jute-jute interface surpass those reported in the literature. The potential reasons for this discrepancy are stated in the discussion of the friction experiment within chapter 7.2.4.

The coefficient of friction is needed to do the probabilistic analysis of the sand bag stability. It can be seen that the mean coefficient of friction of the jute-concrete interface decreases throughout the test, as well occurs with the jute-jute interface. The lower jute-jute values were validated, so therefore it is decided that the lower jute-concrete values are more reliable, because it is believed that the jute had to wear down slightly before realistic friction coefficients could be measured. Therefore, it is decided to look at the final column of the experiment, resulting in a coefficient of friction range between 0.577 and 0.675, and a mean of 0.620 after applying equation 35. To determine the standard deviation, the range of the values is used in equation 28, resulting in a standard deviation of 0.025.

7.2.4 Discussion friction experiment

Upon analyzing the friction test results, a noticeable trend emerges: the angles of mobilization decrease progressively throughout the experiment. The potential cause for this observation could be the variations in brick weight. However, the established relationship between the angle of mobilization and the coefficient of friction suggests that it remains independent of the normal force on the surface. Consequently, one would expect that the heavier bricks should not slide down any earlier than the lighter ones, based on this principle. Several other factors can influence friction test results.

First of all, the surface roughness could have played a role. The roughness of the surfaces in contact can significantly impact friction. Smoother surfaces generally exhibit lower friction, while rough surfaces can lead to higher friction. It could be possible that there was a local difference in roughness along the jute surface, and not all trials had the same brick starting position.

Secondly, the wear and tear principle could have a big effect on this experiment. Repeated slides or prolonged contact between surfaces can cause wear and affect the material, and the coefficient of friction. When the weight was increased to 3 bricks, it had already undergone 10 trials of sliding. These repeated trials might have worn down the jute surface, resulting in a smoother interface. This plausible explanation can explain the lower coefficient of friction observed for the heavier weight.

These factors could also account for the significant difference in the angle of mobilization between the first and last trials during the jute-jute validation. The jute surface on the wood plank might have worn down due to the previous trials, whereas the jute used on the brick was new and still unaffected. The robust fibers of the fresh jute might explain the higher friction coefficient observed at the beginning of the jute-jute validation experiment. This would mean that the friction coefficient from the worn down jute is closest to reality, since it matches with literature. For this reason one could decide to use the lower coefficient of friction for the jute-concrete interface as well. Since a low coefficient of friction results into low friction forces, this would also be the most conservative approach for a stability analysis.

8 Methodology

8.1 Probabilistic Toolkit

To determine the factor of safety for the sandbag wall's failure mechanisms, accurate values for all essential parameters are required. While certain parameters, like wall height, are known precisely, others are subject to uncertainty, requiring a probabilistic analysis. To handle these probabilistic variables effectively, the Probabilistic Toolkit of Deltares proves valuable. The toolkit allows the creation of a Python script within the toolbox to create the model. Deterministic variables are defined in the model code, and the toolbox allows for the specification of probabilistic inputs. Additionally, users need to define the probabilistic output that is desired. An example of the input screen is shown in figure 8.1, where the probabilistic input and output variables are defined separately, shown by the red markings.

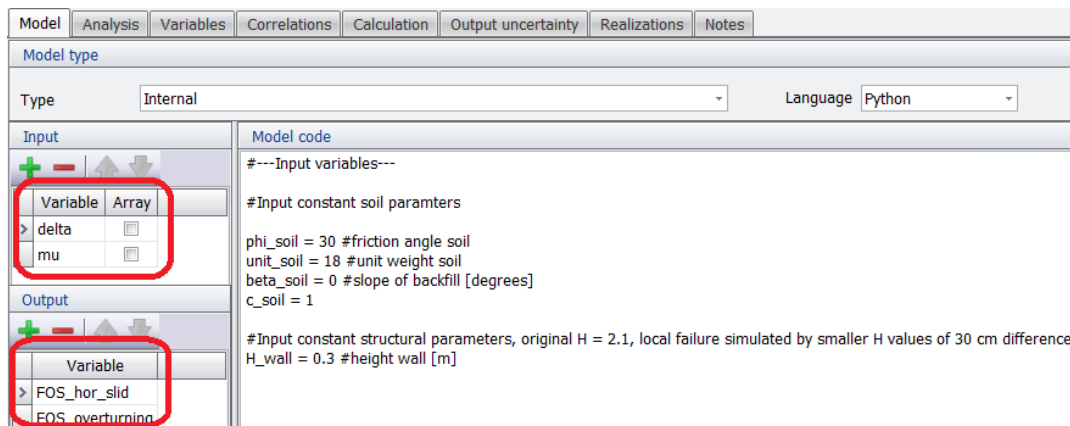


Figure 8.1: The model is made using an internal Python script, where the probabilistic input and output variables can be defined separately, as shown by the red markings.

The type of distribution needs to be defined for every probabilistic variable, e.g. a normal distribution, a triangular distribution or a uniform distribution. This decision depends on the information one has about variable, e.g. if the probability remains constant around the mean of a value, or if the probability decreases around the mean of a value. After choosing the type of distribution, the user needs to define the mean of the distribution, and the standard deviation of this distribution. When the user entered these distribution characteristics, the PDF and CDF of this variable is shown by the toolkit. An example of the variable distribution input is shown in figure 8.2.

When the variables are determined, one can set the correlations between parameters. These can be values from -1, for mutually exclusive parameters, to values of 1, for dependent parameters. The value 0 is used for parameters that are independent from each other, i.e. that have no correlation. An example of the correlation input screen is given in figure 8.3 below.

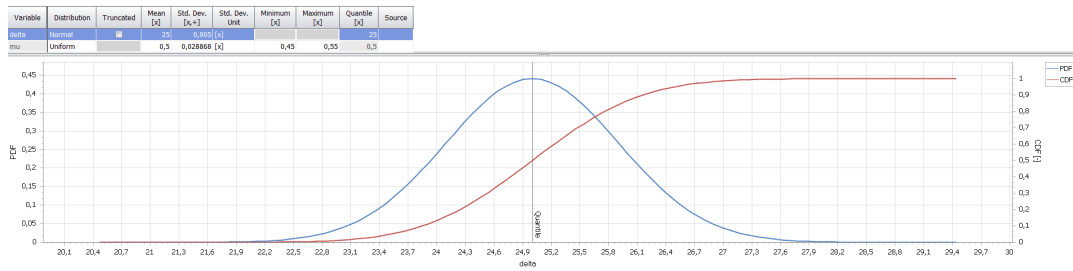


Figure 8.2: The type of distribution needs to be defined for all probabilistic variables.

Variable	mu_jj_18	mu_jj_15	mu_jj_12	mu_jj_09	mu_jj_06	mu_jj_03
mu_jc	0	0	0	0	0	0
mu_jj_18	1	0,5	0,5	0,5	0,5	0,5
mu_jj_15	0,5	1	0,5	0,5	0,5	0,5
mu_jj_12	0,5	0,5	1	0,5	0,5	0,5
mu_jj_09	0,5	0,5	0,5	1	0,5	0,5
mu_jj_06	0,5	0,5	0,5	0,5	1	0,5
mu_jj_03	0,5	0,5	0,5	0,5	0,5	1

Figure 8.3: An example of the correlation input screen of the Probabilistic Toolbox.

Now, the calculation method can be chosen. If the Monte Carlo method is used, one can state the amount of realizations that is desired. When the model is implemented, all variables are defined, the correlations are set, and the calculation method is determined, the calculation can be performed. The output consists out of all the probabilistic variables that were requested in the input screen. These output variables are presented as distributions, with their PDF and CDF graphs, as the example shows in figure 8.4.

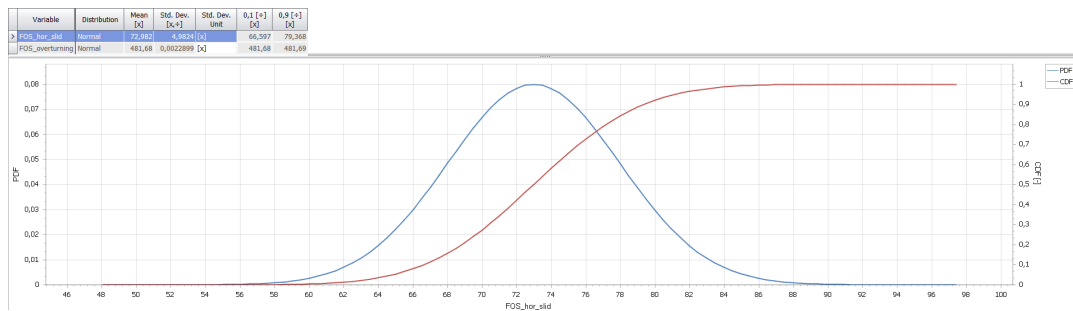


Figure 8.4: The requested output variables are displayed as distributions.

8.2 Parameters

The values of the parameters used for the assessment of the sandbag stability are all listed in this section. The geological parameters are general values for sand occurring in Amsterdam [28]. These values are mostly based on loose sand from the NEN table for soil parameters, which is presented in Appendix A. The values corresponding to the sandbag wall dimensions, its tilt and the slope of the backfill all originate from the Koningsgracht design. The strength and friction parameters originate from literature, except for the coefficient of friction of the jute-concrete interface, which originates from the friction experiment of chapter 7. All deterministic values are listed in table 8.1. These values are also considered as mean values.

Parameter	Value	Description
ϕ_{soil}	30.0°	Friction angle of soil [28]
c_{soil}	1.00 kPa	Cohesion of soil [28]
γ_{soil}	17.0 kPa	Unit weight of soil [28]
γ_{wall}	17.0 kPa	Unit weight of wall
H_{wall}	2.10 m	Height of wall
B_{wall}	0.66 m	Width of wall
α	90.0°	Tilt of wall
β	0.00°	Slope of backfill surface
$\mu_{jute-concrete}$	0.62	Coeff. of friction jute-concrete
$\mu_{jute-jute}$	0.50	Coeff. of friction jute-jute [40]
$\delta_{jute-backfill}$	29.0°	Friction angle jute-backfill [7]
σ_{jute}	22.5 kPa	Tensile strength of jute [19]

Table 8.1: Deterministic values for all parameters used in the stability analysis.

Some of the deterministic parameters in table 8.1 have uncertain values. For these parameters, a value distribution needs to be constructed. This is done using information about the range of possible values. For all considered parameters, the reasoning behind the value distribution is explained below.

For the geological parameters, the standard deviation can be derived from the coefficient of variation in the following manner [24]:

$$\sigma = v * mean \quad (36)$$

Where σ is the standard deviation and v is the coefficient of variation. The coefficient of variation provides a relative assessment of how much a variable spreads out or varies in relation to its mean.[24] The coefficient of variation for a certain parameter is often presented in tables with geological properties. The mean values that are listed in table 8.1 are used to find the standard deviation of the geological parameters used. Table 8.2 shows the standard deviations of the geological parameters using equation 36:

Soil parameter	v	Mean	σ
ϕ_{soil}	0.10	30.0°	3.000
c_{soil}	0.20	1.00 kPa	0.200
γ_{soil}	0.05	17.0 kPa	0.850

Table 8.2: Standard deviation of soil parameters using their coefficient of variation. [2]

Note that for the cohesion a truncated distribution is used. This means that the distribution follows the standard deviation, but it is bounded to the minimum value of 0.0 kPa and maximum value of 1.0 kPa. This decision is made because it needs to be prevented that a negative cohesion value can occur, hence the minimum value, and because it is very unlikely that the backfill sand will have a cohesion higher than 1.0 kPa, hence the maximum value.

Also, the sandbag wall is considered to consist out of the same material as the backfill. For this reason, the mean and standard deviation of the unit weight of the soil γ_{soil} will also be applied to the unit weight variable of the sandbag wall γ_{wall} .

The rest of the parameters have a known range, with a considered uncertainty of 95.4%. This means that there is a 4.6% chance that the real value falls outside of the stated range. The standard deviation of these parameters can therefore be determined using equation 28, where the Z-score equals to 2, corresponding to a probability of 95.4%, which is associated with two standard deviations from the mean.

The coefficient of friction of the jute-concrete surface has been determined in the experiment described in chapter 7. A range of values of 0.577-0.675 resulted from this experiment, with a considered mean at 0.620. Using equation 28 grants a standard deviation of 0.025.

The coefficient of friction of a jute-jute interface can be found in literature, and has a value between 0.45 and 0.54. [40] Based on this range and equation 28, a variable mean is chosen of 0.50 with a standard deviation of 0.023.

The value for $\delta_{jute-backfill}$ represents the friction between the sandbag wall and the backfill. The higher this friction angle is, indicating a rougher wall material, the lower the backfill pressure will be on the sandbag wall. [7] This friction angle can only be equal to the internal friction angle of the backfill soil, or lower than that. According to Banne et al. (2021), the friction angle $\delta_{jute-backfill}$ equals to 29° for an interface between a jute wall and a non-cohesive sand backfill with an internal friction angle of 31°. [7] Since the backfill that is considered in the literature is very similar to the top layer of sand in Amsterdam, which has a friction angle of 30° and a low to non-cohesive character, a mean $\delta_{jute-backfill}$ of 29° will be used for the probabilistic analysis. Since $\delta_{jute-backfill}$ can ultimately be as high as the internal friction angle, its maximum is 30°, and its lowest possible value is considered to be equal to that of geo-textile, which is 27°. [7]. To determine the standard deviation, a range of 27°-31° is considered in order to create a symmetrical distribution

around the mean. when applying equation 28, this results into a standard deviation of 1.000. Because this parameter has an absolute maximum, a truncated distribution should be used in the analysis to limit the distribution to a 29° maximum. However, because it cannot be possible for $\delta_{jute-backfill}$ to be higher than the friction angle, it is decided to state that the distribution of $\delta_{jute-backfill}$ equals that of the friction angle, minus 1.0. For a realization where the friction angle equals 26, $\delta_{jute-backfill}$ would equal 25.

According to Ghosh et al., the maximum tensile strength of jute varies with the type of fabric characteristics and how it is woven. [19] They state that for typical woven jute geotextile, the tensile strength varies from 20 kPa to 25 kPa. For this thesis, the tensile strength is considered to have a mean at 22.5 kpa, ranging from 20-25 kpa. The standard deviation is calculated using equation 28, resulting into a value of 1.250.

The parameters that describe the dimensions and tilt of the sandbag wall, and the slope of the backfill are considered to be sufficiently certain. These variables therefore remain deterministic. All parameters are again listed in table 8.3, both deterministic and probabilistic, with their respective means and standards deviations:

Parameter	Mean	σ	Min	Max	Description
ϕ_{soil}	30.0°	3.000	-	-	Friction angle of soil
c_{soil}	1.00 kPa	0.200	0.00 kPa	1.00 kPa	Cohesion of soil
γ_{soil}	17.0 kPa	0.850	-	-	Unit weight of soil
γ_{wall}	17.0 kPa	0.850	-	-	Unit weight of wall
H_{wall}	2.10 m	-	-	-	Height of wall
B_{wall}	0.66 m	-	-	-	Width of wall
α	90.0°	-	-	-	Tilt of wall
β	0.00°	-	-	-	Slope of backfill surface
$\mu_{jute-concrete}$	0.62	0.025	-	-	Coeff. of friction jute-concrete
$\mu_{jute-jute}$	0.50	0.023	-	-	Coeff. of friction jute-jute
δ	29.0°	1.000	-	30.0°	Friction angle jute-backfill
σ_{jute}	22.5 kPa	1.250	-	-	Tensile strength of jute

Table 8.3: Probabilistic parameters used for stability analysis.

8.2.1 Parameter correlations

From chapter 6.4 of this thesis, it was discussed that correlations can be used to create a relationship between certain parameters when realizations are calculated. This means that for realizations with high value samples of parameter A, the samples of parameter B tend to be high as well for a positive correlation. The opposite is true for a negative correlation.

For the geobag wall, correlations can be considered between parameters in order to approach realism. The model is constructed in such a manner that every interface along the wall height have their own versions of all parameters. This means that when realizations are made, the friction angle at the bottom of the wall can have a different value than the friction angle at the second interface from the floor. This is done to include uncertainties about the heterogeneity of the soil parameters and also for uncertainties about the consistency of the tensile strength of jute and the friction coefficients.

While all these difference sample values at every interface come from the same parameter distribution, it is unrealistic that the spatial variability is very high. By using correlations, it is for example possible to make the probability that a high friction angle occurs at the second interface higher, when the friction angle at the first interface is high as well. By doing so, a more gradual spatial variability is implemented along the wall height. In figure 8.5 below, the distribution of correlations are illustrated, where geological parameters and structural parameters follow different distributions.

As is presented in figure 8.5, for geological parameters, i.e. the friction angle, the cohesion and the unit weight of the soil, a correlation coefficient is chosen of 0.5 between wall segments that border each other. One segment further gives a 0.3 correlation, and one further gives a 0.1 correlation. The segments even further located in the wall are considered to have no correlation with the original segment. Note however, that segments on either side of the wall ends are still indirectly correlated, since they both have correlations to the middle segments of the wall, though these correlations shall be fairly weak. For structural parameters, i.e. the unit weight of the wall, the friction coefficients and the tensile strength of the jute, a consistent correlation coefficient of 0.5 is chosen. This decision is made because the same materials are used throughout the wall, and therefore a spatial variability is considered to be small.

In figure 8.6 below, an example is given for the sample values for 10,000 realizations of the friction angle, showing that for high sample values at the first interface, the sample values on the second interface tend to become higher as well.

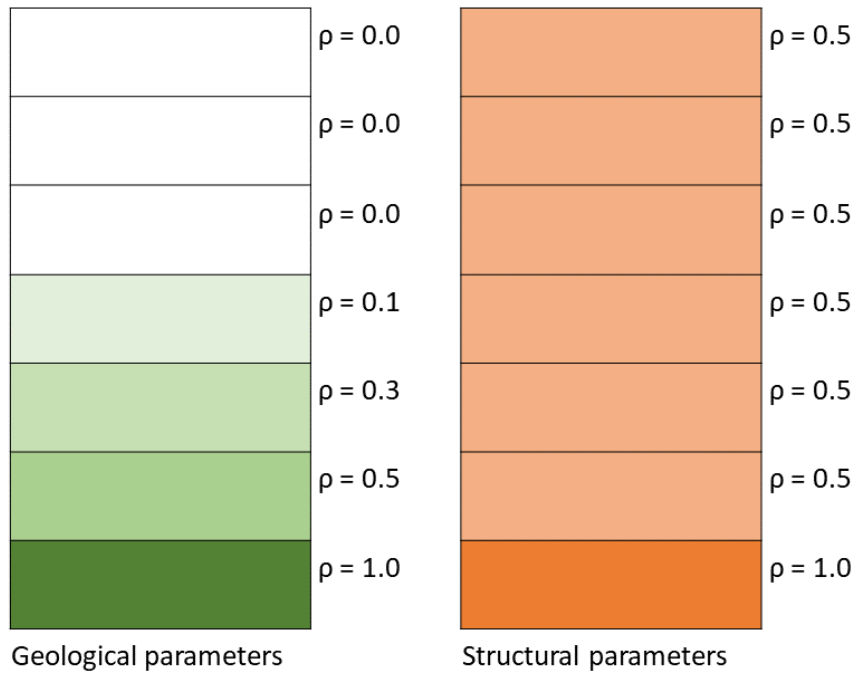


Figure 8.5: An example of the correlation distribution with respect to the bottom segment for both the geological and structural parameters.

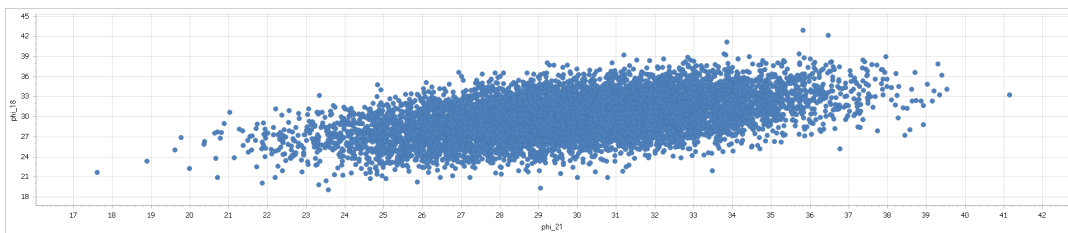


Figure 8.6: An example of the correlation between the friction angles on the first and second interface.

8.3 Analyses to be performed

To determine the reliability of Koningsgracht, and to determine the most parameters with the largest impact on this reliability, several analyses are performed, listed below. It is also listed what probabilistic method is used for each analysis.

1. Global reliability (Monte Carlo)

The reliability of the global structure is represented by the probability of failure along the bottom interface of the wall, between the jute geobags and the concrete floor. The FOS distributions will be presented and the probability of failure is listed considering failure for $FOS = 1.0$ and for $FOS = 2.0$ to incorporate model uncertainties. Monte Carlo is used for this analysis, using 25000 realizations and all parameter correlations as stated in this chapter.

2. Local reliability (Monte Carlo)

To assess the local failure of the geobag wall, the FOS distributions are calculated for all failure interfaces, which occur every 0.3 meters along the wall height. The FOS distributions will be presented and the probability of failure is again listed considering failure for $FOS = 1.0$ and for $FOS = 2.0$. Monte Carlo is used for this analysis, using 25000 realizations and all parameter correlations as stated in this chapter.

3. Contribution analysis (Monte Carlo)

Using the reliability method from the Probabilistic Toolkit, the contributions of each parameter to the limit state can be assessed. This contribution analysis is performed for the bottom interface, representing global failure, for all three failure modes. For this analysis, failure is assumed at $FOS = 2.0$. Monte Carlo is used for this analysis, using 25000 realizations and all parameter correlations as stated in this chapter.

4. Sensitivity analysis to parameters (FOSM)

The sensitivity analysis is performed using the in-built sensitivity method in the Probabilistic Toolkit, and by performing the analysis manually. For the in-built toolkit method, a lower 5% and upper 95% boundary value is automatically calculated from the mean and standard deviation of every uncertain input parameter. Then, for every parameter, three realizations are calculated for each of these value variations. With all other parameters set on the mean value, a deterministic calculation is performed. The manual sensitivity analysis is done using the FOSM method, where the toolkit predicts the FOS distribution based on the input distributions, without making realizations. A lower and upper boundary is calculated manually as well. FOSM is chosen for it requires significantly less computational power, and is therefore very efficient. As an additional reason, the impact of parameter changes on the FOS calculation is desired for a sensitivity analysis, and that impact can be retrieved as accurately using FOSM, as when using Monte Carlo.

5. Sensitivity to scenarios (FOSM)

Another sensitivity analysis is performed using FOSM, but now for additional scenarios that could occur and potentially alter the geobag wall's stability. The scenarios that will be assessed are discussed in subsection 8.4

6. Results system reliability

Finally, the system reliability is assessed considering the failure modes and wall interfaces to be either dependent or independent from one another. The impact of the dependency on the system reliability is then discussed.

The results of these analyses are presented in chapter 9.

8.4 Scenarios for the sensitivity analysis

In this chapter, the four scenarios that are considered for a sensitivity analysis are presented.

One of the critical scenarios to examine is the change in wall tilt, which plays a significant role in the integrity of the geobag wall. Wall tilt refers to the angle at which the geobag wall leans or inclines from its vertical position. When the wall tilt of a geobag wall is altered, it has a notable effect on the normal force acting on the wall. The normal force is the force exerted perpendicular to the wall's surface and is primarily responsible for maintaining the wall's stability. When the wall tilts away from its vertical position, the normal force on the wall decreases and a new gravity term comes into effect, exerting a force parallel to the surface that can contribute to the wall's instability and potential failure. The original tilt of the wall (90°) is changed to 85° and 80° to see how it affects the wall's stability.

The second scenario to analyze is the change in surcharge on the surface above the backfill. This surcharge can occur for various reasons, such as heavy traffic loads, construction equipment, or any additional weight placed on the ground adjacent to the wall. The original scenario has no surcharge, and the change in failure probability will be assessed for a surcharge of 5 kPa and 10 kPa.

The last two scenarios that are considered have an increased wall height and an increased wall width. The original wall height is 2.1 meters, and the tallest possible quay wall retaining height is 3.6 meters. Therefore, a middle value of 2.9 meters and the maximum of 3.6 meters will be utilized for the scenarios. The original wall width equals to 1.0 meters. A smaller 0.66 meters and a larger 1.66 meter wall width are used to see their impact on the stability. For the 0.66 meter width, one geobag is considered to equal the wall width, for the original situation, two geobag widths are considered to equal the wall width, and for the 1.66 meter width scenario, it is considered that the wall is three geobags wide. This is important for it determines how the tensile stresses are divided in order to determine the probability of rupture.

9 Results and interpretation

In this chapter, the results of the proposed analysis methods from 8 are presented. In the first subsection, the FOS distributions and the reliability of the global wall structure is presented for all failure modes, i.e. horizontal sliding, overturning, and geobag rupture. This is followed by the FOS distributions of all local interfaces of the geobag wall, together with the reliability per interface. In the second subsection, the contribution of each involved parameter is assessed using the in-built reliability function of the Probabilistic Toolkit. Then, the results of the sensitivity analysis are discussed. This includes the assessment of the sensitivity to the scenario's introduced in chapter 8. Finally, the global reliability is again assessed, considering dependent failure modes, and compared to the reliability results when independent failure modes are considered.

9.1 Global and local reliability analysis

Using the parameters outlined in chapter 8, a probabilistic analysis is conducted to determine the distributions of the factor of safety for the three distinct failure modes. This is done by running a Monte Carlo simulation, using 25,000 realizations.

9.1.1 Global reliability

The FOS for the global structure is represented by failure along the bottom interface of the wall, between the jute geobags and the concrete floor. In table 9.1 below, the normal distributions of the FOS values from the Monte Carlo simulation for all three modes are presented for the global structure, along with the probability of failure P_f for a limit state of $FOS = 1$. The failure probabilities for $FOS = 2$ are also listed, but one should note that this limit state is very conservative. It can be used to incorporate model uncertainties, but a limit twice as high as $FOS = 1$ is most probably unrealistic, and should solely be used to get a better understanding of which mode is most likely to occur.

The distributions are listed by their mean μ and their standard deviation σ , and the probability of failure is accompanied by the reliability index β to enhance the understanding of the margin of safety. This table is followed by figures 9.1 and 9.2, where the FOS distributions for all modes are visually presented by their PDF and CDF.

Mode	Distribution	μ	σ	$FOS = 1$		$FOS = 2$	
				β	P_f	β	P_f
Hor. slid.	Normal	2.411	0.3625	3.892	$4.973 \cdot 10^{-5}$	1.134	$1.284 \cdot 10^{-1}$
Overturn.	Normal	2.778	0.4016	4.427	$4.782 \cdot 10^{-6}$	1.937	$2.637 \cdot 10^{-2}$
Rupture	Normal	2.184	0.1596	7.419	$5.947 \cdot 10^{-14}$	1.153	$1.245 \cdot 10^{-1}$

Table 9.1: Results probabilistic analysis of geobag wall failure mechanisms.

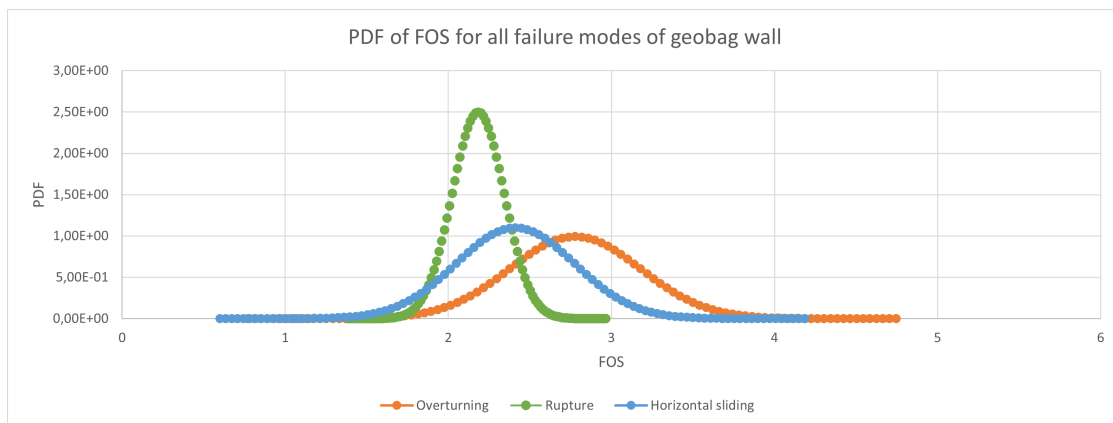


Figure 9.1: The PDF's of the FOS distribution for all failure mechanisms.

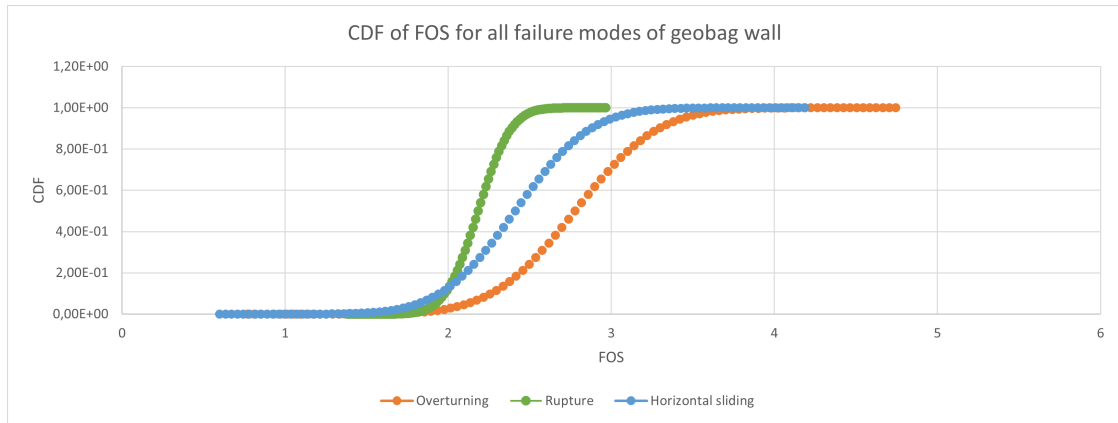


Figure 9.2: The CDF's of the FOS distribution for all failure mechanisms.

Based on the input parameters utilized, it becomes apparent that all failure modes show a Factor of Safety (FOS) distribution with a large margin to the limit state of $FOS = 1$. To understand the magnitudes of safety, one can look at the reliability index β , showing that the means of all modes are almost at a distance of at least four standard deviations from a limit state of $FOS = 1$. Using the thumb rule of probabilities, one knows that 99.7% of all values in a distribution occur within a distance of three standard deviations. This means that when the reliability index is at least 3, one can already assume that failure is not likely to occur.

Note that β is larger for the textile rupture distribution per distance to the limit state than for the other mode distributions because the standard deviation of textile rupture is significantly smaller. This means that for the same value of β for all modes, the probability of failure is higher for textile rupture than for the other modes.

When analyzing the failure probabilities for a limit state of $FOS = 2$, one can see that probabilities of failure increased significantly. While the probabilities that horizontal sliding or textile rupture occurs became more similar to one another, the probability of overturning is a tenth smaller for this limit state.

9.1.2 Local reliability

To assess the local failure of the geobag wall, the FOS distributions are generated for all failure interfaces, which occur every 0.3 meters along the wall height. Note that at an interface height of 0.0 meters, at the bottom of the wall, the same assessment is done as for the global structure, hence those results are the same as in table 9.1. For the local failure assessment, the means and standard deviations of the FOS distributions are presented per geobag wall interface. From these distributions, the probability of failure P_f can be listed based on a limit state of $FOS = 1$ and $FOS = 2$. The probability of failure is accompanied by the reliability index β , for a better understanding of the magnitude of safety for low probabilities. These results are all listed in table 9.2 below.

$H_{interface}$	Mode	μ	σ	$FOS = 1$		$FOS = 2$	
				β	P_f	β	P_f
1.8 m	Hor. slid.	92.58	73.55	1.245	$1.066 \cdot 10^{-1}$	1.232	$1.090 \cdot 10^{-1}$
	Overturn.	925.3	734.1	1.259	$1.040 \cdot 10^{-1}$	1.258	$1.042 \cdot 10^{-1}$
	Rupture	8.448	0.783	9.512	$9.513 \cdot 10^{-22}$	8.235	$9.079 \cdot 10^{-17}$
1.5 m	Hor. slid.	11.92	2.764	3.951	$3.893 \cdot 10^{-5}$	3.589	$1.660 \cdot 10^{-4}$
	Overturn	59.58	13.53	4.330	$7.461 \cdot 10^{-6}$	4.256	$1.041 \cdot 10^{-5}$
	Rupture	5.712	0.4594	10.26	$5.448 \cdot 10^{-25}$	8.080	$3.273 \cdot 10^{-16}$
1.2 m	Hor. slid.	5.995	1.116	4.476	$3.806 \cdot 10^{-6}$	3.580	$1.718 \cdot 10^{-14}$
	Overturn	19.98	3.596	5.278	$6.543 \cdot 10^{-8}$	5.000	$2.871 \cdot 10^{-7}$
	Rupture	4.320	0.3287	10.10	$2.818 \cdot 10^{-24}$	7.058	$8.502 \cdot 10^{-13}$
0.9 m	Hor. slid.	3.958	0.6661	4.441	$4.481 \cdot 10^{-6}$	2.939	$1.646 \cdot 10^{-3}$
	Overturn	9.900	1.603	5.552	$1.416 \cdot 10^{-8}$	4.928	$4.160 \cdot 10^{-7}$
	Rupture	3.4684	0.2576	9.582	$4.843 \cdot 10^{-22}$	5.700	$6.008 \cdot 10^{-9}$
0.6 m	Hor. slid.	2.945	0.4741	4.103	$2.040 \cdot 10^{-5}$	1.993	$2.313 \cdot 10^{-2}$
	Overturn	5.890	0.910	5.374	$3.859 \cdot 10^{-8}$	4.275	$9.563 \cdot 10^{-6}$
	Rupture	2.900	0.2134	8.903	$2.757 \cdot 10^{-19}$	4.217	$1.239 \cdot 10^{-5}$
0.3 m	Hor. slid.	2.342	0.3589	3.739	$9.240 \cdot 10^{-5}$	0.953	$1.703 \cdot 10^{-1}$
	Overturn	3.905	0.5701	5.096	$1.738 \cdot 10^{-7}$	3.342	$4.159 \cdot 10^{-4}$
	Rupture	2.491	0.1821	8.188	$1.343 \cdot 10^{-16}$	2.696	$3.509 \cdot 10^{-3}$
0.0 m	Hor. slid.	2.411	0.3625	3.892	$4.973 \cdot 10^{-5}$	1.134	$1.284 \cdot 10^{-1}$
	Overturn	2.778	0.4016	4.427	$4.782 \cdot 10^{-6}$	1.937	$2.637 \cdot 10^{-2}$
	Rupture	2.184	0.1596	7.419	$5.947 \cdot 10^{-14}$	1.153	$1.245 \cdot 10^{-1}$

Table 9.2: All FOS distributions and failure probabilities per mode for every local interface along the geobag wall.

From table 9.2 the failure probabilities can easily be compared between all modes at every interface along the wall. Note that the FOS distributions at the bottom interface, at $H_{interface} = 0.0m$, equal those of the global structure which were discussed before. For a limit state of $FOS = 1$, the probability of failure is very small along all interfaces for all three modes. When analyzing the values of reliability index β , one could see that there is a sufficient safety margin, since these values approach a value of 4 or higher.

With an increase in interface height, the value of β increases at the bottom half of the wall, indicating larger safety margins and therefore smaller failure probabilities. However, when analyzing the interfaces at the upper half of the wall, one can see that the value of β decreases again, while the conditions are expected to be safer at the top of the wall, since the loads and forces decrease in height. The phenomena of β decreasing at the upper half of the wall can be explained by a consistent increase of the standard deviation with the wall height. The higher the interface is situated, the more uncertain the FOS distribution is, hence the probability that values occur beyond the limit state eventually increases as well.

The reason that the uncertainty increases with height, is because the deterministic parameters decrease in the limit state equation, while the uncertain parameters keep their distribution. Therefore, the contribution of the deterministic parameters relatively decrease to the value of the FOS compared to the contribution of the uncertain parameters, resulting into an increase in uncertainty for the limit state equation.

One discrepancy in these results is the probability of horizontal sliding at the second interface from the bottom, at $H_{interface} = 0.3$. The probability of failure of this mode is larger here than at the bottom interface, while the probability of failure generally decreases over height. The reason for this is because the second interface hosts a smoother jute-jute contact, while the bottom interface hosts a rougher jute-concrete contact.

For $FOS = 1$, one can conclude that textile rupture is the least likely to occur along all interfaces. This is followed by overturning, with its highest probabilities at the bottom of the wall. Horizontal sliding can be seen as the relatively most likely mode to occur along the entire wall. The top two interfaces include too much uncertainty to add anything to this conclusion, considering these interfaces belong to the more safe interfaces.

For $FOS = 2$, a similar ratio between the probabilities of horizontal sliding and overturning can be seen, where horizontal sliding is consistently more likely to occur. However, textile rupture has risen in probability of failure significantly for $FOS = 2$. The reason for this change, compared to the other two modes, is because of the relatively small standard deviation of textile rupture. When moving the limit state, this means that relatively many realizations of textile rupture exceed its border.

From these findings, the primary research question can be conclusively addressed, i.e the reliability of the geobag wall system. This will be addressed in chapter 9.5 of this thesis.

9.2 Contribution analysis

The Probabilistic Toolbox provides a reliability analysis which states the contributions of each parameter, positive or negative, to the FOS calculation. This contribution analysis is performed at the bottom interface, representing global failure, for all three failure modes. Failure is assumed at $FOS = 2$ or lower, because a limit state at $FOS = 1$ calculates probabilities that are too low for this contribution analysis. If one would still use $FOS = 1$, the contributions of all parameters would result into an equal value, which is false.

The results from the reliability analysis are presented in table 9.3.

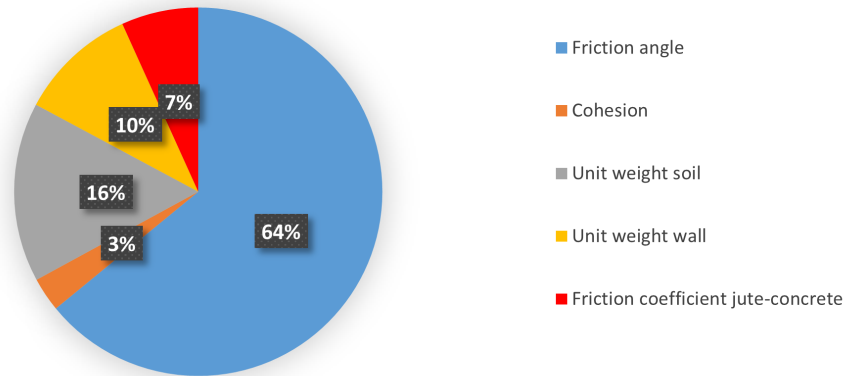
Parameter	Hor. sliding		Overturning		Rupture	
	α	infl. factor	α	infl. factor	α	infl. factor
ϕ_{soil}	0.789	0.622	0.829	0.688	0.235	0.0554
c_{soil}	0.171	0.0291	0.186	0.0346	0.0321	0.0010
γ_{soil}	-0.391	0.153	-0.353	0.125	-0.162	0.0264
γ_{wall}	0.318	0.101	0.332	0.110	-0.534	0.286
$\mu_{jute-concrete}$	0.256	0.0657	-	-	-	-
σ_{jute}	-	-	-	-	0.772	0.597

Table 9.3: Results of the reliability analysis, stating the impact of all parameters per failure mode.

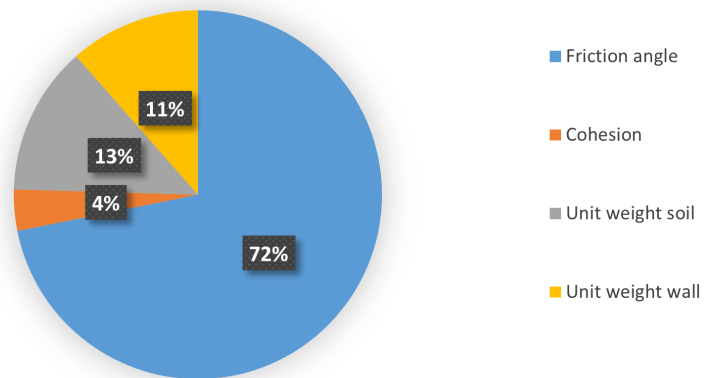
Where α represents the contribution per parameter to the reliability. It gives a more detailed and comprehensive understanding of how individual factors or components contribute to the overall reliability or safety of a system. Parameters with negative α values indicate areas of concern where the system is more prone to failure or non-compliance with performance requirements. On the other hand, parameters with positive α values shows strengths in the system. These parameters contribute positively to the overall reliability, and efforts can be directed toward maintaining or enhancing these aspects.

From the contribution factor α , the influence factor can be calculated for each parameter, since the influence factor equals to α^2 . The influence factor marks the impact a parameter has on the FOS calculation, where the sum of the influence factors of all parameters equals to 1. The influence of each parameter to the FOS calculation of the failure modes can also be visualized in pie charts, presented in figure 9.3.

Parameter contributions - Horizontal sliding



Parameter contributions - Overturning



Parameter contributions - Textile rupture

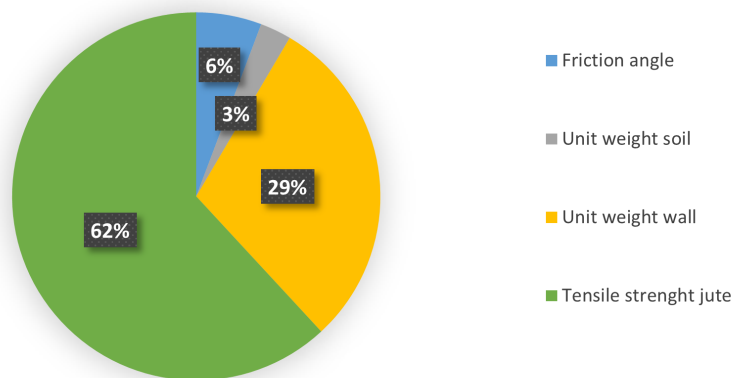


Figure 9.3: Parameter contributions of all failure modes.

Notably from table 9.3 and figure 9.3, the friction angle emerges as a critical factor significantly influencing the FOS in the modes horizontal sliding and overturning. In contrast, the tensile strength of the jute material is dominant in determining the FOS in the textile rupture failure mode. Additionally for the latter mode, the unit weight of the wall is of more importance to determining the FOS than it is for horizontal sliding and overturning, in contrary to the unit weight of the soil which contributes less to textile rupture. Interestingly, the cohesion of the soil has a negligible impact on the calculation of the FOS of textile rupture. This is probably due to the fact that the earth pressure has a less significant contribution to the limit state calculation of textile rupture, hence cohesion, a parameter determining the magnitude of earth pressure, has a lower contribution.

9.3 Sensitivity analysis

9.3.1 Toolbox sensitivity analysis

The Probabilistic Toolbox can construct bar plots for every input parameter, showing their impact on the value of the FOS of any failure mode. To do this it calculates a lower and upper boundary value for each parameter from their mean and standard deviation. For the toolbox sensitivity analysis, the lower boundary is set at the 5% value in the distribution, and the upper boundary is set at the upper 95% value for each parameter. In figure 9.4, the bar plots are presented for all failure modes.

From the bar plots of figure 9.4, one can see that the friction angle has a large influence on the FOS of both horizontal sliding and overturning. As could be seen in the contributions pie charts of figure 9.3, the friction angle only has a limited effect on the FOS of textile rupture, similarly to the other soil parameters for the contribution of the soil pressure is lower for this failure mode. The unit weight of the soil is the only parameter for horizontal sliding and overturning that affects the FOS of all modes in a negative manner. This is because for higher values of unit weight of the soil, the soil becomes heavier hence it will exert larger pressures onto the wall. For textile rupture, the unit weight of the wall acts as a driving force of failure as well, since rupture also occurs when the tensions from the weight of the wall increase.

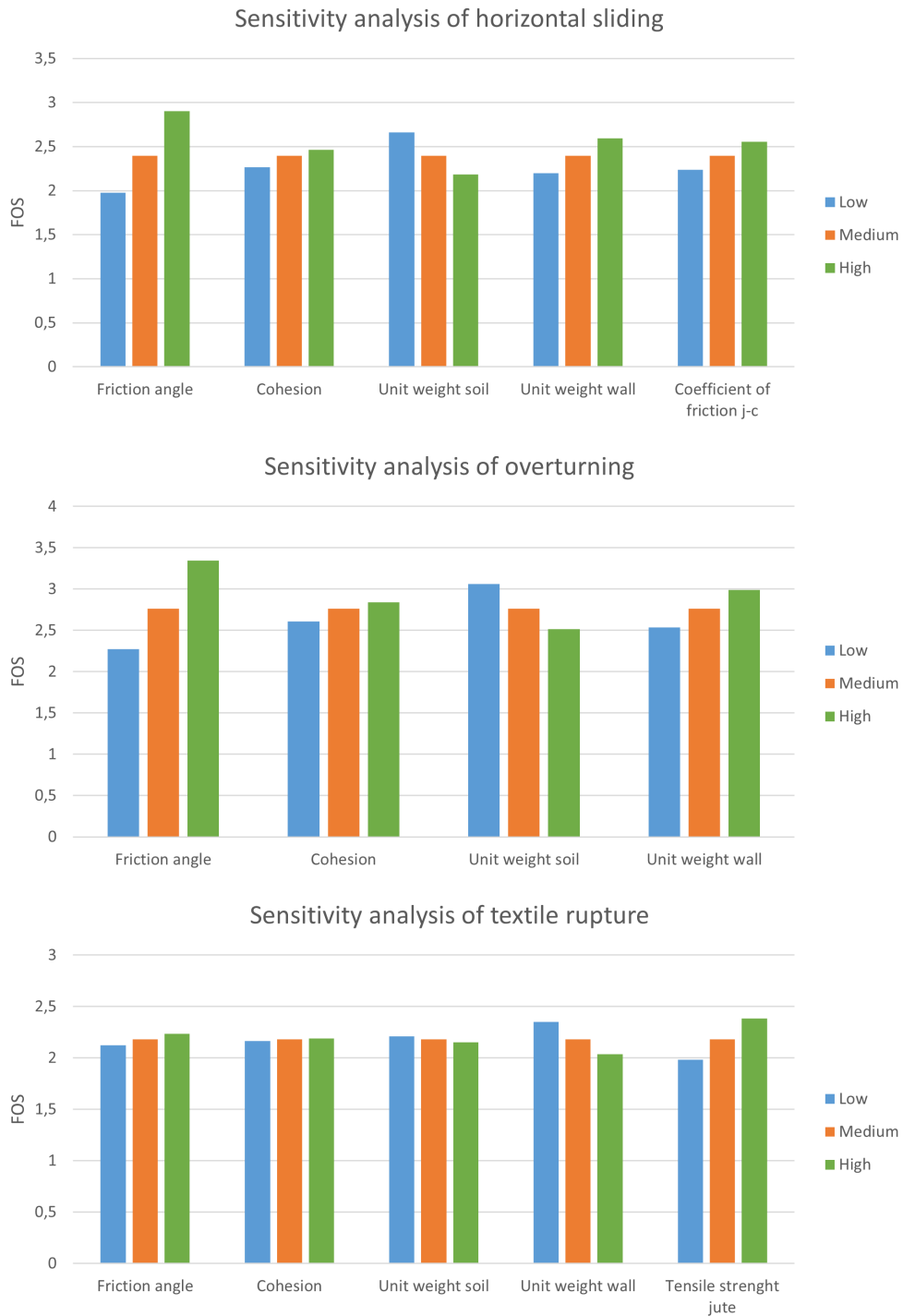


Figure 9.4: The FOS sensitivity to all parameters for all modes.

9.3.2 Manual sensitivity analysis

In this chapter, a reliability analysis is performed while changing the parameter value to its lower, mean, or upper boundary value. The pie charts and bar plots in the previous chapter are constructed using the means and standard deviations of the parameter distributions, where a lower and upper boundary value was automatically calculated, using the 5% and 95% value. For the manual sensitivity analysis, to toolbox is used to calculate the FOS distributions with the FOSM method, using a lower 2.3% and upper 97.7% boundary value for each parameter. The FOSM method is a predictive method of the FOS distributions without performing actual sample calculations. However, for a sensitivity analysis it is an excellent method. These percentiles are chosen because these are exactly on a two-standard-deviation-distance from the mean. The lower, mean and upper bound values that are used in the sensitivity analysis are presented in table 9.4 below.

Parameter	Unit	Lower 2.3%	Mean	Upper 97.7%
ϕ_{soil}	°	24	30	36
c_{soil}	<i>kPa</i>	0.6	1.0	1.4
γ_{soil}	<i>kPa</i>	15.3	17	18.7
γ_{wall}	<i>kPa</i>	15.3	17	18.7
$\mu_{jute-concrete}$	—	0.57	0.62	0.67
$\mu_{jute-jute}$	—	0.454	0.50	0.546
$\delta_{jute-soil}$	°	27	29	31
σ_{jute}	<i>kPa</i>	20	22.5	25

Table 9.4: Lower, mean and upper boundary values for all uncertain parameters, used for the sensitivity analysis.

The sensitivity analysis creates three FOS distributions per parameter, per failure mode. Two examples of the PDF distributions of horizontal sliding for a changing friction angle and changing friction coefficient is shown below in figure 9.5. The parameter that is being assessed is set to be deterministic, and the model is run three times to test its effect on the FOS distribution. The parameters that are not being assessed remain uncertain with a normal distribution. This sensitivity results in tables 9.5 to 9.7, for the bottom interface, i.e. the global construction. For every parameter value, for all three modes, the probability of failure is listed. This is done for failure at $FOS = 1.0$, and for failure at $FOS = 2.0$. Note that because of a negligible contribution of $\delta_{jute-backfill}$ to the FOS calculation it is decided not to include it in the sensitivity analysis. It is later discussed why this effect is so little.

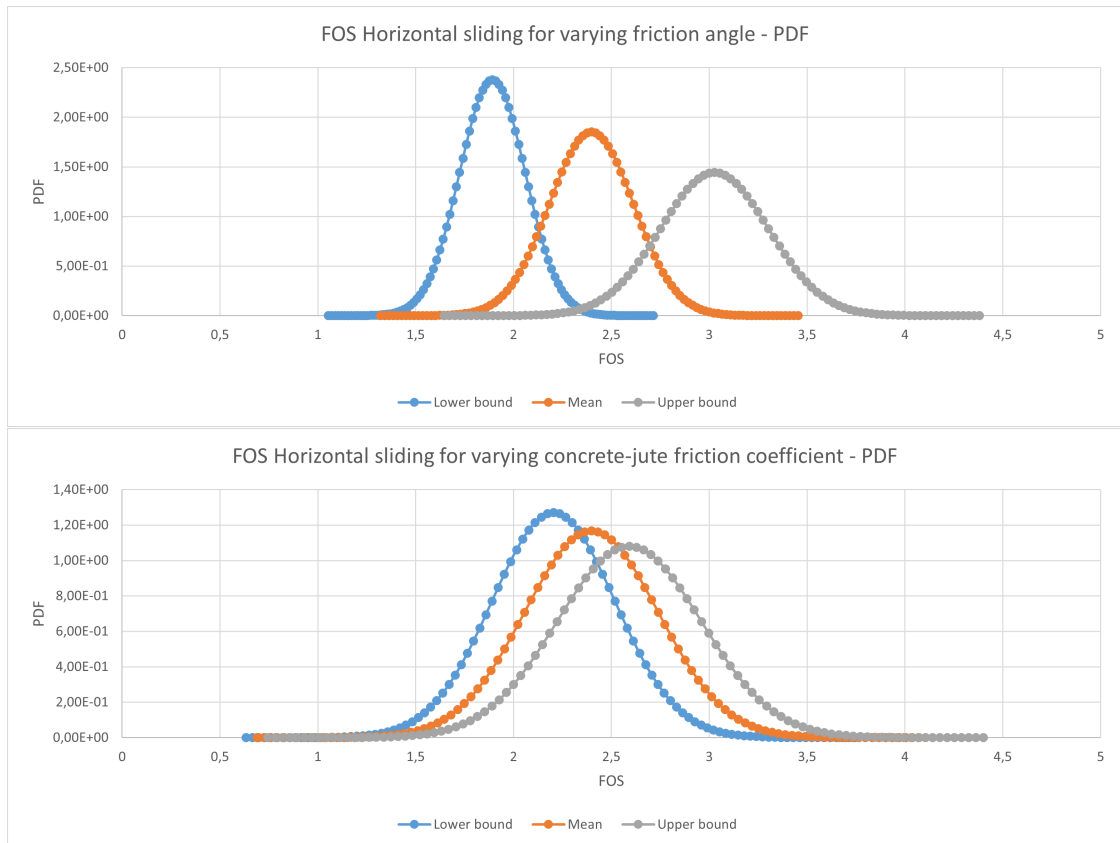


Figure 9.5: PDF curves of the FOS of horizontal sliding for a changing friction angle and changing jute-concrete friction coefficient.

Hor slid.	$P(F = 1.0)$ [%]			$P(F = 2.0)$ [%]		
Parameter	Low	Mean	High	Low	Mean	High
ϕ_{soil}	0	0	0	42	0.50	0
c_{soil}	0	0	0	9.7	4.7	2.0
γ_{soil}	0	0	0	1.07	4.46	15.9
γ_{wall}	0	0	0	15.9	5.45	1.79
$\mu_{jute-concrete}$	0	0	0	27.0	13.4	5.48

Table 9.5: Reliability of the global geobag wall against horizontal sliding per changing parameter.

Overturning	$P(F = 1.0)$ [%]			$P(F = 2.0)$ [%]		
Parameter	Low	Mean	High	Low	Mean	High
ϕ_{soil}	0	0	0	15.9	0.03	0
c_{soil}	0	0	0	4.5	1.97	0.82
γ_{soil}	0	0	0	0.30	1.79	6.70
γ_{wall}	0	0	0	7.00	2.00	0.50

Table 9.6: Reliability of the global geobag wall against overturning per changing parameter.

Rupture	$P(F = 1.0)$ [%]			$P(F = 2.0)$ [%]		
Parameter	Low	Mean	High	Low	Mean	High
ϕ_{soil}	0	0	0	24.1	12	6.68
c_{soil}	0	0	0	15.9	11.5	9.68
γ_{soil}	0	0	0	9.50	13.6	18.4
γ_{wall}	0	0	0	0.35	8.08	50.0
σ_{jute}	0	0	0	75.8	3.59	0

Table 9.7: Reliability of the global geobag wall against textile rupture per changing parameter.

As was could be seen in 9.2, there is a 0% probability that failure occurs for $FOS = 1.0$. However, for failure that is considered to occur at $FOS = 2.0$ this changes significantly.

A change in the friction angle has a substantial effect on the likelihood of horizontal sliding occurring. In comparison, the cohesion and unit weight of the soil exert less influence. Conversely, the unit weight of the wall and the friction coefficient of the jute-concrete contact make a significant contribution. The reason behind the substantial impact of the friction angle is its relatively wide distribution, where the lower boundary value is significantly lower than its mean. This is in contrast to the distribution of cohesion or friction coefficient, both of which have relatively narrower distributions.

When it comes to overturning, it can be observed that the impact of each parameter on the probability of failure resembles that of horizontal sliding. It's essential to take into account the percentage change in probability rather than solely examining changes in values.

Finally, when considering the textile rupture mode, it becomes evident that the tensile strength has a significantly high impact on the probability of failure. Furthermore, it's evident that geological parameters have minimal influence on the rupture of the geobags, while the unit weight of the wall plays a substantially more significant role.

9.4 Sensitivity to scenarios

In the following subsections, the effect of applying the scenarios that were presented in chapter 8.4 to the wall's stability will be assessed compared to the original situation.

In table 9.8 below, the four parameters that represent the scenarios are listed. The original value of these parameters is shown, together with the value of the 8 additional scenarios, i.e. the original situation plus two scenarios per parameter. For example, in scenario 2a, the surcharge is changed from 0 kPa to 5.0 kPa. All other parameters keep their original value. At scenario 4b, the wall width is set to 1.66 m, while all other parameters again keep their original value. Note that all parameter changes per scenario will be changed in the model separately. This means that a reliability is calculated per one parameter change.

Scenario	Parameter	Original	a	b
1	Wall tilt α	90°	85°	80°
2	Surcharge q	0 kPa	5.0 kPa	10 kPa
3	Wall height H	2.1 m	2.9 m	3.6 m
4	Wall width B	1.0 m	0.66 m	1.66 m

Table 9.8: Parameter values for the original situation, and for the additional 8 scenario's.

The reliability of the global structure is assessed at limit state $FOS = 1.0$ and $FOS = 2.0$. This reliability analysis is done using the FOSM method. For simplicity, values approaching zero are listed as such. The results are presented in tables 9.9 to 9.11.

Scenario	Parameter	$P(F = 1.0)$ [%]			$P(F = 2.0)$ [%]		
		Original	a	b	Original	a	b
1	Wall tilt α	0.00	0.02	4.46	12.7	98.9	100
2	Surcharge q	0.00	0.10	1.20	12.7	80.0	99.8
3	Wall height H	0.00	0.35	5.50	12.7	93.3	100
4	Wall width B	0.00	0.62	0.00	12.7	96.4	0.03

Table 9.9: Global reliability against horizontal sliding for the original situation and for the additional 8 scenarios.

Scenario	Parameter	$P(F = 1.0)$ [%]			$P(F = 2.0)$ [%]		
		Original	a	b	Original	a	b
1	Wall tilt α	0.00	0.00	1.79	1.39	98.9	100
2	Surcharge q	0.00	0.03	1.79	1.39	75.8	100
3	Wall height H	0.00	2.87	88.5	1.39	100	100
4	Wall width B	0.00	12.0	0.00	1.39	100	0.00

Table 9.10: Global reliability against overturning for the original situation and for the additional 8 scenarios.

Scenario	Parameter	$P(F = 1.0)$ [%]			$P(F = 2.0)$ [%]		
		Original	a	b	Original	a	b
1	Wall tilt α	0.00	0.00	0.00	13.6	18.4	23.0
2	Surcharge q	0.00	0.00	0.00	13.6	28.0	50.0
3	Wall height H	0.00	0.00	0.00	13.6	100	100
4	Wall width B	0.00	0.00	0.19	13.6	0.00	100

Table 9.11: Global reliability against textile rupture for the original situation and for the additional 8 scenarios.

As the wall tilt angle increases, the $P(F)$ of both horizontal sliding and overturning experiences a rise for both $FOS = 1.0$ and $FOS = 2.0$. When the wall is tilted, the normal weight that helps resisting these failure modes decreases, while the weight gains a horizontal component that drives sliding and overturning. The rupture of geotextile seems to be affected the least by the tilting of the wall, for a redistribution of forces has little effect on this mode. This is because rupture failure is driven by a summation of both the normal force and the earth pressure, hence a redistribution has little effect.

The addition of a surcharge atop the backfill exerts a notable impact on the failure modes, particularly concerning the horizontal sliding and overturning of the geobag wall. However, its influence on the rupture of the geotextile is comparatively less pronounced. The surcharge introduces an extra horizontal pressure to the earth pressure already at play. However, it is important to note that this added pressure doesn't strengthen the resistance of the failure modes.

As the height of the wall is elevated, a noticeable impact is primarily observed in the context of the overturning mode. This is due to the fact that the driving moment arm becomes larger, while the backfill pressure increases over a larger length as well. Geo textile rupture is said to occur as well considering failure at $FOS = 2.0$. This development can be attributed to the increased weight of the wall and the accompanying pressure, resulting in substantial tensile stresses within the jute bags.

Finally, with a decreasing width the geobag wall becomes significantly more prone to overturning. The reduction in weight and the diminishment of the resisting moment arm are responsible for this outcome. Additionally, the likelihood of horizontal sliding increases due to a decrease in the normal force. Conversely, when the wall width expands, it exhibits complete stability against overturning for the considered FOS values, accompanied by a minimal probability of horizontal sliding. In contrary, for $FOS = 2.0$, geobag rupture becomes an inevitable consequence of the increment of geobag wall weight.

9.5 Results system reliability

In chapter 6 of this thesis, it was discussed that the failure modes of the geobag wall are considered to be in series and fully dependent on one another. The reason for the decision is because the modes are largely dependent on the same parameter set.

Since in reality, a full dependency is unrealistic, it is useful to identify the system reliability by considering both fully dependent as independent modes. The true dependency will most probably lie in between both relationships, hence the true system reliability will as well.

To determine the system reliability, the results of chapter 9.1.2, which were listed in table 9.2, are used. In table 9.12 below, the results from the bottom three interfaces are again shown, since these interfaces have the most significant probability of failure. The results of the other interfaces are considered to be sufficiently small to be neglected in the determination of the system reliability.

$H_{interface}$	Mode	μ	σ	$FOS = 1$		$FOS = 2$	
				β	P_f	β	P_f
0.6 m	Hor. slid.	2.945	0.4741	4.103	$2.040 \cdot 10^{-5}$	1.993	$2.313 \cdot 10^{-2}$
	Overturn	5.890	0.910	5.374	$3.859 \cdot 10^{-8}$	4.275	$9.563 \cdot 10^{-6}$
	Rupture	2.900	0.2134	8.903	$2.757 \cdot 10^{-19}$	4.217	$1.239 \cdot 10^{-5}$
0.3 m	Hor. slid.	2.342	0.3589	3.739	$9.240 \cdot 10^{-5}$	0.953	$1.703 \cdot 10^{-1}$
	Overturn	3.905	0.5701	5.096	$1.738 \cdot 10^{-7}$	3.342	$4.159 \cdot 10^{-4}$
	Rupture	2.491	0.1821	8.188	$1.343 \cdot 10^{-16}$	2.696	$3.509 \cdot 10^{-3}$
0.0 m	Hor. slid.	2.411	0.3625	3.892	$4.973 \cdot 10^{-5}$	1.134	$1.284 \cdot 10^{-1}$
	Overturn	2.778	0.4016	4.427	$4.782 \cdot 10^{-6}$	1.937	$2.637 \cdot 10^{-2}$
	Rupture	2.184	0.1596	7.419	$5.947 \cdot 10^{-14}$	1.153	$1.245 \cdot 10^{-1}$

Table 9.12: All FOS distributions and failure probabilities per mode for every local interface along the geobag wall.

For fully dependent events, the system reliability equals to the maximum reliability between the reliabilities of the system's events. For independent events, the system reliability can be calculated with the following equation, considering three events:

$$P(F) = P(F_1 + F_2 + F_3) - P(F_1 \cdot F_2) - P(F_1 \cdot F_3) - P(F_2 \cdot F_3) + P(F_1 \cdot F_2 \cdot F_3) \quad (37)$$

Note that not only the different modes can either be fully dependent or independent from one another, but this should also be considered for the different wall interfaces, as visualized in the fault tree of figure 5.10. This results into four possible system reliabilities, presented for both the limit states $FOS = 1$ and $FOS = 2$ in table 9.13.

Mode relationship	Interface relationship	$P_f(FOS = 1)$	$P_f(FOS = 2)$
Dependent	Dependent	$9.240 \cdot 10^{-5}$	$1.703 \cdot 10^{-1}$
	Independent	$1.625 \cdot 10^{-4}$	$2.936 \cdot 10^{-1}$
Independent	Dependent	$9.257 \cdot 10^{-5}$	$2.570 \cdot 10^{-1}$
	Independent	$1.675 \cdot 10^{-4}$	$4.002 \cdot 10^{-1}$

Table 9.13: System probability of failure considering modes and interfaces being dependent and independent from one another.

Again, one should note that the limit state of $FOS = 2$ is highly conservative, where failure is assumed when the resisting forces are equal or lower than twice the active forces. The results from the $FOS = 1$ are more realistic, where all relationships consistently result into very low probabilities of failure. The probability of failure for $FOS = 2$ is still presented to assess the effect of a changed limit state.

The probabilities of failure that were presented in table 9.12 result into four possible system probabilities. The safest scenario is when both the modes as the interfaces are considered to be fully dependent on one another, i.e. the modes to other modes and the interfaces to other interfaces. Dependent modes and interfaces result into the lowest system reliability, fully based on the highest probability of failure of one of the modes at one of the interfaces. In this scenario the reliability of other modes and interfaces other than the maximum do not contribute to the system probability. This is because with full dependency, it is considered that when the modes with smaller probabilities occur, the mode with the maximum probability has occurred as well.

The probability of failure increases significantly for the scenarios where either the modes, or the interfaces are independent, or both. The latter means that modes or interfaces are less or not influenced by one another, meaning that individual probabilities of failure combine towards a higher system probability, since failure by multiple modes and along multiple interfaces could occur, and where only occurrence is needed for the failure of the geobag wall system.

The reason that a system with dependent modes and independent interfaces has a higher probability of failure than a system with independent modes and dependent interfaces is because the mode probabilities are the source of all further probabilities in the failure tree. Dependent modes ensure that the maximum probability is picked per interface. Consequently, the independent interfaces combine all these relatively high probabilities resulting in the highest possible system probability. For an independent mode- and dependent interface system, the independent modes could send a relatively low probability of failure to the interface. The highest of these relatively low probabilities then determines the system probability.

While difficult to determine, the modes of the geobag wall seem to lean more towards a dependent relationship, since all modes rely for a large part on the same parameter set. While this also applies to the interfaces, failure could occur simultaneously along multiple interfaces, where each interface has its own version of the parameter set, based on the wall

height. The interfaces therefore seem to lean more towards an independent relationship. Note that a perfect dependency or independency is unrealistic, meaning that the true system reliability is a combination of relationships.

The reliability of the geobag wall system directly answers the main research question, which seeks the answer of the reliability of the Koningsgracht method. As is discussed in the scope of this thesis, the reliability of Koningsgracht is considered to be equal to the reliability of the most sensitive phase, i.e. the geobag wall system. Hence, considering dependent modes and independent interfaces, the probability of failure of Koningsgracht is considered to be $1.625 \cdot 10^{-4}$ or 0.01625%.

9.6 Additional discussion of parameter effects

9.6.1 Cohesion and friction angle

From the sensitivity analysis, it can be seen that for higher levels of cohesion, higher FOS values are obtained for the failure modes. This implies that the cohesion, a soil parameter, decreases the backfill pressure for higher values. In the paper of Cho et al. (2015) [14] it is also concluded that cohesion reduces the lateral earth pressure and that it reduces the displacement of soil. Similar to the cohesion, when the friction angle is increased there is increase of the FOS values visible for all modes, indicating that the lateral earth pressure decreases. This can be explained by the fact that soil grains tend to interlock faster for higher friction angles, decreasing the mobilization of the soil, and with that its lateral pressure. [14]

Because the contribution of the friction angle is very large for the modes horizontal sliding and overturning, with a contribution of 64% and 72% respectively, it is of high importance to minimize its value uncertainty when making the geobag wall design. This could be done by performing an accurate on-site soil investigation of the backfill.

9.6.2 Friction angle wall-backfill

While performing the sensitivity analysis, it became apparent that the wall-backfill friction angle δ had a negligible influence on the FOS calculation. This was due to having an insignificant influence on the calculation of the active earth pressure coefficient, and therefore on the earth pressure itself. According to a study of Hu et al. (2017) [23], the friction angle of the wall-soil interface should be considered to have an influence on the effect of soil friction angle ϕ , rather than on the active earth pressure itself. In the paper, a curve was presented showing the relationship of the wall-soil friction angle δ , and the effect that the friction angle ϕ has on the active earth pressure K_a , shown in figure 9.6 below. [23]

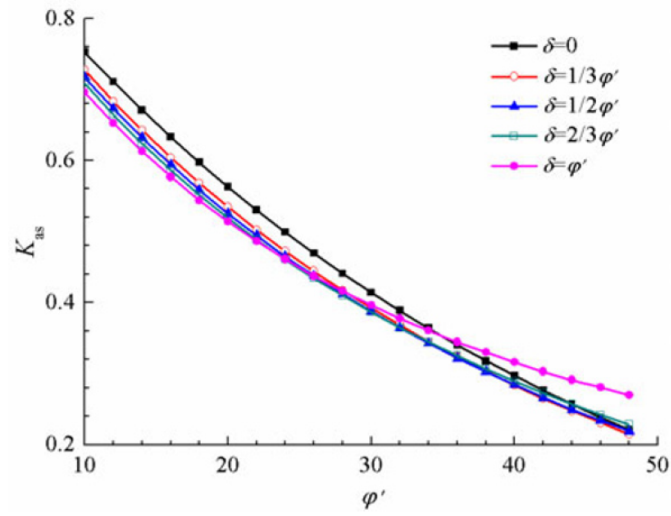


Figure 9.6: The effect of friction angle ϕ on the active earth pressure K_a for different values of wall-backfill friction angle δ . [23]

In the figure, the effect that different values of ϕ have on the value for K_a for a friction-less wall is shown by the black line for $\delta = 0$. When δ becomes a third, half or two thirds the value of ϕ , a small effect becomes apparent on the effect that ϕ has on K_a . Note that the effect of δ is almost negligible for $\delta = \phi$. The largest influence that δ can have is at $\phi = 45^\circ$ and $\delta = \phi$, although this is still only a 16% change compared to the $\delta = 0$ scenario. [23]

10 Conclusion

How do the support reactions change during Koningsgracht, and how is equilibrium maintained?

In evaluating the reliability of the Koningsgracht renewal method, a critical consideration is identifying the most sensitive phase during the renewal process. This phase was determined through a preliminary assessment of support reactions across various significant work phases.

In this assessment, no significant changes in support reactions were obtained, and therefore no direct signs of instabilities were observed during the Koningsgracht method. A change of loads, such as excavations, inserting the trench box or constructing the new concrete flooring, did not result into instabilities, especially when one would consider a stiff quay foundation. Equilibrium is mainly maintained by the vertical and horizontal support reactions of the wooden piles, flooring and the masonry wall. The support of the old quay wall is transferred to the inserted trench box, which on its turn transfers the support to the geobag wall.

What is the most sensitive phase in the Koningsgracht method?

Among the components of Koningsgracht, such as the historic construction, the new casings and piles, and the trench box, it is the geobag wall that emerges as the most sensitive due to its unique construction using jute bags. The relative rarity of geobag walls in engineering contexts underscores the importance of conducting a comprehensive stability assessment. This rarity stems from their distinctive use of jute bags, a material that, while environmentally friendly, introduces a degree of sensitivity to specific failure modes. Geobags, commonly used for coastal protection and soil reinforcement, are less frequently employed in tall retaining walls, making their stability assessment even more critical.

How to assess the Koningsgracht stability?

To assess the geobag wall's stability, various failure mechanisms and limit states were identified, including horizontal sliding, overturning, and rupture of the geobag textile. Uncertainty in geological and structural parameters necessitated the use of probability distributions to describe these parameters. Monte Carlo simulations and the First-Order-Second-Moment (FOSM) method, employed with the Probabilistic Toolkit of Deltares, enabled the analysis of these uncertainties.

To address spatial variability in geological parameters and to limit this variability with space, correlations were introduced. A consistent correlation was applied for structural parameters, considering that elements of the same material typically share similar parameter values.

What are the most sensitive variables in the most sensitive phase?

From the sensitivity analysis of the limit state variables, the limit state of $FOS = 2$ is used. The friction angle showed a large influence on both horizontal sliding and overturning, with a contribution of respectively 64% and 72%. For textile rupture, the tensile strength of jute is the most dominant parameter, with a 62% contribution on that failure mode. Additionally, the unit weight of the wall, with a 29% contribution, has a large effect on the FOS calculation of textile rupture. The large contribution of the friction angle asks for proper on-site soil investigations of the backfill that should be incorporated in the design. Information about the tensile strength of the jute geobags could be retrieved from the material supplier, or from strength experiments.

What is the reliability of the most sensitive phase of Koningsgracht?

After conducting Monte Carlo simulations and considering the limit state at $FOS = 1$, it was found that the global failure probabilities for horizontal sliding, overturning, and rupture are very small, represented by values to the power -5, -6 and -14 respectively. Locally, the probability of occurrence of the modes was again assessed along all interfaces, all similarly resulting in very small probabilities with large safety margins. This margin is lowest at the second interface from the bottom, followed by the bottom interface. The reason that the safety margin is lowest at the second interface is due to the smaller friction coefficient it has from its jute-jute contact plane, compared to the jute-concrete interface at the bottom. The uncertainty of the interface reliability increases with height of the wall. This is due to the deterministic values decreasing, increasing the contribution of uncertain variables.

The analyses highlighted the critical influence of the friction angle on horizontal sliding and overturning, while textile rupture depends heavily on the tensile strength of the jute. Wall tilt and additional surcharges significantly increased the probability of failure for all three modes. Furthermore, taller walls were found to drive overturning failure, while wider dimensions prevented overturning, but increased the risk of textile rupture.

A change of dependency between the modes or between the interfaces show a large impact on the system's reliability, where systems with solely dependent aspects have a higher reliability than systems with solely independent aspects. Full dependency or independency is unrealistic, meaning that the true relationships of the geobag wall is probably a combination. The geobag wall is considered to be most similar to a system with dependent modes and independent interfaces. This results into a geobag wall system probability of failure of $1.625 \cdot 10^{-4}$.

What is the reliability of Koningsgracht?

In the context of this thesis, it has been established that the reliability of Koningsgracht is equals to the reliability of its most vulnerable phase, namely the geobag wall system. Therefore, the likelihood of Koningsgracht experiencing failure is estimated to be $1.625 \cdot 10^{-4}$ or 0.01625%.

11 Recommendations

Since not all structural and geological mechanisms could be included in this thesis, a few recommendations are made for future work.

First of all, the stiffness of the geobags is a parameter that is not considered in the stability analysis of this thesis. The stiffness of geobags directly impacts their structural integrity. Geobags need to maintain their shape and stability over time to ensure the overall stability of the wall. The external factors that could lead to deformations include soil pressures, surcharges, and dynamic loads such as traffic vibrations. If the geobags are too flexible, they may deform or settle unevenly, potentially leading to structural failure. Furthermore, stiffness determines the distribution of loads and stresses across the wall interfaces. Stiffer geobags are more able to evenly distribute these loads, helping to prevent localized stress concentrations that could lead to failure. Finally, The stiffness of geobags can influence their interaction with the surrounding soil or with the concrete floor. Stiffer geobags may provide better soil confinement and frictional resistance, which can enhance the overall stability of the wall.

Secondly, a different approach to assessing the stability of the geobag wall is by using Finite Element Modelling software, such as PLAXIS. It allows for a highly accurate representation of complex geotechnical systems, such as the geobag wall, and for variations in stiffness, load distribution, and deformation across the entire wall. It can make complex geometries, and include interfaces where these are desired. Being able to choose from a variety of soil models, it could model the soil deformations and pressures that the soil exerts on the geobag wall more accurately. PLAXIS could therefore make an accurate estimation of the stability of the geobag wall. It might be possible to combine a PLAXIS analysis with a probabilistic analysis as is performed in this thesis, in order to get a more complete assessment of the geobag stability.

Thirdly, the effect of the casings that were situated through the geobag wall were neglected in this thesis. However, it might have been possible that the casings stabilize the geobag wall, since extra friction is added. It could also be possible that the casings disturb the geobag wall geometry in such a way that it loses integrity or stability. It is recommended to model the casings in FEM software, since complex casing-geobag interfaces are present.

Lastly, real sized experiments with geobag walls are recommended. When the pressures and deformations are monitored accurately, and when material properties are known, it could give insights in the behavior of the geobag wall under a variety of pressures, in a variety of wall dimensions. It could then be assessed under what conditions the wall tends to fail locally, and if deformation behavior as bulging or tilting occurs. Using real sized experiments could also be a manner to validate the probabilistic model that is constructed.

References

- [1] Innovatiepartnerschap Kademuren (IPK) - Ingenieursbureau Amsterdam.
- [2] NEN 9997-1:2016/C2:2017 nl.
- [3] Probabilistic Toolkit (PTK) - Deltares.
- [4] Renovatie kademuren Amsterdam — Royal HaskoningDHV.
- [5] Standard Deviation Graph - Deviation Calculator.
- [6] M. Alam, O. Chaallal, and B. Galy. Soil-Structure Interaction of Flexible Temporary Trench Box: Parametric Studies Using 3D FE Modelling. *Modelling and Simulation in Engineering*, 2021, 2021.
- [7] S. Banne, S. Pathak, and A. Dhawale. Influence of Wall Friction and Surcharge on Active Earth Pressure in Model Test. 8 2021.
- [8] E. Bastidas-Arteaga and A.-H. Soubra. Reliability Analysis Methods. 10 2014.
- [9] A. Bensoussan. Reliability Index. In R. F. Deissenberg Christophe }and Hartl, editor, *Optimal Control and Dynamic Games: Applications in Finance, Management Science and Economics*, pages 311–317. Springer US, Boston, MA, 2005.
- [10] P. J. Blau. The significance and use of the friction coefficient. *Tribology International*, 34:585–591, 2001.
- [11] A. Bouazza and S. Djafer-Khodja. Friction Characteristics of a Nonwoven Geotextile and Peat. 1994.
- [12] H. Brooks and J. Nielsen. *Basics of Retaining Wall Design*. HBAPublications, Newport Beach, 10 edition, 2013.
- [13] X. Cai, S. Zhang, S. Li, H. Xu, X. Huang, and C. Zhu. A Review of the Methods Calculating the Horizontal Displacement for Modular Reinforced Soil Retaining Walls. *Applied Sciences*, 11(8681):8681, 9 2021.
- [14] J. Cho, H. Lim, S. Jeong, and K. Kim. Analysis of lateral earth pressure on a vertical circular shaft considering the 3D arching effect. *Tunnelling and Underground Space Technology*, 48:11–19, 4 2015.
- [15] A.-S. Colas, J.-C. Morel, and D. Garnier. Full-scale field trials to assess dry-stone retaining wall stability. *Engineering Structures*, 32:1215–1222, 2010.
- [16] S. Frankenmolen. *Analyse Noord/Zuidlijn monitoringsdata: Effecten van de beïnvloeding van de Holocene Laag op het zettingsgedrag van vooroorlogse panden*. PhD thesis, 2006.

- [17] A. Gaur and A. Sahay. Comparison of Different Soil Models for Excavation using Retaining Walls. *SSRG International Journal of Civil Engineering (SSRG-IJCE)*, 4, 2017.
- [18] Gemeente Amsterdam. Notulen review op normen en uitgangspunten bij beoordelen en ontwerpen kademuren gemeente Amsterdam. Technical report, 2022.
- [19] S. Ghosh, R. Bhattacharyya, and M. Mondal. A review on jute geotextile - part 1. *IJRET: International Journal of Research in Engineering and Technology*, 3(2), 2014.
- [20] A. Haddad, D. Rezazadeh Eidgahee, and H. Naderpour. A probabilistic study on the geometrical design of gravity retaining walls. *World Journal of Engineering*, 14(5):414–422, 1 2017.
- [21] N. Hataf and M. Sayadi. Experimental and numerical study on the bearing capacity of soils reinforced using geobags. *Journal of Building Engineering*, 15:290–297, 1 2018.
- [22] M. J. Hemel, M. Korff, and D. J. Peters. Analytical model for laterally loaded pile groups in layered sloping soil. *Marine Structures*, 84:103229, 7 2022.
- [23] Z. Hu, Z. X. Yang, and S. P. Wilkinson. Active earth pressure acting on retaining wall considering anisotropic seepage effect. *Journal of Mountain Science*, 14(6):1202–1211, 2017.
- [24] S. Jonkman, R. Steenbergen, O. Morales-Nápoles, A. Vrouwenvelder, and J. Vrijling. Probabilistic Design: Risk and Reliability Analysis in Civil Engineering Lecture notes CIE4130, 2016.
- [25] Korff, Hemel, and Peters. Collapse of the Grimburgwal, a historic quay in Amsterdam, the Netherlands. *Proceedings of the Institution of Civil Engineers: Forensic Engineering*, 175(4):96–105, 4 2022.
- [26] T. Krahn, J. Blatz, M. Alfaro, and R. Bathurst. Large-scale interface shear testing of sandbag dyke materials. *Geosynthetics International - GEOSYNTH INT*, 14:119–126, 10 2007.
- [27] C. Lee. *Math in Society: Mathematics for liberal arts majors*. Portland Community College Math Department, 8 2020.
- [28] J. Lieftinck. *Inclination Behaviour of Historic Quay Walls*. PhD thesis, Delft University of Technology, Delft, 1 2022.
- [29] A. Mahmood and N. Zakaria. A study on the coefficient of friction of soil/geotextile interfaces. *Electronic Journal of Geotechnical Engineering*, 5, 6 2000.
- [30] H. Matsuoka and S. Liu. New Earth Reinforcement Method by Soilbags (“Donow”). *Soils and Foundations*, 43(6):173–188, 2003.

- [31] P. F. McCombie, C. Mundell, A. Heath, and P. Walker. Drystone retaining walls: Ductile engineering structures with tensile strength. *Engineering Structures*, 45:238–243, 12 2012.
- [32] R. Mustafa, P. Samui, and S. Kumari. Probabilistic analysis of gravity retaining wall using ANFIS-based optimization techniques. *Innovative Infrastructure Solutions*, 7(6):1–16, 12 2022.
- [33] Nederlandse Geotextielorganisatie and Rijkswaterstaat. CUR 174: Geokunststoffen in de waterbouw. Technical report, Gouda, 2009.
- [34] Royal HaskoningDHV. Aanzicht kade. Technical report.
- [35] Royal HaskoningDHV. Bepaling wrijvingscoëfficiënt Enkadrain CK20 - internal document - RHDHV. Technical report.
- [36] Royal HaskoningDHV. Fasering Koningsgracht stappenplan.
- [37] Royal HaskoningDHV. Quay wall pile dimensions and groups.
- [38] J. Ruigrok. Laterally Loaded Piles. Technical report, TU Delft - Faculty of Civil Engineering and Geosciences - Section of Geo-engineering, Delft, 2010.
- [39] Samenwerkingsverband Koningsgracht. IPK Ontwerpnota NOK Pilotproject Brouwersgracht. Technical report, 2022.
- [40] T. Sanyal. Developments in Geotechnical Engineering Jute Geotextiles and their Applications in Civil Engineering. 2017.
- [41] SBRCURnet. CUR 198 - Ontwerprichtlijn Kerende constructies van gewapende grond. Technical report, SBRCURnet, Delft, 2017.
- [42] A. P. Singh and K. Chatterjee. Effect of Soil–Wall Friction Angle on Behaviour of Sheet Pile Wall Under Surcharge Loading. *Proceedings of the National Academy of Sciences India Section A - Physical Sciences*, 91(1):169–179, 3 2021.
- [43] S. Van Baars and H. Kuijper. *CT3330 Handboek Constructieve Waterbouw*. 2002.
- [44] J. Van Dalen. Slides - Introduction to Structural Mechanics - CIE4370-19, 2019.
- [45] J.-W. van de Kuilen, O. Beketova-Hummel, G. Pagella, G. Ravenshorst, and W. Gard. An integral approach for the assessment of timber pile foundations. 5 2021.
- [46] R. Van der Eijk. *Alternatieven voor de zandzak als tijdelijke waterkering*. PhD thesis, Technische Universiteit Delft, Krimpen aan den IJssel, 2002.

12 Appendix A - NEN 9997 - Table 2b

Tabel 2.b — Karakteristieke waarden van grondeigenschappen

Grondsoort			Karakteristieke waarde ^a van grondeigenschap												
Hoofd-naam	Bijmengsel	Consistentie ^b	γ^c	γ_{sat}	$q_c^{d,g}$	C'_p^g	C'_s	$C_c/(1+e_0)^g$	C_σ^f	$C_{sw}/(1+e_0)^g$	$E_{100}^{g,h}$	ϕ'^g	c'	c_u	
			kN/m ³	kN/m ³	MPa			[-]	[-]	[-]	MPa	Graden	kPa	kPa	
Grind	Zwak siltig	Los	17	19	15	500	∞	0,004 6	0	0,001 5	45	32,5	0	N.v.t.	
		Matig	18	20	25	1 000	∞	0,002 3	0	0,000 8	75	35,0	0		
		Vast	19 20	21 22	30	1 200 1 400	∞	0,001 9 0,001 6	0	0,000 6 0,000 5	90 105	37,5 40,0	0		
	Sterk siltig	Los	18	20	10	400	∞	0,005 8	0	0,001 9	30	30,0	0	N.v.t.	
		Matig	19	21	15	600	∞	0,003 8	0	0,001 3	45	32,5	0		
		Vast	20 21	22 22,5	25	1 000 1 500	∞	0,002 3 0,001 5	0	0,000 8 0,000 5	75 110	35,0 40,0	0		
Zand	Schoon	Los	17	19	5	200	∞	0,011 5	0	0,003 8	15	30,0	0	N.v.t.	
		Matig	18	20	15	600	∞	0,003 8	0	0,001 3	45	32,5	0		
		Vast	19 20	21 22	25	1 000 1 500	∞	0,002 3 0,001 5	0	0,000 8 0,000 5	75 110	35,0 40,0	0		
	Zwak siltig, kleiig	18 19	20 21	12	450 650	∞	0,005 1 0,003 5	0	0,001 7 0,001 2	35 50	27,0 32,5	0	N.v.t.		
	Sterk siltig, kleiig	18 19	20 21	8	200 400	∞	0,011 5 0,005 8	0	0,003 8 0,001 9	15 30	25,0 30,0	0	N.v.t.		
	Leem ^e	Zwak zandig	Slap	19	19	1	25	650	0,092 0	0,003 7	0,030 7	2	27,5 30,0	0	50
Matig			20	20	2	45	1 300	0,051 1	0,002 0	0,017 0	3	27,5 32,5	1	100	
Vast			21 22	21 22	3	70 100	1 900 2 500	0,032 9 0,023 0	0,001 3 0,000 9	0,011 0 0,007 7	5 7	27,5 35,0	2,5 3,8	200 300	
Sterk zandig		19 20	19 20	2	45 70	1 300 2 000	0,051 1 0,032 9	0,002 0 0,001 3	0,017 0 0,011 0	3 5	27,5 35,0	0 1	50 100		
Klei	Schoon	Slap	14	14	0,5	7	80	0,328 6	0,013 1	0,109 5	1	17,5	0	25	
		Matig	17	17	1,0	15	160	0,153 3	0,006 1	0,051 1	2	17,5	5	50	
		Vast	19 20	19 20	2,0	25 30	320 500	0,092 0 0,076 7	0,003 7 0,003 1	0,030 7 0,025 6	4 10	17,5 25,0	13 15	100 200	
	Zwak zandig	Slap	15	15	0,7	10	110	0,230 0	0,009 2	0,076 7	1,5	22,5	0	40	
		Matig	18	18	1,5	20	240	0,115 0	0,004 6	0,038 3	3	22,5	5	80	
		Vast	20 21	20 21	2,5	30 50	400 600	0,076 7 0,046 0	0,003 1 0,001 8	0,025 6 0,015 3	5 10	22,5 27,5	13 15	120 170	
	Sterk zandig	-	18 20	18 20	1,0	25 140	320 1 680	0,092 0 0,016 4	0,003 7 0,000 7	0,030 7 0,005 5	2 5	27,5 32,5	0 1	0 10	
		Organisch	Slap	13	13	0,2	7,5	30	0,306 7	0,015 3	0,102 2	0,5	15,0	0 1	10
Veen	Niet voorbelast	Matig	15 16	15 16	0,5	10 15	40 60	0,230 0 0,153 3	0,011 5 0,007 7	0,076 7 0,051 1	1,0 2,0	15,0	0 1	25 30	
		Matig voorbelast	10 12	10 12	0,1	5 7,5	20 30	0,460 0 0,306 7	0,023 0 0,015 3	0,153 3 0,102 2	0,2 0,5	15,0	1 2,5	10 20	
Variatiecoëfficiënt v			0,05		-	7,5 10		30 40	0,306 7 0,230 0	0,015 3 0,011 5	0,102 2 0,076 7	0,5 1,0	15,0	2,5 5	20 30
									0,25			0,10		0,20	

^a De tabel geeft van de desbetreffende grondsoort de lage, respectievelijk de hoge karakteristieke waarde van gemiddelden. Binnen een gebied, vastgesteld door de rij van het bijmengsel en de kolom van de parameter (een cel), geldt:

- als een verhoging van de waarde van een van de grondeigenschappen tot een ongunstiger situatie leidt dan de toepassing van de in de tabel gepresenteerde lagere karakteristieke waarde, moet de rechterwaarde op dezelfde regel zijn gebruikt. Is er rechts geen waarde vermeld, dan moet de waarde er recht onder zijn toegepast;
- OPMERKING Dit is bijvoorbeeld het geval bij negatieve kleef op een paal waar een hogere waarde van ϕ' , c' en c_u ook een hogere waarde van de negatieve kleef oplevert.
- voor $C_c/(1+e_0)$, C_σ en $C_{sw}/(1+e_0)$ zijn in de tabel de hoge karakteristieke gemiddelde waarden vermeld.